Heterogeneous Reactions of Micro and Nano Aluminum Particles with Various Oxidizers

by

Florin Saceleanu

A thesis

presented to the University of Waterloo

in fulfilment of the

thesis requirement for the degree of

Doctor of Philosophy

in

Mechanical and Mechatronics Engineering

Waterloo, Ontario, Canada, 2019

Examining Committee Membership

The following served on the Examining Committee for this thesis. The decision of the Examining Committee is by majority vote.

External Examiner	CHARLES DUBOIS Professor
Supervisor(s)	JOHN Z. WEN Associate professor
Internal Member	MUSTAFA YAVUZ Professor
Internal Member	DONGQING LI Professor
Internal-external Member	ERIC CROISET Professor

Author's Declaration

I hereby declare that I am the sole author of this thesis. This is a true copy of the thesis, including any required final revisions, as accepted by my examiners.

I understand that my thesis may be made electronically available to the public.

Abstract

Micro and nano aluminum (Al) particles have drawn much attention for properties as metal fuels in energetic materials. Aluminum is the preferred metal due to its thermodynamic stability after long term storage, abundance on Earth and relatively high reactivity with various oxidizers such as oxygen gas, metal oxides and liquid water. This thesis investigates the kinetics of heterogeneous reactions of micro and nano aluminum particles via controlled oxidation and combustion experiments. The main objectives of this research are to incorporate fundamental theories in solid state kinetics with the experimental data/observations, and obtain a deeper understanding of the kinetic mechanisms that control these heterogeneous reactions. Proper experimental setups and procedures are an essential part of this research due to the currently limited theoretical knowledge in this field.

Studies have shown that mass diffusion and phase transformations processes are elementary for reactions of Al in air or oxygen. However, the physical processes regarding simultaneous oxidation and phase transformation were unclear. Thermogravimetric and differential scanning calorimetry experiments and the core-shell model of oxidation were combined, and it was found that this model is only applicable when the shell does not undergo phase transformations. On the other hand, the simultaneous oxidation and phase transformation were explained by the nucleation and growth model with a parameter that defines the rate controlling processes. Diffusional processes were rate determining steps in the oxidation of micro and nano Al powders while the kinetics of the chemical reactions were very fast. Similarly, high speed imaging of the combustion of consolidated Al particles via laser ignition in a closed chamber at various partial pressures of oxygen indicated that oxygen diffusion is the rate controlling mechanism of flame

propagation. However, some experimental observations diverge from the theoretical predictions due to the particle agglomeration and inhomogeneous pore structure.

Aluminum based thermites are a class of highly energetic materials composed of solid state Al and metal oxidizer with tunable combustion properties. The ignition and combustion mechanisms of consolidated aluminum/copper oxide (CuO) nanothermite pellets were investigated via laser ignition coupled with high speed imaging. It was found that the fast heating created significant material ablation followed by heat transfer along the heated surface. The bulk ignition occurred near the edges prior to the self-sustained combustion. The high porosity Al/CuO pellets ignited significantly faster and the burning speed was orders of magnitude higher compared to the low porosity pellets. The results indicated that the reaction mechanism changed from mass convection to heat conduction with increasing the bulk density. Scanning electron microscopy images of pre and post-combustion illustrated that homogeneity of the mixture is a critical parameter for optimizing the performance. On the other hand, the type of nanothermite structures is a critical parameter for the tenability of these reactions. It was found that the ignition mechanisms of the consolidated Al/CuO nanoparticles and sputtered Al/Cu_2O nanolaminates are fundamentally different. The net energy balance on the laser heated surface controlled the ignition delay in the pellets, and this was dominated by the net thermal conductivity of the porous structure. A semi-empirical laser ignition model of the pellets was proposed. On the other hand, significant laser energy absorption was mandatory for the ignition of nanolaminates. The ignition delay was optimized by finding the optimum Cu_2O layer thickness that maximized both the absorption coefficient of laser radiation and the mass diffusion rates of oxygen.

The reactions between aluminum and liquid water are attractive to generated hydrogen gas on-demand. Controlled oxidation experiments were performed using isothermal calorimetry and self-sustained combustion experiments were performed using a high pressure batch reactor. . It was found that the nucleation and growth of the aluminum hydroxides byproducts control the kinetics of these reactions and thus the kinetics of hydrogen release. Model and model-free methods were implemented to describe the reaction sequence. It was found that this mechanism exhibits two distinct and sequential stages: a kinetically controlled stage where nucleation and growth is limited by the chemical reactions on the surface of aluminum, and a diffusion controlled stage where the growth is limited by the mass diffusion through the aluminum hydroxide by-products. The separation of these stages is not obvious under non-isothermal conditions due to the overlap of the stages, and the one with a lower E_a dominates. The kinetics of the reactions was significantly increased under high temperature and pressure, which prevented the boiling of water. The Al-hydroxide byproducts and NaOH solutions were found to have catalytic properties on the Al/water reactions by lowering the apparent activation energy. A semi-empirical batch reactor model was proposed to study the complexity of these heterogeneous reactions.

Acknowledgements

I would like to thank my supervisor, Dr. John Wen, for giving me the opportunity, guidance and financial support to complete this thesis. He taught me to approach complicated physics from the first principles and simplify the problem. Also, I would like to thank the committee members for their comments and suggestions to improve this thesis. I would like to acknowledge my colleagues Dr. Munur Herdem, Dr. Hongtao Sui, Ms. Yiqi Zhang, Mr. Alex Baranovsky, Mr. Joseph Mark Epps, Ms. Boyu Li and Ms. Lauren LeSergent, for all the research related discussions. Last but not least, I am very thankful to my girlfriend and family for the years of encouragement and support whenever necessary.

Table of Contents

List of Figures

List of Tables

1. Introduction

Energetic materials at the micro and nano scale have gained significant interest for potential use in propellants, explosives, heat generators and pyrotechnics, since the chemical energy is released as heat. In monomolecular energetic materials, the fuel and oxidizer are within one molecule. Despite the high energy release rate due to kinetically controlled reactions of the monomolecular materials, they are chemically unstable and the packing density is limited [1]. On the other hand, composite materials are heterogeneous mixtures of the fuel and oxidizer. The energy release rates are usually controlled by mass diffusion; hence the mixture quality is very important to enhance the reactivity. Metal fuels are attractive due to the higher enthalpy of combustion in oxygen than the monomolecular energetics as shown in Figure 1.1. From the metals shown, beryllium, Be, and lithium, Li, are extremely toxic, and boron, B, has high ignition temperatures and reduced energy release rates due to the protective boron oxide layer [1]. Aluminum, Al, on the other hand, is abundant on Earth, safe to use, and chemically stable due to protective alumina layer. There has been significant research on aluminum (Al) particles in the past two decades due to their high reactivity with oxidizers in gaseous, liquid and solid state. It is a promising metallic fuel given its high energy density relative to other metals, thermodynamic stability after long term storage, and scalability from the nano/micro to the macro scale in the experiments.

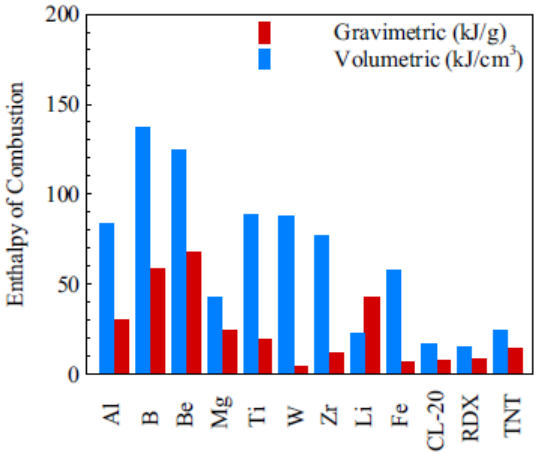

Figure 1.1: Enthalpy of combustion of various metals and monomolecular energetics [1]

1.1. Aluminum as a metal fuel

Aluminum oxidizes according to the following chemical reaction

$$2Al_{(s)} + 3/2O_{2(g)} \rightarrow Al_2O_{3(l-g)} \qquad \text{(R1.1)}$$

The enthalpy of this reaction is approximately 31 kJ/g Al if the Al reactants and Al_2O_3 products are on the bulk scale (i.e. size independent) [2]. The adiabatic flame temperature is limited to the vaporization-dissociation temperature of the metal oxide. This is because the heat available from the oxidation reaction is not enough to raise the condensed state of the oxide to its boiling temperature [3]. In reaction R1.1, the adiabatic flame temperature is around 4000 K, which is significantly above 2791 K required to boil aluminum. Hence, according to Glassman criterion of metal combustion, aluminum burns in vapor phase [3]. This mechanism of combustion is applicable to large particle sizes (micron and above), but fails to explain the combustion of nano sized Al particles.

Figure 1.2: Core-shell aluminum particle

Aluminum is covered by a native alumina shell that protects the active core as shown in Figure 1.2. This Al_2O_3 shell play an important role on the ignition and combustion characteristics of Al since it is a diffusion barrier for the reaction. The effects of size become important when the particle dimension reaches the nano scale. The thermo-physical, kinetic and mechanical properties of nano powders are significantly different than those of the bulk material due to the enhanced surface energy. There are several advantages of Al nanoparticles as discussed in references [4] and [5]: a) decreased diffusion distances between the Al and the oxidizer, which decrease the reaction time; b) increase specific surface area and high percentage of surface atoms relative to bulk atoms, which enhance reactivity; c) lower ignition temperatures

and activation energies due to the enhanced surface energy; d) more uniform mixing between the Al particles and metal oxidizers, which enhance the reaction rates. However, the main drawback of Al nanoparticles is that the active content is reduced significantly since the alumina mass is large relative to the particle mass [6] as shown in Figure 1.3. Also, the combustion of Al nanoparticles is highly sensitivity the surrounding conditions. Particles below 50 nm are considered pyrophoric [7], and care should be taken when mixing and handing these powders. Despite the size reduction, it has been shown that Al nano powders maintained their high reactivity despite 10 to 27 years of storage in nitrogen or argon [8].

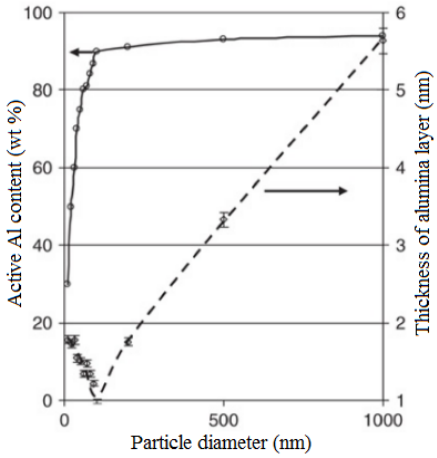

Figure 1.3: Size dependent active content of Al particles [6]

1.2. The Al based thermite reaction

A thermite reaction is a chemical reaction where a reactive metal (e.g. Al) reacts with a metal oxide (e.g. copper oxide, CuO). Thermites are highly exothermic reactions with potential applications in welding, joining, propulsion, igniters. The global Al-CuO reaction is shown in reaction R1.2 below

$$2Al_{(s)} + 3CuO_{(s)} \rightarrow Al_2O_{3(l)} + 3Cu_{(l-g)} \qquad \text{(R1.2)}$$

The enthalpy of this reaction is about 4075 kJ/kg, and the adiabatic flame temperature is 2843 K [9]. Common thermite reactions along with their heat of reaction, adiabatic flame temperature and amount of gas generated are listed Table 1.1. The amount of gas generation and heat release have a direct effect on the potential application; for instance, Al-CuO can be used for propulsion

due to its high gas generation, whereas Al-Fe_2O_3 can be used for welding due to its large heat release with small amount of gas generation.

Table 1.1: Theoretical energy release, adiabatic flame temperature, and gas generation of common thermites [9]

Reactants	Products	Heat of reaction (J/g)	Adiabatic flame temperature (K)	Gas generation (g/g reactant)
$2Al_{(s)} + 3CuO_{(s)}$	$Al_2O_{3(l)} + 3Cu_{(l-g)}$	4075	2843	0.3431
$2Al_{(s)} + Fe_2O_{3(s)}$	$Al_2O_{3(l)} + 2Fe_{(l-g)}$	3955	3135	0.0784
$2Al_{(s)} + 3NiO_{(s)}$	$Al_2O_{3(l)} + 3Ni_{(l-g)}$	3440	3187	0.0063
$2Al_{(s)} + MoO_{3(s)}$	$Al_2O_{3(l-g)} + Mo_{(l)}$	4703	3253	0.2473
$2Al_{(s)} + WO_{3(s)}$	$Al_2O_{3(l-g)} + W_{(l)}$	2914	3253	0.1463

Thermites have higher reaction rates compared to the combustion of Al in atmospheric air due to the higher concentration of oxidizer around the Al particle, and smaller diffusion distances between Al and oxidizer. The fast oxidation of aluminum in a thermite reaction can occur in two modes: 1) condensed phase, where the oxygen and aluminum ions are transported across the Al/metal oxidizer interface [10], and 2) gas phase, where the metal oxidizer first dissociates and creates a dense oxygen atmosphere around the Al particle [11]. Once the thermite is ignited, the combustion flame self-propagates via mass and heat transfer processes such as heat conduction and mass convection.

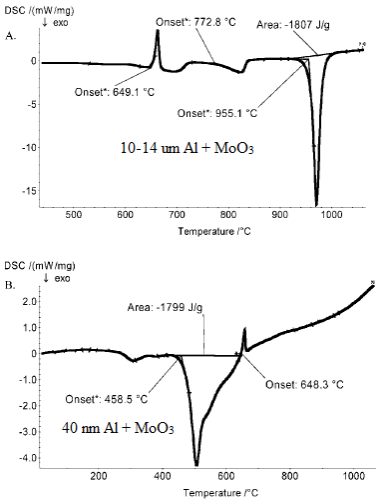

Figure 1.4: Heat release of micro and nano Al/MoO3 thermites [13]

Nanothermites have significantly higher reaction rates and lower ignition temperatures compared to the thermites counterparts. The higher specific surface area improves the homogeneity of the mixture, thus enhancing the reaction rates. Furthermore, nano scale metal oxidizers decompose at lower temperatures since the particle heating timescale and diffusion length scales for oxygen release are reduced [12]. Figure 1.4 shows the heat

release of Al/MoO_3 nanothermites and micro thermites [13]. It can be seen that the nanothermite ignites before the melting temperature of aluminum, whereas the micro thermite requires molten aluminum to ignite and sustain the combustion.

1.3.The aluminum-water reaction

The reaction between aluminum and water, H_2O, has gained significant interest in the past decade as a feasible method for clean propulsion and power generation [14]. This reaction produces hydrogen, which may become an important source for environmentally friendly energy. The cogeneration of hydrogen and electricity from Al/water reactions has been proposed in reference [15]. The reaction between Al and H_2O is slow at low temperatures due to the alumina passivation layer illustrated in Figure 1.2. Water must hydrate this alumina layer in order to break the Al-O bonds. The Al/H_2O reactions are highly exothermic and produce aluminum hydroxides by-products as shown in the reactions R3, R4 and R5 [16].

$$Al_{(s)} + 3H_2O_{(l)} \rightarrow Al(OH)_{3\,(s)} + 3/2H_{2\,(g)} \quad \text{(R1.3)}$$

$$Al_{(s)} + 2H_2O_{(l)} \rightarrow AlOOH_{(s)} + 3/2H_{2\,(g)} \quad \text{(R1.4)}$$

$$Al_{(s)} + 3/2H_2O_{(l)} \rightarrow 1/2Al_2O_{3\,(s)} + 3/2H_{2\,(g)} \quad \text{(R1.5)}$$

Reaction R1.3 forms bayerite, $Al(OH)_3$, and it is thermodynamically favourable between room temperature and 280 ˚C with a reaction enthalpy of 426.5 kJ/mol. Reaction R1.4 forms boehmite, AlOOH, and it is thermodynamically favourable between 280 and 480 ˚C with a reaction enthalpy of 414 kJ/mol. Reaction R1.5 forms alumina, Al_2O_3, and it is thermodynamically favourable above 480 ˚C with a reaction enthalpy of 402 kJ/mol [17]. Chemically, these are

redox reactions, where the anodic reaction oxidizes Al to Al^{3+} and the cathodic reaction reduces H_2O to $OH^- + H_2$.

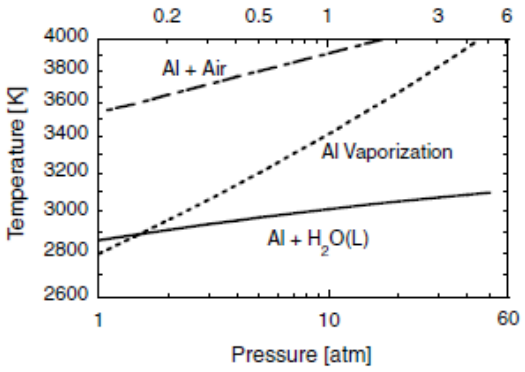

Figure 1.5: Adiabatic flame temperature of aluminum-air and aluminum-water [18]

The adiabatic flame temperature of the Al/water reaction is significantly lower than the adiabatic flame temperature of Al/air as shown in Figure 1.5 [18]. For pressure higher than atmospheric, the Al does not vaporize and the reactions occur as heterogeneous processes. Furthermore, water should be kept in liquid state during the reaction in order to maximize the contact surface between Al particles and H_2O molecules.

1.4.Motivation

Energetic materials based on aluminum micro and nano particles are promising for power generation, propulsion and hydrogen production. As explained above, this metallic fuel reacts in various oxidizing atmospheres such as air, water and metallic oxides. In Al based thermites, the heat release and gas generation should be tunable and optimized for power generation or propulsion, respectively. In Al/water reactions, the heterogeneous processes should be well understood since they play an important role on the kinetics of hydrogen production. There are key parameters that must be understood for the targeted application: the particle size and active content of Al and the metal oxidizer, the purity/partial pressure of the liquid/gaseous oxidizer, the synthesis/fabrication of these mixtures, and the heating rate for igniting the mixture. Furthermore, it is important to control the integrity of the reactive mixture, the rate of energy release and phases of the products for the particular application.

The reaction mechanisms of Al based energetic materials at the micro/nano scale are complex due to their heterogeneous nature, and lack of accurate thermo-physical and kinetic properties of nanoparticles [6]. The phase transformations and reaction kinetics of aluminum particles with gaseous oxidizers should be well understood since it is fundamental in Al based thermites. Generally, the core-shell model of oxidation is used to understand the reaction kinetics [19] [20], which ignore the effects of sintering and agglomeration. Thermodynamics of the detailed reaction steps are generally limited to the materials on the bulk scale assuming local thermodynamic equilibrium between the solid and gaseous phases [21]. On the other hand, the nucleation and growth of the by-products should be well understood since it is fundamental in Al/water reactions. Again, thermodynamic data is limited to the materials on the bulk scale, and the reaction kinetics assumes the core-shell model of aluminum [22] [23], despite the complex and irregular morphologies of the by-products [24]. Given the limited theoretical understanding of Al based energetic materials, it is important to design proper experiments with state of the art apparatus, to characterize the reactivity and reaction mechanisms of these mixtures.

1.5.Challenges and research gap

Fundamental understanding of the reaction kinetics between Al micro/nano particles and various oxidizers is an ongoing topic. The main reason is that the theoretical background is not well established due to the complex structure of the Al particles, lack of thermos-physical properties for reactants and products, unknown reaction mechanisms complicated by phase transformations, and the multi-physics nature of these heterogeneous reactions. Micro and nano Al particles generally have spherical morphology and are covered by a native alumina shell that prevents oxidation of the Al core as shown in Figure 2. The physicochemical processes that occur within

this shell and the thermodynamic stability at the aluminum/alumina interface have significant effects on the kinetics of reaction.

Thermodynamic and kinetic properties of Al based energetic materials are lacking due to the size effects complicated by agglomeration. As the particle size decreases to micro or nano scale, its specific surface area and surface energy increase. This specific surface energy changes the thermodynamic properties such as the enthalpy change of the reaction [25], specific heat capacity, thermal conductivity, and melting temperature [6], and kinetic properties such as the apparent activation energy [7]. There are theoretical equations that relate these thermodynamic properties to the size of a single particle. For example, the enthalpy of reaction can be related to the size dependent cohesive and lattice energies and the surface energy at the Al/Al_2O_3 interface; the melting temperature can be approximated by the Gibbs-Thompson equation for spherical particles; specific heat capacity and thermal conductivity can be related to the porosity and bulk density; and apparent activation energy can be reduced by the higher surface energy to volume ratio of nanoparticles. However, Al powders have a size distribution such that the particles at the tail of the distribution may react differently compared to the most probable particle sizes. The high surface energy forces the small sized particles (nanoparticles) to agglomerate in order to minimize this energy. The particle size distribution along with agglomeration makes it very challenging to model the physical processes within these reactions. The kinetics of reactions of solid particles is generally modelled using the temperature dependent Arrhenius equation with two parameters, the activation energy and the frequency factor. This kinetic model has a physical interpretation for elementary reactions. The activation energy is the energy barrier (units of kJ/mol) that must be overcome to initiate the reaction, and the frequency factor (units of Hz) is the collision rate with correct orientation that results in a chemical reaction. However, in the case

of heterogeneous reactions, where the elementary steps are unknown, there is not an exact interpretation of the reaction kinetics. There are mass and heat transfer processes such as diffusion, adsorption, nucleation, phase transformation, in addition to the chemical reaction, which complicate the global reaction mechanism. In this case, the Arrhenius equation may define the rate determining step, which can change with the progress of the reaction. The Arrhenius parameters have a similar interpretation as mentioned before, but activation energy is apparent for this rate determining step, and the frequency factor is dependent on the mixture morphology, external temperature and pressure.

The reaction mechanisms of Al based energetic materials are very complex due to the fast kinetics that occurs simultaneously with phase transformations and mass diffusion. The spherical core-shell model has been widely accepted in literature for Al particles that react in gaseous atmosphere. In this model, the Al core reacts with oxygen to form the Al_2O_3 shell, which grows with the progress of the reaction. The reaction front can be located at the Al/Al_2O_3 interface, inside the Al_2O_3 shell, or at the Al_2O_3/surroundings interface. This location and physical state of aluminum play a dominant role on the reaction mechanism. Experiment data shows that Al nanoparticles oxidize below their melting temperature, whereas Al micro particle oxidize after the melting temperature. Furthermore, Al_2O_3 can undergo several phase transformations from amorphous to crystalline states, which have a significant effect on the mass and heat diffusion processes [26]. A similar core-shell model has been accepted in literature for Al particles that react with water. In this case, water must first hydrate the alumina shell in order to reach the aluminum core. The reaction between Al and water produces hydrogen gas and Al-hydroxides with highly irregular morphologies [27]. Hence it is difficult to study the kinetics of such reactions due to the unknown/complex pathways. The physics are complicated further for

reactions between Al and solid oxidizers (i.e. thermites). It has been shown that such reactions initiate at the aluminum/metal oxidizer interface via a reactive sintering mechanism [28]. This suggests that mixture homogeneity plays a critical role on ignition. Furthermore, some metal oxidizers such as copper oxide, CuO, can release oxygen around the ignition temperature of the thermite. It has been shown that on a scale much larger than the particle size, the mass transport of this oxygen is a rate determining process [29]. The contribution of these competitive steps (i.e. the reactions at the metal/metal and metal/gas interfaces) on the overall reaction mechanism remains unclear.

Given the multi-physics nature of these heterogeneous reactions along with the lack of thermodynamic and kinetic data, complicated by agglomeration at the micro/nano scale, it is imperative that experiments are conducted upon which hypotheses can be made. The experimental apparatus should provide accurate measurements of the rates of energy release, phase changes, flame propagation, etc.

1.6.Objectives

The experimental apparatus is a fundamental part of studying the kinetics of reactions in solid state, such as Al powders mixed with various oxidizers. Repeatable and validated experimental data is necessary to form hypotheses on the reaction mechanisms, due to the complexity of these heterogeneous reactions and the size dependent thermodynamics/kinetics. The purpose of this thesis is to investigate the reaction kinetics for the following: a) Al nano and micro powders, oxidized and ignited in oxygen at different partial pressures; b) Al/CuO nano powder mixtures at various equivalence ratios, ignited in argon; and c) Al nano and micro powders oxidized and ignited in distilled water, with and without catalysts, at different equivalence ratios. The experimental apparatus used and the setups developed measure parameters such as the rate of

heat release, the flame propagation, and the rate of hydrogen produced, in order to monitor accurately the extent of the reaction. There are three main objectives of this research:

First of all, the reactive mixtures are prepared using simple and repeatable ultra-sonication methods. The as-received Al powders are sonicated in ethanol in order to reduce agglomeration. The as-received CuO powders are added to the sonicated Al solution and further sonicated to improve the homogeneity of the mixture. The ethanol is evaporated overnight in the fume hood and the mixture is further dried in the oven to remove adsorbed moisture. For the Al/water mixtures, the Al powders are sonicated in water for shorter durations to prevent initiation. The Al powders, Al/CuO mixtures and the corresponding reaction products are investigated under scanning electron microscopy and x-ray diffraction to determine their morphologies and chemical compositions.

Secondly, experimental methods are developed to quantify the reactivity of the Al-based mixtures under high heating rates, such as the ignition delay, flame propagation speed, burn duration, heat release, pressurization rates. Micro calorimetry is used to quantify the heat release of the Al-based mixtures under low heating rates, where Al is oxidized without ignition. These measurements are essential for understanding complex reaction mechanisms since they link the nano/micro scale of the reactants to the macro scale of the mixture. The reaction kinetics and the underlying mechanisms are determined by combining the experimental findings with fundamental theory relevant to solid state processes.

Thirdly, semi-empirical models are developed to estimate the kinetics of ignition and combustion of the Al particles in the various oxidizers, based on the fundamental understanding of these reactions, solid state kinetics, and experimental findings. These models are not high fidelity

simulations of the chemical and physical processes of the reactions due to the limited understanding of this field. Instead, the models focus on the elementary and rate-controlling mechanisms that drive the kinetics of these reactions.

2. Literature Review

This chapter provides a background on the effects of particle size on the properties of aluminum, a review of experimental findings on the reactions between Al and oxygen, Al and metal oxidizers, and Al and water, and a summary of the potential applications of these mixtures.

2.1.Effects of particle size on properties of aluminum

When the particle size is reduced to the nano scale, the number of surface atoms and the specific surface area increase significantly; consequently, the surface energy becomes a significant part of the internal energy. This affects the thermodynamic, electro-chemical and mechanical properties of the particle. Figure 2.1 illustrates the melting temperatures of Al nanoparticles fitted to the theoretical melting temperature curve calculated via the Gibbs-Thomson equation [1]. The melting temperature dependence on particle size can be used to determine the surface energy and enthalpy by thermal analysis, assuming that the surface energy lowers the activation energy for melting [30]. Experimentally, the oxidation of zinc sulfide nanoparticles indicated a linear decrease of the activation energy with the particle size reduction [25], which was shown to be due to the large surface energy and entropy of the nanoparticles. Furthermore, as the particle's specific surface area increase, its cohesive energy decreases. This affects the reaction enthalpy, which is computed theoretically in Figure 2.2 [2]. The enthalpy of oxidation can be enhanced when nano scale Al oxidizes to bulk scale Al_2O_3, since the cohesive energy is reduced and no lattice energy is required to break-up the crystal structure of the alumina.

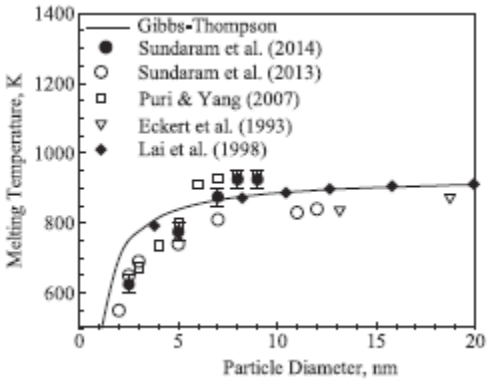

Figure 2.1: Effect of particle size on melting temperature of Al [1]

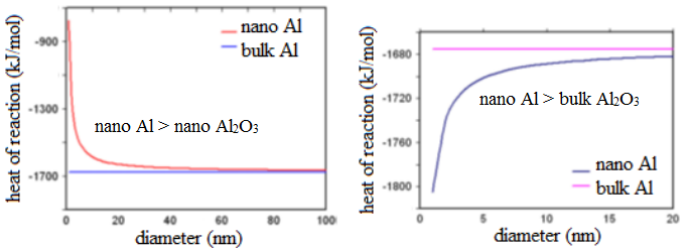

Figure 2.2: Size dependence on the enthalpy of oxidation of Al [2]

The Al particle size also has significant contribution on the effective heat and mass transfer processes. At the nano scale, the collisions between the particle and the gas molecules are significant, and the Knudsen number must be considered

$$Kn = \frac{\lambda}{d_p} \qquad \text{(Eq. 2.1)}$$

where λ is the mean free path of the gas molecule, and d_p is the particle diameter. Generally, the continuum regime exists for $Kn < 0.01$ where collisions between gas molecules are dominant, and the free molecular regime exists for $Kn > 10$ where collisions between the gas molecules and the particles are dominant [7]. Figure 2.3 illustrates the dependence of the continuum and free molecular regimes on the particle size and pressure. Appropriate equations for the heat and mass transfer processes (i.e. thermal conduction, mass diffusion) must be used depending on the regime. In the transition regime, Fuch's model is generally used; this model balances the heat and mass transfers between the two regimes at a distance of one mean free path from the particle surface [7].

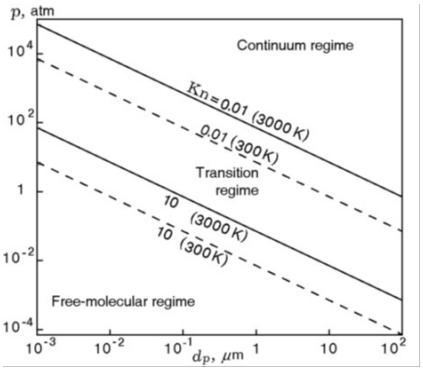

Figure 2.3: Particle size for continuum and free molecular regimes [7]

The active content of aluminum is significantly affected for particles below 100 nm, as shown in Figure 1.3. Micron sized Al particles can have ~99% active aluminum by mass, whereas 40 nm particles are only ~60-70% active by mass [31]. The active content can be lower than 50% for particles below 50 nm [32]. The significant alumina mass affects thermodynamic properties such

as heat capacity and heat conductivity. Furthermore, Al nano powders have much lower thermal conductivity due to their low bulk density. It has been shown that the thermal conductivity and light absorption coefficient of consolidated Al nanoparticle pellets increase almost linearly with their packing density [31]. Porosity is another important parameter that affects the ignition and combustion properties of Al particles or Al-based thermites. Porosity is related to the bulk density of the sample, as a percentage relative to the theoretical maximum density (TMD). The TMD of a thermite mixture is calculated as the weight average of the reactants densities in solid state. Experimental data indicated that flame propagation increases with density in micron thermites due to the increased thermal conductivity, but decreases with density in nanothermites [33]. The decrease of the flame speed with bulk density in nanothermites was explained by a change of the dominant heat transfer mechanism from mass convection to heat conduction [34]. It is important to investigate the effective diffusivity of oxygen when mass convection is a rate determining mechanism for combustion. The effective diffusivity, D_e, is a function of porosity, and largely dependent on the Knudsen number. For example, the free molecular Knudsen diffusivity was implemented in the combustion of consolidated Al nanoparticles [35]. However, a more advanced model to estimate D_e was proposed in [36] based on the pore size distribution of a microstructure. This model uses the continuum domain diffusivity (e.g. between agglomerates) and Knudsen diffusivity (e.g. within the agglomerates).

Given the importance of Al particles size, it is important to determine the particle size distribution of nano powders. Nano size particles tend to follow the log-normal distribution [37], given by

$$f(d_p) = \frac{1}{\sqrt{2\pi}\sigma d_p} e^{\left[-\frac{1}{2}\left(\frac{\ln d_p - \mu}{\sigma}\right)^2\right]} \quad \text{(Eq. 2.2)}$$

where μ and σ are the particle's mean diameter and standard deviation, respectively. The mean particle diameter can be found experimentally from scanning electron microscopy or photon correlation spectroscopy. Also, the specific surface area can be determined using gas adsorption [38] [39]. However, it should be noted that nanoparticles sinter more readily and the intensity of light scattered is proportional to d_p^6 [40].

2.2.Experiments with micro/nano aluminum reacting in air/oxygen

Controlled oxidation of Al nanoparticles is generally performed using Thermogravimetric Analysis and Differential Scanning Calorimetry (TGA/DSC) at the low heating rates of 5 to 40 ˚C/min [41] [42] [43]., whereas ignition experiments are generally performed under the high heating rates of 10^3 to 10^6 ˚C/min using reflected shockwaves [44], temperature jump (T-jump) with Pb wire [45], aerosol flow reactor [46], or laser ignition [32] [47]. The TGA/DSC is a highly controlled environment where the flowrates of air/oxygen can be controlled; the apparent activation energy, onset of phase transitions and the energy release can be obtained from this data [48]. The oxidation kinetics of Al micro and nanoparticles using TGA/DSC was modelled by various researchers [49] [43] [50] [51] [26]. The major assumption is that Al particles oxidize homogenously and the mass rate of oxidation is related to the diffusional flux of Al or O_2 across the Al_2O_3 shell [52] [53] [19] [43] [54], based on the unconstrained core-shell model (i.e. both Al and O_2 can diffuse) [20]. However, the apparent activation energy for oxidation can be much higher if the particle size distribution and particle agglomeration are significant [50]. The oxidation of micro and nano Al powders under constant heating rate indicates a 3-stage oxidation curve. Low temperature oxidation is initialized kinetically by reactions on the particle surface

[52] or by diffusion of O_2 through the Al_2O_3 shell [49]. Medium temperature oxidation (up to the melting temperature of the Al core) is complex; this stage has been shown to be dependent on the rate of crystallization of the Al_2O_3 shell [43]. The high temperature oxidation was shown to be governed by the diffusion of molten Al and subsequent oxidation outside the particle [20] [49]. These stages of oxidation are shown in Figure 2.4 [49]. The phase transformations in the Al_2O_3 shell and melting of the Al core have significant contributions on the kinetics of oxidation. In TGA/DSC experiments, an intermediate stage between the low-temperature (amorphous shell) and high-temperature (crystalline shell) oxidation is controlled by phase transformation assisted diffusion [43] [49] [19] [26]. Some researchers considered the stress forces at the Al/Al_2O_3 interface upon melting of the Al core. It was found that fast oxidation is caused by a combination of enhanced diffusivity of aluminum and pressure gradients within the alumina shell [53]. Furthermore, the enhanced diffusion of Al into Al_2O_3 is also a stress relief mechanism [55]. Furthermore, it has been suggested that Al particles smaller than 3 μm never experience tensile stress because the timescale of oxidation is faster than the timescale of thermal expansion [56]. The melting of Al combined with the partial oxygen pressure plays an important role on the reaction. Nano powders were slowly oxidized at the very low O_2 pressure of 0.2 mbar in argon, and ignited in atmospheric air [57]. It should be noted that the melting temperatures of bulk aluminum and alumina are 993 K and 2345 K, respectively. The physio-chemical processes at the interface between the Al core and the Al_2O_3 shell are critical on the ignition and combustion processes [55] [58]. Generally, nano Al particles ignite around the melting temperature of the

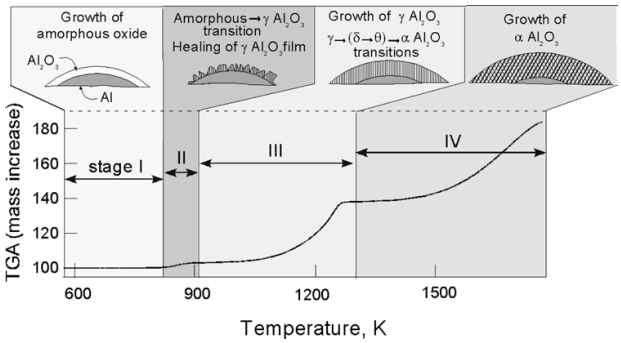

Figure 2.4: Stages of oxidation of Al particles [49]

aluminum core, whereas micro Al particles ignite around the melting temperature of the alumina shell [59].

It has been hypothesized that the melting of Al core combined with phase transformations in the Al_2O_3 layer cause early ignition in Al nanoparticles since partial combustion was observed in 150 nm Al particles at heating rates above 8 °C/min [41]. This theory agrees qualitatively with the results of oxidation of 40-60 nm Al particles via hot-stage TEM, which indicated that ignition initiates most probably with the melting of the aluminum core that causes rupture in the alumina shell [42]. Similarly, it has been proposed that the mechanical stability of the alumina shell determines the onset of combustion. On the other hand, molecular dynamics simulations illustrate that oxidation is initiated via localized hot spots that form due to the high exothermicity of the Al-O_2 reaction [60]. The hot spots created void spaces near the outer surface of the particle, which then reduced the activation energy for the diffusion of oxygen by an order of magnitude. Figure 2.5 illustrates the reaction mechanism, supported by TEM images, of Al nanoparticles at high heating rates [61]. The original Al nanoparticle in Figure 2.5a expands upon melting of the Al core, as shown in Figures 2.5b and 2.5f. The Al_2O_3 shell ruptures due to the tensile forces, as shown in Figures 2.5c and 2.5g, and Al reacts with the air/oxygen. The expanded particles is hollow since most Al oxidizes near the Al_2O_3 surface (Figures 2.5d and 2.5h), and eventually fractures into nano clusters of Al_2O_3 and partially oxidized Al (Figures 2.5e and 2.5i).

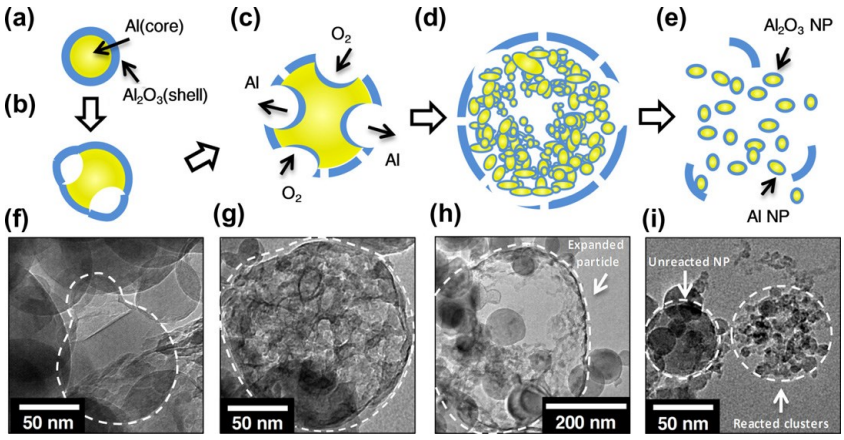

Figure 2.5: Reaction mechanism of Al nanoparticles at high heating rate [61]

The effect of the Al particle size was investigated in [62]; an increase in the ambient O_2 temperature or pressure reduced the ignition delay and burn time, which indicated a transition from diffusion to kinetic controlled combustion as Al particle reaches the nanoscale. Similarly, pyrometry measurements of 80 nm to 40 μm Al particles ignited behind a reflected shockwave were performed in [62] and indicated a transition from vapor phase diffusion to heterogeneous reactions on the particle surface. The temperature of burning particles below 20 μm was near the boiling point of Al, whereas the temperature of the nanoparticles was near the environment temperature. Also, the combustion of bimodal nano and micro sized Al particles in stabilized Bunsen flames in air [63] showed that Al nanoparticles ignite at much lower temperatures than the micron counterparts. A comprehensive literature review related to the oxidation and combustion of Al micro/nanoparticle is tabulated in [41] and a summary of the proposed oxidation and ignition mechanisms is available in [64] [65].

2.3.Reaction mechanisms of aluminum micro/nano particles reacting in air/oxygen

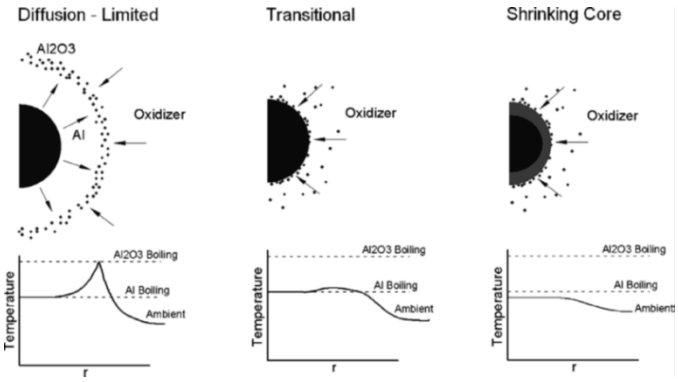

Figure 2.6: Reaction mechanisms of Al particles [62]

The reaction mechanism of Al particles is highly dependent on the particle size as shown in Figure 2.6 [62]. Large particles (d_p>10 μm) burn in the gas-phase, and a detached flame develops around the particle at a standoff distance controlled by the diffusivity of aluminum gas. The flame temperature reaches the boiling point of alumina [21], and the burning time is proportional to d_p^2 [46]. However, since diffusion length scales reduce for smaller particles (d_p≈1 μm), the

role of chemical reaction rates becomes important [10]. This is the transitional stage, where combustion is controlled by heterogeneous reactions on the surface, and the flame temperature is near the aluminum boiling point. At the nanoscale, the shrinking core model has been proposed. The oxidizer diffuses through the alumina shell and chemical reactions occur at the aluminum-alumina interface. In this case the flame temperature is highest within the particle core, and the burning time is strongly dependent on the external temperature and pressure [7]. At very high heating rates ($>10^6$ K/s), the fast burning times on the order of μs were independent of particle size and could not be explained by the diffusion mechanism [66] [67]. A new mechanism was suggested, called melt-dispersion, where tensile stresses upon melting of the Al core shatter the Al_2O_3 shell, and the produced nano clusters of aluminum react directly with the oxidizing atmosphere.

A common method of analyzing the oxidation/combustion of an Al particle is to consider the rate of mass and energy transfer around a spherical particle [7] [59]. It is assumed that the particle oxidizes homogenously while maintaining its core-shell structure. Details of the core-shell model with equations for kinetic or diffusive controlled burning rates are readily available [59]. A general combustion theory of Al particles at the nano scale must contain heat transfer equations in the molecular and continuum regimes. These equations are summarized in the literature [7] [3]. Studies of the oxidation of micro and nano Al powders under low heating rates indicated that diffusion of O_2 and Al in the Al_2O_3 layer are rate limiting [52] [53] [19] [43] [54]. Also, the combustion kinetics of laser ignited consolidated pellets made of Al nanoparticles were shown to be controlled by the diffusion of O_2 through the porous structure [35]. Theoretically, it was shown that the ignition temperature of a single isolated Al nanoparticle is just above the melting temperature of the aluminum core [68].

2.4.Experiments with aluminum based thermites

A major limitation of conventional or micron sized Al powders and the related thermite is that the burning rate is slow. The flame speeds in nanothermites are 3 orders of magnitude higher compared to the micro thermites. The enhanced flame speed can be explained by reduced diffusion distances at the nano scale and increased interface area between the Al and the metal oxide [69]. The effect of Al particle size on the burning rate of Al/MoO_3 nanothermites was investigated in [32]. Al particles less than 50 nm burned at 2 m/s, whereas larger nanoparticles burned at 10 m/s. Ignitions of Al/CuO nanothermites coated on Pt wires at high heating rates led to ignition delays on the order of micro seconds, which were proportional to the oxide thickness; this result supports a diffusion controlled mechanism [70], contrary to the melt dispersion mechanism [66]. The combustion of Al/CuO nanothermites under constant volume illustrated that the pressure signal leads the optical emission signal; this was explained by the full decomposition of CuO at temperatures below the adiabatic flame temperature [71]. Similarly, electrically heated nanothermite coatings showed that CuO decomposes prior to ignition but only at heating rates higher than 2000 ˚K/s [72]. Figure 2.7 illustrates the effect of the heating rate on the ignition of Al/CuO nanothermites [72]. It can be seen that as the heating rates increases, the decomposition of CuO before the ignition of Al is more pronounced. Moreover, 3 modes of combustion were identified for lightly packed Al/CuO mixtures; the combustion velocity decreased from 1000 m/s to 2 m/s by increasing the surrounding inert gas pressure [73]. Convection was shown to be dominant at low (near atmospheric) pressures and

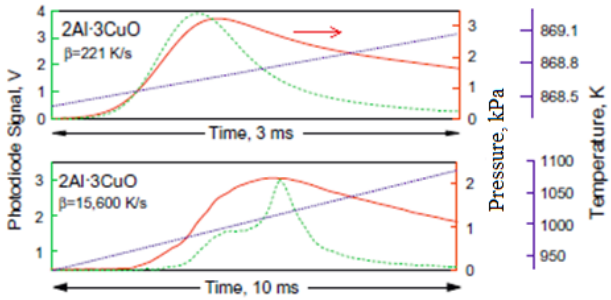

Figure 2.7: Effect of heating rate on ignition of Al/CuO nanothermites [72]

thermal conduction to be dominant at high pressures. The observations above suggest a gas-solid reaction mechanism. However, the burning rates of high density Al/CuO pellets were uniform with the nitrogen pressure [74]. T-jump experiments of Al/CuO nanothermites ignited at high heating rates (10^5 K/s) indicated that chemistry and energy release are controlled by a mechanism of large particle formation [75] since 85% of the products were micro sized. These observations suggest a condensed phase reaction mechanism.The bulk density of the nanothermite mixture has a dominant effect on the flame propagation mechanism. Experimental data showed that the flame velocity decreases from ~1000 m/s to ~1 m/s as bulk density increases, and the heat transfer mechanism changes from mass convection to heat conduction. Figure 2.8 illustrates that Al/MoO_3 micron thermite have higher flame velocity in denser mixtures; this was explained by the enhanced thermal conductivity [33] [76]. However, the nanothermites show opposite trend, and this was explained by the changing combustion mechanism from heat/mass convection to heat conduction [33] [13]. At high bulk densities, numerical modeling of the flame speed of Al/MoO3 based on the heat equation provides similar burning speeds (order of 1 m/s) as those obtained in experiments [77]. However, simple scaling arguments in [164] suggest that burning speeds on the order of 100 m/s can only be sustained by the transport of the condensed phases to the unreacted zone, since energy transfer via heat conduction and product gas convection/condensation is not enough to ignite the adjacent reactants. At low nanothermite densities, burn tube experiments indicated that convection is the dominant transport mechanism [78], and the reduced particle size was elementary for enhancing

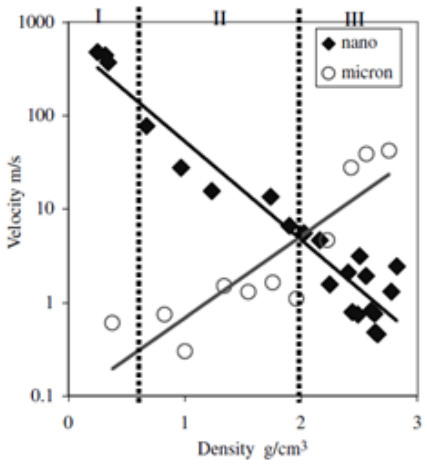

Figure 2.8: Flame propagation velocity in Al/MoO3 micro and nanothermites [33]

convection [79]. Furthermore, Al/CuO and Al/MoO_3 nanothermites ignited in burn tubes had faster flame propagations with decreasing the size of the oxidizer particles, rather than the size of the Al particles [12]. This result suggests that gas generation via decomposition or sublimation drives the combustion front via a convective mechanism. Some authors believe that the reaction is driven kinetically by the melt-dispersion mechanism in convective burning [66] [67], where the alumina shell breaks, and Al clusters are dispersed ahead of the flame front. Also, Al/MoO_3 nanothermite powders ignited in burn tubes illustrated that stoichiometry has a large effect on the mode of propagation [80]. For equivalent ratios (ER) of 0.2 to 3, a supersonic convective drive propagation front was observed, whereas in the highly rich mixtures (ER of 7 to 10) the reaction front speed was on the order of 1 m/s.

2.5.Reaction mechanisms of Al/CuO thermites

The reaction mechanism between Al and CuO is complex since the reactions can initiate at the Al/CuO interface, or by the decomposition of CuO into Cu_2O and O_2 followed by the reaction between the gaseous oxygen and aluminum. Several theories have been proposed to explain the combustion behavior in nanothermites: the melt-dispersion mechanism that disperses Al clusters in the unreacted mixture after spallation of the Al_2O_3 shell [66], a convection mechanism driven by the intermediate gas species that carry condensed species into the unreacted mixture [164], combined effects of heat convection and conduction that causes unstable propagation fronts [73]. However, these theories are in the infancy phase and have not been fully validated.

At the molecular scale, in-situ transmission electron microscopy of rapidly heated Al/CuO [28] and Al/WO_3 [81] nanothermites revealed a reactive sintering mechanism as illustrated in Figure 2.9 [28]. In this mechanism heat is transferred away from the fuel/oxidizer interface, which then melts and possibly dissociates the adjacent Al and metal oxidizer, respectively. Then, surface

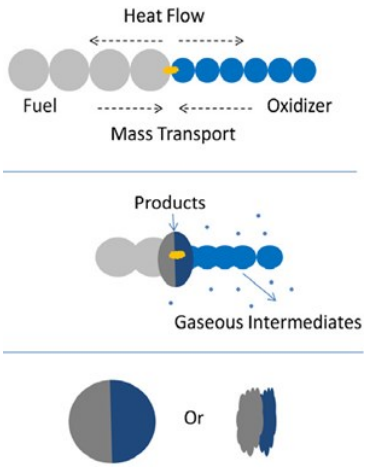

Figure 2.9: Reactive sintering mechanism [28]

tension and capillary forces deliver new material to the reacting interface. The final morphology of the products is dependent on the local temperature, cooling rate and stoichiometry.

Several nanothermite mixtures coated on a Pt wire and ignited via T-jump indicate that oxygen release from the metal oxide is not a necessary prerequisite for ignition [11]; however, as shown in Figure 2.10, the ignition temperature of Al/CuO nanothermites has been correlated to the O_2 release temperature from CuO. In another study, the activation energy for O_2 release decreased at very high heating rates, which indicated mass-diffusion limitations [82]. In order to account for the kinetics of the reaction, the effective activation energy should account for both the oxygen release and the chemical reaction. In [83] and [84], new methods to prepare core-shell Al/CuO thin film nanorods are described, and these nanothermites display several low-temperature reactions before the main exothermic reaction. At low heating rates, four reaction steps were observed in Al/CuO combustion. It was suggested that the decomposition of CuO is the first step due to low activation energies, and that ignition is reached when 4% of the reaction enthalpy is released [85]. Furthermore, ignitions of dense nanothermites showed that ignition temperatures increase while pressurization rates decrease with the heating rate [72]. The authors postulate that low temperature reactions prior to ignition alter the transport properties of the alumina layer and have important contribution on the ignition mechanism. Recently, a new criterion for ignition of Al-

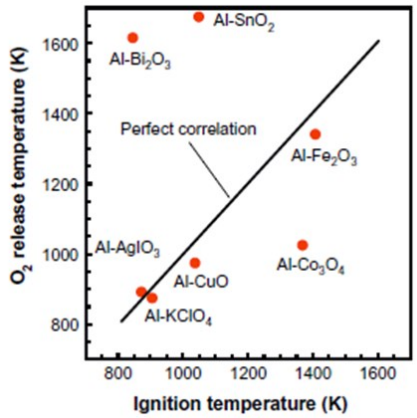

Figure 2.10: Oxygen release and ignition temperatures in nanothermites [11]

based nanothermites has been suggested [45]. By measuring the heating rates before and after ignition and assuming Arrhenius kinetics, it was suggested that the reaction rate constant is independent of the type of oxidizer ($R_C \sim 5.8 \cdot 10^{-2}$ mol/m^{2}s*)*. This result indicates that the ignition temperature only reflects the conditions for thermal runaway.

2.6.Experiments with micro/nano aluminum reacting in water

The role of the Al particle size on the kinetics of hydrogen generation from Al/water reactions at 55 ˚C was investigated in [86]. It was found that the H_2 evolution increased by decreasing the particle size, and also the induction time was reduced. The reaction mechanism of nano and micro-sized Al powders with water and the role of particle size were investigated in [86] [87]. It was found that H_2 evolution at low temperature is highly dependent on particle size. At a temperature of 60 ˚C, Al powders with mean diameter of 98 nm were fully reacted in 1.9 hours, whereas powders with mean diameter of 2.25 µm produced only 74% yield after 8 hours. Figure 2.11 illustrates that the hydrogen yield is highly dependent on the Al particle size [86]. A two-stage reaction mechanism was found, where the rate is first controlled by the chemical reactions on the Al surface, and then by diffusion of OH^- and H_2O through the byproduct layer [87]. Similarly, the Al/water reactions at 100˚C showed a two-stage mechanism [88], and a multi-step mechanism for Al particles of 100 to 10 µm diameter [86]. The apparent activation energy of these reactions is size dependent. However, Arrhenius kinetics of the maximum H_2 flowrate indicated that activation energy is 41 kJ/mol and independent of particle size, such that the reaction rate is proportional to the specific surface area [22]. Low temperature isothermal

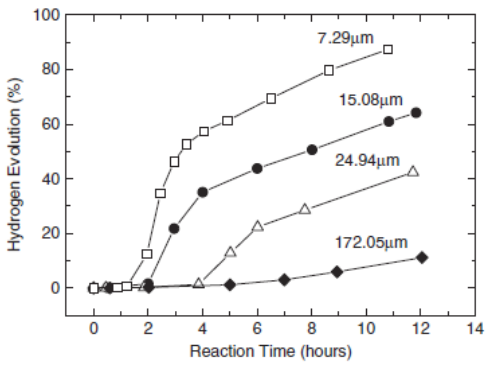

Figure 2.11: Size dependent hydrogen yield for Al/water reaction [86]

calorimetry and differential scanning calorimetry experiments showed that the reactions in liquid water occur at the Al/hydroxide interface and follow the shrinking Al core model [23], and followed two fast reaction stages and termination [89]. However, the rate-controlling mechanism could not be explained by a single step since mass diffusivities through the growing bayerite layer varied with time and particle size. Under atmospheric pressure and below the boiling temperature of water, micro Al particles formed laminate structures of $Al(OH)_3$ [17], whereas the nano Al particles formed highly porous fibrous spheres of AlOOH [90]. Also, it has been shown that Al reacted in distilled water produced significantly higher hydrogen yield compared to tap water due to the increased solubility of the alumina shell [91]. The kinetics of self-heating 100 nm Al nanopowders in liquid water indicated that spontaneous self-heating begins at a temperature of 64 to 66 ˚C [92].

Some methods such as mechanical activation [24] [93] [94] have been investigated to increase the reaction rates by optimizing the surface area at the Al/hydroxide interface and increasing the mass diffusion of OH ions and H_2O molecules through the by-product layer. An optimal milling time was found to optimize both the lattice imperfections and the porosity of the microstructure, and fine and deformed grains with more grain boundaries had more affinity for the reaction. It was found that manual grinding process yields needle-like crystals, whereas mechanical activation via ball milling lowered the particle size by an order of magnitude [94]. Figure 2.12 illustrates that the rate of H_2 production is significantly higher and induction period is shorter for the ball milled Al powders due to the enhanced mechanical activation [94]. Also, reactions with

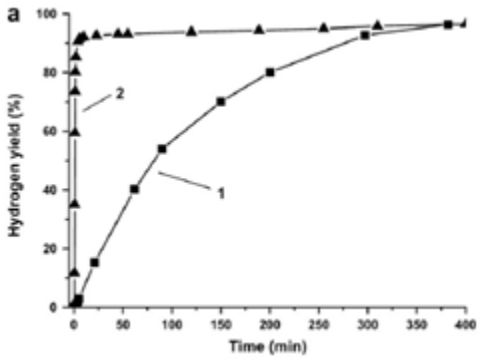

Figure 2.12: Hydrogen yield for grinded (1), and ball milled Al powders (2) [94]

protective salt layering proceeded at significantly higher rates since NaCl prevented the formation of the aluminum oxide [95]. Alternatively, the rates of hydrogen production were increased in acidic/alkaline amphoteric water electrolysis with reduced energy consumption and electrode polarization [96], in alkaline solution such as NaOH and KOH [97], by mixing the Al with metal hydrides [98] [27], catalyzing with Co [27], Na_2CO_3 [99], $Al(OH)_3$ [100], $Al(OH)_3$, gamma-Al_2O_3 or alpha-Al_2O_3 [101] or graphene modified Al particles [102]. The Al_2O_3 layer dissociated in the alkaline solution and the reaction rate was first order with respect to the OH concentration. Similarly, water dissociated faster on the surface of $Al(OH)_3$ or crystalline Al_2O_3 phases to produce AlOOH, such that the activation energy for the reaction was reduced from 158 kJ/mol to about 75 kJ/mol [103]. On the other hand, metal hydrides such as Bi and CaH_2 formed micro-galvanic cells that accelerated the corrosion of the Al anode. The addition of LiOH and $Ca/Ca(OH)_2$ solutions at the low temperature of 25 ˚C increased the reaction rates due to the continuous production of OH^- ions [104].

2.7.Reaction mechanisms of micro/nano aluminum reacting in water

The reaction between the Al and H_2O is extremely slow due to the coherent Al_2O_3 passivation layer around the Al core. Hence the key to maintain the reaction is the continual removal or disruption of the Al_2O_3 layer. There are two mechanisms for hydration: pitting and uniform corrosion [105]. In the pitting mechanism, the oxide film goes through localized breakdown due to anodic polarization, where OH^- ions are driven to the Al/Al_2O_3 interface faster than the oxidation of Al. The mechanism of H_2 evolution during anodic polarization is described in reference [106]. The kinetics of pitting is highly dependent on the structure of the Al_2O_3 shell. In the uniform corrosion model, there is an induction period where the Al-O bonds are replaced by Al-OH, followed by the rapid formation and growth of the hydrated alumina film, AlOOH,

which reaches the Al surface. The uniform corrosion model has been used to explain the hydrogen generation rates in the Al/water reactions at atmospheric pressures in references [17] and [87]. It has been further suggested that H_2 formed at the $AlOOH/Al_2O_3$ interface must reach a critical pressure to break the hydrated oxide film, such that Al comes in direct contact with H_2O. This is a critical step for self-sustaining the reaction, which is particle size dependent, such that the H^+ ion diffusion does not reach the solubility limit in the Al (i.e. equilibrium) [107].

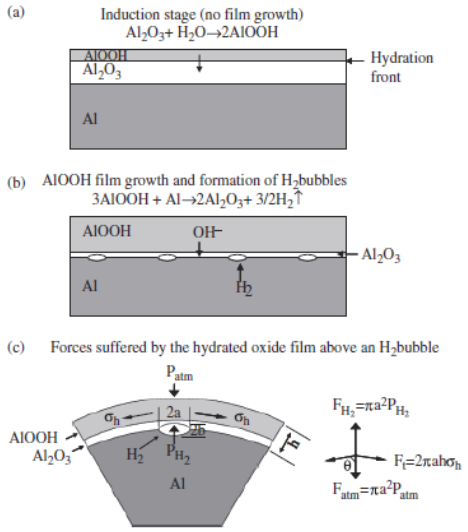

Figure 2.13: Reaction mechanism between Al and water [17]

A summary of the proposed reaction mechanism between Al and H_2O is illustrated in Figure 2.13 [17]. There are 3 major steps: (1) hydration of the Al_2O_3 shell surrounding the Al core replaces the Al-O-Al bonds with Al-OH. The hydroxide species AlOOH and $Al(OH)_3$ are produced since they are more thermodynamically stable than Al_2O_3 under ambient conditions. This induction stage is shown in Figure 2.13a; (2) OH^- ions are driven to the Al/Al_2O_3 interface by the internal anodic potential, and then react with Al via an electro-chemical process. This contributes to the film growth. The hydroxide reacts with Al on its surface to generate H_2 as shown in Figure 2.13b. The H_2 bubbles produced diffuse through the Al core. However, since the solubility of H in Al is low, the H_2 accumulates at the interface; (3) the pressure in the H_2 bubbles must reach a critical value given by the force balance shown in Figure 2.13c. It should be noted that large Al particles have larger critical pressure and larger H_2 bubbles due to larger tolerable extension of the oxide film [87]. The critical gas pressure is reduced if the surrounding pressure or the tensile strength of the hydrated oxide film is decreased. A similar mechanism was proposed in the late 1960s [108]. Three

essential steps are proposed: 1) amorphous oxide formation, 2) dissolution of the amorphous oxide, and 3) precipitation of aluminum hydroxide. The dissolution of amorphous oxide is limited by the hydrolysis of Al-O bonds for pH below 10, and by diffusion of OH^- ions to the surface for pH above 10.

2.8.Applications for Al based thermites and Al/water mixtures

Some notable applications of aluminum powders and aluminum based energetic materials include micro joining [109], MEMS, pyrotechnics [110], micro-igniters [111] [112], actuation in micro-fluidic pumps [113], propulsion [114] [115], and on-demand hydrogen generation [14] [116]. The type of oxidizer has major role on the thermodynamics and reactivity of the Al-based mixture.

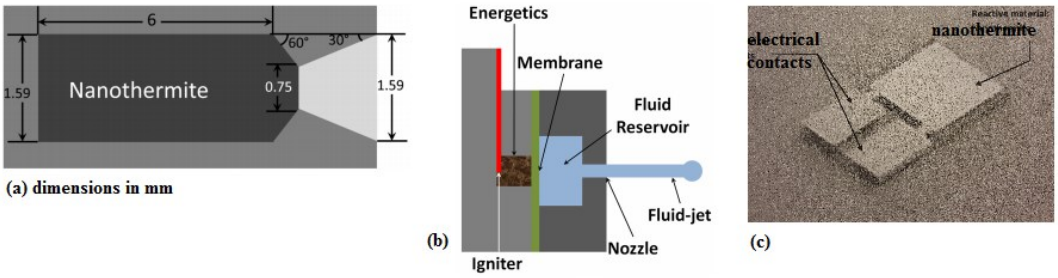

Figure 2.14: Applications of porous nanothermite structures a) micro-thruster [113], b) micro-fluidic jet injector [113], and c) micro-igniter [64]

Figure 2.14 illustrates some potential configurations for porous nanothermite structures. The micro-thruster in Figure 2.14a contains Al/CuO is pressed at various densities from 20% to 80% TMD. At low packing pressure the thrust was 75 N over a period of 50 μs, whereas at high packing pressure the thrust was 3 to 5 N over a period of 1.5 to 3 ms. In both cases the weight specific impulse was 20-25 s [113]. Such micro-thrusters have potential applications in space for controlling the altitude of small satellites with precise thrust impulses. The micro-fluidic jet

injector in Figure 2.14b contains nanothermite, which produces gas once ignited to stretch an elastic membrane that creates a fluid jet through a converging nozzle. Such smooth actuators can control the fluid flow in the micro-channels of a lab-on-a-chip, a device that includes multiple laboratory functions on a single chip. In such application the rate of pressurization must be carefully controlled, and this is directly related to the kinetics of the reaction and flame propagation in the nanothermite. The micro-igniter in Figure 2.14c has a thin nanothermite film deposited on a glass substrate. LAAS-CNRS first proposed the idea of pyroMEMRS (micro-electromechanical system) to integrated solid propellants on silicon-based devices to provide heat and pressure bursts in fast impulse actuators [64]. Such micro-igniters can be used in military applications such as missiles and rockets, or civilian applications such as triggering the inflation of automobile airbags. These applications require fast and reliable ignition time, and this is directly related to the ignition kinetics of the nanothermite.

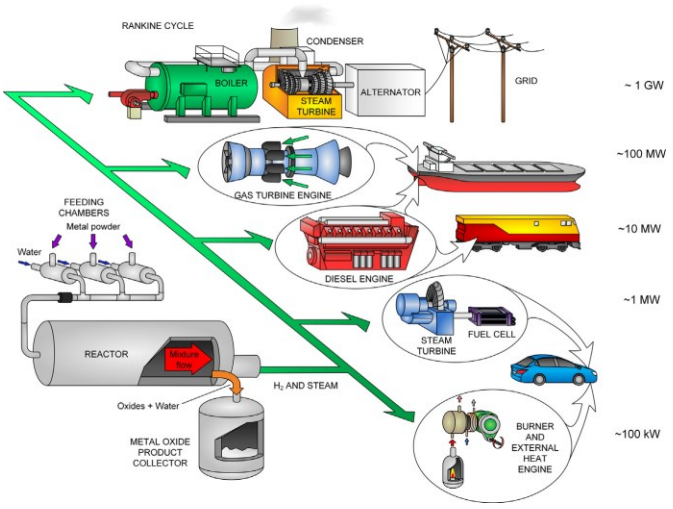

Figure 2.15: Possible applications for high-temperature aluminum-water reactions [14]

Figure 2.15 illustrates the possible applications of the high-temperature Al/water reaction for on-demand hydrogen generation [14]. The H_2 gas and steam are moved from the high-pressure zone inside the reactor and the solid state by-products are collected. Hydrogen fuel can be used on a variety of power scale, from a fuel cell on the order of 100 kW to a Rankine cycle on the order of 1 GW. Furthermore, Al/water reactions can be used for space propulsion if the equivalence ratios are near stoichiometric, since these mixtures were ignited and self-deflagrated

in argon or air with a combustion front velocity on the order of 1 to 10 mm/s [18] [117] [118]. The weight specific impulse was on the order of 40 to 100 s [119].

3. Methodology

The methodology for this research is divided into two sections: an experimental section that describes the materials and methods of preparation, apparatus and experimental setup, and a theoretical section that describes the specific equations that were used to model the reactions of Al powders in air, Al/CuO and Al/water mixtures.

3.1.Experimental

Commercially available Al powders were used in all experiments, and the mixtures were prepared in ethanol via ultra-sonication. Specific apparatus were used and experimental setups were designed for this research, with the intent of monitoring the reactivity and extent of the Al based mixtures. These apparatus and experimental setups are summarized below.

3.1.1. Materials and preparation

Aluminum powders with APS (aerodynamic particle size) diameters of 40 nm and 1 μm, and copper oxide powders with APS diameters of 40 nm, were purchased from US Research Nanomaterials Inc. The Al powders were ultra-sonicated in ethanol or hexane for 20 min to reduce agglomeration. The suspensions were dried on an evaporating plate in a fume hood overnight, followed by over or plate heating at 60 ˚C for 30 min to remove adsorbed moisture. A similar procedure was used to prepare the Al/CuO mixtures, but the Al and CuO powders were sonicated together at various equivalence ratios, to improve the mixture homogeneity. The as-prepared samples of Al and Al/CuO mixtures were mechanically consolidated in a pellet cast (6mm diameter) using a hydraulic press. The packing densities were regulated by the applied pressure, and the final densities were compared to the theoretical maximum density (TMD). The TMD is the volume weighted average of all the species in the mixture (Al core, Al_2O_3 shell, and

CuO). For the Al/water reactions, the powders were sonicated in distilled water for 5 min at various equivalence ratios, to reduce agglomeration and prevent overheating that could initiate the reaction.

3.1.2. Scanning electron microscopy and Energy-dispersive X-ray spectroscopy

Scanning Electron Microscopy (SEM) is a powerful tool for visualizing the morphology of a sample at the nano scale. SEM provides images of a sample by bombarding its surface with high energy electrons. There are two types of detectors used: back scattered electron beam (BSE) and secondary electron beam (SE). The detectors for BSE are coaxial with the incident electron beam, such that scattered electrons with high energy are captured. Since the amount of scattered electrons is proportional to the particle size, samples with high atomic weight appear brighter. This is important for observing the homogeneity of a mixture composed of Al and CuO since CuO particles appear brighter. On the other hand, the detector for SE is on the side of the sample, such that secondary electrons emitted from the sample, with lower energy compared to the BSE, are captured. The SE creates a well resolved image of the surface morphology. The sample should be conductive in order to prevent charge accumulation. The Al particles have to be sputtered with gold since the alumina shell is an electrical insulator.

The SEM can be coupled with Energy-dispersive X-ray spectroscopy (EDX) in order to provide the chemical composition of a sample and the relative concentration of each element in its composition. X-rays are generated when secondary electrons are ejected from the sample's surface due to transition from a higher energy state to a lower energy state. The wavelengths of these X-rays correspond to specific elements. However, EDX can only estimate the relative concentration of each element rather than precise measurements. This is because the X-rays are generated in all directions and may not reach the detectors, and are not always released from the

sample. The amount, density and composition of a sample affect the EDX measurements. SEM and EDX were used extensively to study the morphology of the reactants and products in Al/air, Al/CuO and Al/water reactions.

3.1.3. X-ray diffraction

X-ray Diffraction (XRD) is a technique that determines the crystalline phase of samples. The data provide the peaks of the crystal lattice due to the constructive interferences of the X-rays incident on the sample, according to Bragg's law [120]

$$n\lambda = 2d \sin\theta \qquad \text{(Eq. 3.1)}$$

where λ is the X-ray wavelength, d is the planar spacing of the crystalline phases, and θ is the incident angle of the X-ray. The X-rays sweep at various incident angles and the reflected X-rays are collected. When constructive interferences occur, the collected X-rays have higher intensity. Since θ and λ are known, the values of d can be determined for a given sample, and these can be compared to the database values. For small nano sized crystallites, the reflected X-rays have low intensity, and the constructive peaks are broader. On the other hand, amorphous samples do not have any constructive interference.

3.1.4. Thermogravimetric analysis and Differential scanning calorimetry

Thermogravimetric analysis (TGA) uses a sensitive scale to monitor the mass of a sample during reactions. For example, aluminum reacts with air by absorbing oxygen from the surrounding atmosphere and its mass increases. On the other hand, copper oxide can decompose to cuprous oxide by release oxygen and its mass decreases. TGA can be used to determine the active content of Al particles, assuming the stoichiometric reaction R1 in section 1.1, where the mass of aluminum can be related to the mass of oxygen as $m_{Al} = 1.124 m_{O2}$. The oxygen mass is simply

the mass change, Δm, recorded when the reaction is complete. The active content is determined by the aluminum mass calculated relative to the sample mass of the powder.

Differential Scanning Calorimetry (DSC) measures the heat flow during a reaction under constant heating rate or isothermal conditions. The heat released during an exothermic reaction, or heat absorbed during an endothermic reaction, are disturbances to the surroundings that can be monitored accurately. The heat flow is calculated relative to a baseline (reference crucible without sample) under the same heating conditions and gas flowrates. The DSC data is useful to obtain data on the onset temperature, peak temperature, and reaction rates, melting temperature, and phase transformations, total heat absorbed or released. These parameters provide insight into the ignition and reaction mechanisms, and the kinetics of the reaction. The TGA and DSC can be coupled, and is a fundamental apparatus for studying solid state reactions because it links the kinetics to both mass and heat transfer processes. A Netzsch TGA/DSC, as shown in Figure 3.1, was used to study the controlled oxidation of nano and micro Al particles by varying the flowrates of air.

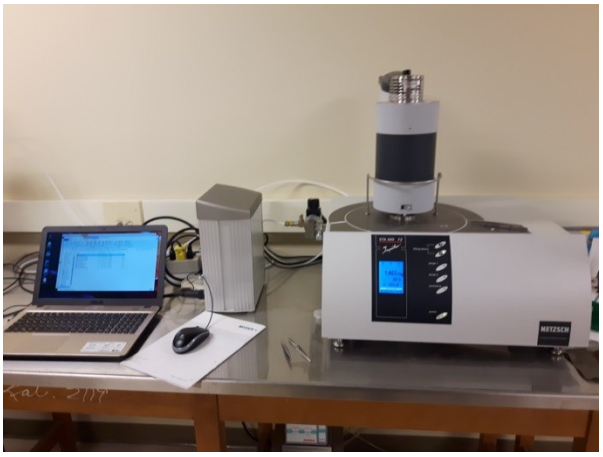

Figure 3.1: Netzsch STA 449 F3 TGA/DSC

It should be noted that the minimum sample mass for this TGA/DSC is 10 mg in order to obtain precise measurements of the mass changes during the reaction. The accuracy of the sample mass is mainly affected by two factors: 1) external disturbances to the sensitive scale inside the apparatus, and 2) the baseline, obtained by an identical heating process and gas flowrates in the absence of a reaction, which corrects the measurements.

3.1.5. Laser ignition with high speed imaging

A custom design high pressure chamber (HPC) was manufactured from stainless steel in order to study the reactions of consolidated Al pellets in air and consolidated Al/CuO pellets in argon under fast heating rates. The HPC was fitted with borosilicate windows and a T-shaped stand at its center to hold the samples. It has a pressure limit of 50 bar. The chamber is vacuumed or injected with air or argon through an intake port, and vaporized products are removed through an exhaust port. A 10W 520 nm diode laser from Ultralasers was used to ignite the sample by heating its top surface. A focusing lens was used to vary the laser power density from ~100 W/cm^2 to ~10 kW/cm^2, and a pulse generator was used to control the duration of the laser beam. A piezoelectric sensor was installed below the T-shaped stand in order to provide force data during the reaction. Two Thorlabs DET10A photodiodes (with 1 ns response time) were used to capture the light emitted during the reaction; one of the photodiodes was fitted with a 488 ± 2 nm transmission filter in order to capture the AlO emission. AlO is an important intermediate in the reaction mechanism of Al and oxygen. A Phantom V2012 high speed camera was placed orthogonal to the axial direction of the sample in order to capture the burning speed and the expansion of the flame plume. The high speed camera recorded at 200,000 fps with a low exposure time of 1 μs, and additional filters such as extended dynamic range (EDR) in order to prevent image saturation. The signals from the laser pulse, the photodiodes and the piezoelectric sensor were captured on a 6ch Tektronix MSO56 oscilloscope with a sample rate of 6.25 Gs/s and a bandwidth of 350 Mhz. The oscilloscope was triggered by the unfiltered photodiode. The setup is shown in Figure 3.2a and its diagram is shown in Figure 3.2b.

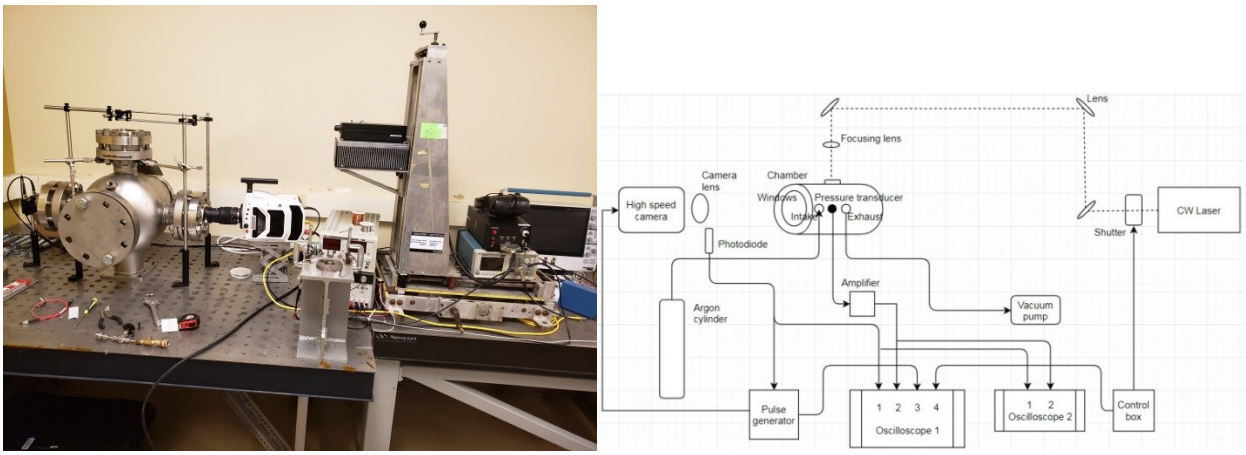

Figure 3.2: a) Setup for the laser ignition and high speed imaging of nanothermites; b) setup diagram

3.1.6. Isothermal micro calorimetry

Isothermal Micro Calorimetry (IMC) is a technique similar to the differential scanning calorimetry. The heat release by the reaction in a vessel is measured relative to a reference vessel. A TA Instruments TAM III micro calorimeter was used to study the kinetics of reaction between Al powders and water under atmospheric pressure. Pre-heated water was added to the Al powder to reduce the thermal disturbances once the vessel is inserted in the isothermal atmosphere. The insertion procedure was outlined in the manuals, followed by a period of 30 to 45 min to reach thermal equilibrium.

3.1.7. Batch reactor

Batch reactor (BR) experiments are useful for studying reactions under constant volume and high temperature and pressure. Al/water reactions were ignited and self-sustained in a 250 mL non-stirred high pressure BR from Parr Instruments in order to prevent water from vaporizing. An external electric heater was used to heat the solution, which stopped automatically once a set temperature was reached. A custom Omega pressure transducer measured the total gas pressure in the reactor, and two Omega type J thermocouples measured the solution and gas temperatures.

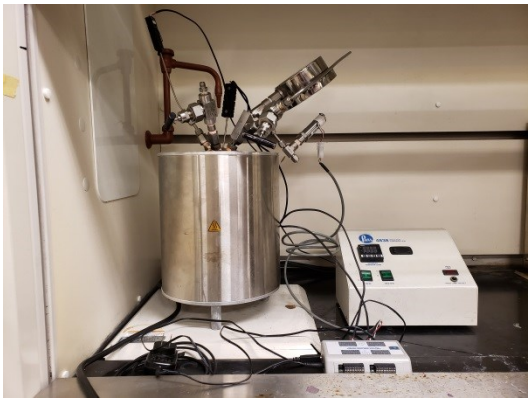

Figure 3.3: Parr Instruments 2650 high pressure/temperature batch reactor

The data was recorded with an Omega USB data acquisition module at sampling rates of 1 to 5 Hz. The hydrogen released from the Al/water reaction was used to study the reaction kinetics. The experimental setup is shown in Figure 3.3.

3.1.8. Definition of terms

The main terms used throughout this thesis and their meaning are summarized below:

Extent of reaction, α: the normalized conversion of reactants into products during a chemical reaction (α = 0 when the reaction starts with 100% reactants, and α = 1 when the reaction completes with 100% products).

Reaction model, f(α): a theoretical equation that describes the mechanism of the reaction, developed from fundamental physics.

Apparent activation energy, E_a (kJ/mol): the amount of energy required to initiate a rate-controlling physical process that results in a chemical reaction; the term apparent means that this is not the real activation energy that describes the elementary reaction in homogeneous systems.

Ignition delay (μs or ms): the difference between the time when the source of ignition is triggered (e.g. laser) and the time when the bulk ignition of the sample is observed on the photodiode or the camera.

Burning time or burning duration (ms): the time required for a reaction to burn as measured by the duration of the photodiode signal at full width at 15% maximum (FW15%M).

TGA mass (mg): the mass of the sample measured by the TGA/DSC apparatus, before, during and after a reaction.

DSC heat flow (a.u. or W/g): the heat release by a chemical reaction normalized by the sample mass, as measured by the TGA/DSC apparatus.

3.2. Theoretical

Heterogeneous reactions of metal particles such as Al/air, Al/CuO and Al/water do not always have a mechanistic model linked to the reaction rate. Generally, the model is determined by combing the experimental data with theoretical equations related to extent of reaction and the rate-determining kinetics. The algorithms and procedures used to measure parameters such as flame speed, burn durations, apparent activation energy, are fundamental for establishing a correct mechanistic model for heterogeneous reactions.

3.2.1. General model for extent of reaction

The progress of a reaction can be related to the reaction rate constant and the rate controlling mechanism as follows

$$d\alpha/_{dt} = k(T)f(\alpha) \qquad \text{(Eq. 3.2)}$$

where α is the extent of reaction ($0 \leq \alpha \leq 1$), $k(T)$ is the rate constant, and $f(\alpha)$ is a the reaction model (a function that defines the rate controlling mechanism). The integral form of the reaction model is given by

$$g(\alpha) = \int d\alpha/_{f(\alpha)} = \int Ae^{-E_a/RT}dt \qquad \text{(Eq. 3.3)}$$

The rate constant is given by the Arrhenius equation

$$k(T) = Ae^{-\frac{E_a}{R_u T}} \qquad \text{(Eq. 3.4)}$$

where A is the frequency factor, E_a is the apparent activation energy, R_u is the universal gas constant, and T is the temperature.

Some common reaction models for solid state kinetics, in differential and integral form, are shown in Table 3.1 below, and derived in reference [121].

Table 3.1: Reaction models in solid state kinetics

Model	**Differential form** $f(\alpha) = 1/k(T)\, d\alpha/dt$	**Integral form** $g(\alpha) = k(T)t$
Power law nucleation	$n\alpha^{1-1/n}$	$\alpha^{1/n}$
JMAK nucleation	$m(1-\alpha)[-\ln(1-\alpha)]^{1-1/m}$	$[-\ln(1-\alpha)]^{1/m}$
Contracting area (2D)	$2(1-\alpha)^{1/2}$	$1-(1-\alpha)^{1/2}$
Contracting volume (spherical 3D)	$3(1-\alpha)^{2/3}$	$1-(1-\alpha)^{1/3}$
2D diffusion	$-{}^{1}/_{\ln(1-\alpha)}$	$((1-\alpha)\ln(1-\alpha)) + \alpha$
3D diffusion (spherical 3D)	${}^{3}/_{[2((1-\alpha)^{-1/3}-1)]}$	$1-{}^{2}/_{3}\,\alpha-(1-\alpha)^{2/3}$
First order reaction	$1-\alpha$	$-\ln(1-\alpha)$

The kinetic parameters A and E_a in the Arrhenius equation Eq. 3.4 can be determined from model or model-free methods. In the model method, the mechanistic process that governs the reaction must be known as shown in Table 3.1. The rate constant is found from the slope of the curve ${}^{d\alpha}/_{dt}\ vs\ f(\alpha)$ or $g(\alpha)\ vs\ t$. Alternatively, the kinetic parameters cam be determined from Kissinger equation assuming first order reaction [122]

$$\ln\left(\frac{\beta}{T_p{}^2}\right) = -\frac{E}{RT_p} + \ln\left(\frac{AR}{E_a}\right) \qquad \text{(Eq. 3.5)}$$

where $\beta = {}^{dT}/_{dt}$ is the heating rate and T_p is the temperature at which the reaction rate is maximized. It should be noted that the Kissinger method can be derived for other reaction models. On the other hand, a master plot fitting method can be used to determine the mechanism, by normalizing the reaction model to its value at $\alpha = 0.5$ [123]

$$g(\alpha)/g(0.5) = \theta/\theta_{0.5} \quad \text{(Eq. 3.6)}$$

where θ is the time function $\theta = \int_0^t e^{-E_a/RT} dt$. The rate-determining model, *g(α)*, has the best fit to the experimental data (i.e. highest and most consistent coefficient of determination). For isothermal experiments, the reaction rate constant is not time dependent and $\theta/\theta_{0.5} = t/t_{0.5}$. For non-isothermal experiments, the heating rate and the apparent activation energy must be known [123]. In the model-free method, a set of kinetic experiments are required to show the dependence of α on temperature (for isothermal data) or on the heating rate (for non-isothermal data). This method is also called the isoconversion method, since the kinetic parameters are obtained at a constant conversion, α. The isoconversion methods are generally derived in the integral form since the differential form is very sensitive to experimental noise [124]. For isothermal experiments, it can be shown that

$$\ln(t_\alpha) = const + E_a/RT \quad \text{(Eq. 3.7)}$$

where t_α is the time required to reach the conversion α at the isothermal temperature T. For non-isothermal data at a constant heating rate, it can be shown that

$$\ln\left(\beta/T_\alpha{}^C\right) = const - E_a/RT_\alpha \quad \text{(Eq. 3.8)}$$

where T_α is the temperature required to reach the conversion α at the heating rate β, and C is a coefficient dependent on the method used to approximate the temperature integral $\int e^{-E_a/RT} dt$; $C = 0$ for the Flynn-Wall-Ozawa (FWO) method, and $C = 2$ for the Kissinger-Akahira-Sunose

(KAS) method [125] [126]. The main drawback of the integral method is that the activation energy is averaged over the range of the conversion process 0 to α; hence its value is not directly related to a unique process. Practical applications of the isoconversion methods are in references [127] [128].

Although heterogeneous reactions are strongly affected by structural defects, nucleation, diffusion pathways, and products' morphologies, the Arrhenius equation is applicable to the kinetics of these reactions. However, the effective activation energy of a heterogeneous reaction is cumulative from individual reaction steps based on their contributions to the overall reaction rate. Furthermore, using the effective activation energy often under-weigh the roles of elementary steps, and the mechanism is characterized by the rate-limiting process only. The resulting kinetic parameters are apparent and dependent on the extent of the reaction.

3.2.2. Core-shell model

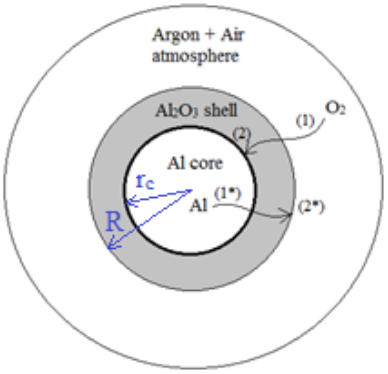

Figure 3.4: Oxidation of a core-shell Al particle

The core-shell model is a mechanistic approach for solid state and solid-gas reactions of spherical particles. It assumes that the product of the reaction forms a uniform shell around the spherical core. Consider an Al particle inside a gaseous argon/air atmosphere as illustrated in Figure 3.4. Assuming that oxygen gets adsorbed fast on the particle surface (i.e. no mass transfer limitations in the gas phase), the Al particle reacts with O_2 according to reaction R1.1. There are two major processes in series [53] [43]: (1) The O_2 or Al (ion) diffusion through the Al_2O_3 shell; and (2) The chemical reaction between Al and O_2. At steady state conditions, the rate of diffusion through the alumina shell is the same as the reaction rate on the surface of Al core. The rate-controlling mechanism is given by the slower process. If

oxidation is controlled by the diffusion of O_2 through the Al_2O_3 shell, the diffusive flux of oxygen can be estimated by Fick's first law of diffusion

$$\frac{dN_{O2}}{dt} = -4\pi r^2 D_e \frac{\partial c_{O2}}{\partial r} \quad \text{(Eq. 3.9)}$$

where r is the radius, D_e is the effective diffusion coefficient of oxygen in alumina (which follows the Arrhenius kinetics as shown in equation Eq. 3.4), and c_{o2} is the molar concentration of oxygen. Since the chemical reaction is very fast, the concentration of oxygen on the surface of Al core is negligible, and Eq. 3.9 can be integrated to obtain

$$\dot{N}_{O2} = \frac{4\pi c_{O2} D_e}{1/r_c - 1/R} \quad \text{(Eq.3.10)}$$

where r_c is the radius of the Al core and R is the particle radius. The molar consumption of O_2 is related to the molar consumption of Al through the stoichiometric reaction R1.1. This diffusion controlled oxidation is equivalent to the 3D diffusion model in Table 3.1.

If oxidation is controlled by the chemical reaction on the aluminum core, the rate of oxygen consumption is given by

$$\dot{N}_{O2} = 4\pi {r_c}^2 c_{O_2} k_s \quad \text{(Eq.3.11)}$$

where k_s is the reaction rate constant at the reaction interface (which follows the Arrhenius kinetics as shown in equation Eq. 3.4). It can be assumed that the concentration of O_2 around the Al core is homogenous since diffusion is much faster the reaction and the reaction order is one [129]. Again, the molar consumption of O_2 is related to the molar consumption of Al through the

stoichiometric reaction R1.1. This reaction controlled oxidation is equivalent to the 3D contracting volume model in Table 3.1.

For constant heating rate, $\beta = dT/dt$, the derivative method is based on rewriting Eq. 3.10 and Eq. 3.11 as

$$Y_{DER}(T) = \ln\left({}^{\Delta m}/_{\Delta T}\right) - \ln\left(f(r)\right) = const - {}^{E_a}/_{R_u T} \qquad \text{(Eq.3.12)}$$

where $\Delta m/\Delta T$ is the mass change with temperature, $f(r)$ is a function of the Al core and the particle radii, r and R respectively: $f(r)=r/(R-r)$ for diffusion controlled and $f(r)=r^2$ for kinetically controlled oxidation, E_a is the apparent activation energy, and T is the sample temperature. E_a is found by linear fitting the $Y_{DER}(T)$ vs 1/T.

An integral method was developed in [130] to model the kinetics of solid state reactions between spherical particles under isothermal conditions. This model is based on the core-shell structure of a reacting particle as illustrated in Figure 3.1, where the rate of change of the core mass is given by the diffusive flux through the shell. The integral model for isothermal conditions is given by

$$Y_{INT}(t) = \frac{\{zr_0^3 + (1-z)(1-x)r_0^3 + C\}^{\frac{2}{3}} - (1-z)\left\{(1-x)^{\frac{2}{3}}r_0^2 - r_0^2\right\} - (r_0^3 + C)^{\frac{2}{3}}}{2(1-z)} \qquad \text{(Eq.3.13a)}$$

$$= Dt$$

where x is the mass fraction of the particle that has reacted, r_0 is the initial core radius, z is the volume of product formed per volume of reactant consumed, D is the effective diffusion coefficient, t is time, and C is the initial product volume normalized by $4/3\pi$. It should be noted that C does not appear in the original derivation [130]; it is used here to represent the initial

oxide layer of the Al particle. For constant heating rate β, an approximate solution to the Arrhenius temperature integral is required, such as Doyle's approximation [126],

$$Y_{INT}(T) = \frac{D_o}{\beta}\int e^{-E_d/RT}dT \approx \frac{D_o}{\beta}\left(\frac{E_d}{R}\right)e^{-5.35-1.05\frac{E_d}{RT}} \quad \text{(Eq.3.13b)}$$

where D_o is the diffusivity pre-exponential, E_d is the apparent activation energy for diffusion, and β is the heating rate. E_d can be determined by linear fitting the natural logarithm $Y_{INT}(T)$ vs 1/T.

3.2.3. Nucleation and growth model

The Johnson-Mehl-Avrami-Kholmogorov (JMAK) equation is a widely known nucleation and growth model that describes the kinetics of crystallization. It can also be used to describe reaction rates when the kinetics depends on the nucleation/growth of the product. Assuming that nucleation occurs randomly in the bulk and on the surface of the material with a constant rate as shown in Figure 3.5, and the growth is homogeneous; then, the extent of transformation is given by

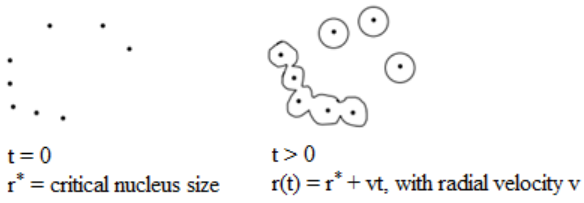

Figure 3.5: JMAK model of nucleation and growth

$$\alpha(t) = 1 - e^{-(k_e t)^m} \quad \text{(Eq.3.14)}$$

where k_e is the effective rate constant for the formation/growth of the nuclei, and m is a parameter that describes the growth dimension. The value of m depends on the rate controlling mechanism. If nucleation is instantaneous, the value of m defines the geometrical dimension of the new phase ($m=1$ for rod shape, $m=2$ for disk shape, and $m=3$ for sphere). However, if nucleation and growth are simultaneous, the values of m can be larger, and non-integer for irregular product morphologies. It was also suggested that m indicates the type of rate-controlling

mechanism at a specific temperature [131] [132]; for example, $m=0.5$ for diffusion controlled reactions and $m=1$ for first-order chemical reactions. Eq. 3.14 is equivalent to the integral form of the JMAK equation shown in Table 3.1.

3.2.4. Model for laser ignition of nanothermite pellets

Consider an Al/metal oxidizer consolidated nanothermite pellet as shown in Figure 3.6. Once ignited by a laser by heating its top surface, the heat release by the chemical reactions self-sustains the flame. If the pellet is made of consolidated Al particles, the burned zone is made up of porous Al_2O_3; however, for Al/CuO consolidated pellets, the burned zone disintegrates/vaporizes. A combustion model of consolidated Al or Al/CuO pellets is very complex due to the multi-scale and multi-phase physics. If the fuel and oxidizer particles are at the nanoscale, the chemical reactions are much faster than the heat/mass transport through the pellet; hence the local thermodynamic equilibrium is valid. Further assumptions are made to simplify the modeling equations:

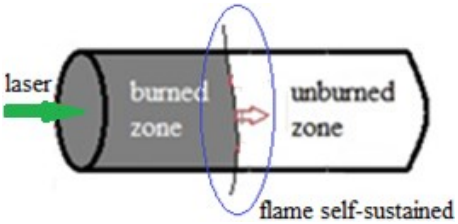

Figure 3.6: Combustion of a laser ignited nanothermite pellet

- The reaction rates are based on Arrhenius kinetics, and the overall mechanism is first order with respect to the extent of reaction
- Particle agglomeration and sintering do not affect the porosity in the unreacted zone, such that the effective thermodynamic properties are only dependent on the overall porosity and temperature
- The local gas velocity is given by Darcy's law for porous media and laminar flow

Based on the assumptions above, the conservation of mass for the gas phase generated by the reaction is given by equation

$$\frac{\partial(\varepsilon \rho_g)}{\partial t} + \nabla \cdot (\rho_g \boldsymbol{v}_g) = \rho_p \frac{\partial \alpha}{\partial t} \quad \text{(Eq.3.15)}$$

where ε is the porosity, ρ_g is the local gas concentration, $\boldsymbol{v_g}$ is the bulk velocity at the macro scale (i.e. volume flowrate over the cross sectional area of the porous element), ρ_p is the pellet bulk density, and α is the extent of reaction. The extent of reaction is 0 at ignition and 1 when reaction is complete locally, and its time derivative is the reaction rate

$$d\alpha/_{dt} = (1-\alpha) A e^{-E_a/RT} \quad \text{(Eq.3.16)}$$

where A is the frequency factor, and E_a is the apparent activation energy. The bulk gas velocity is relative to the stationary solid phase and is found from Darcy's law [133]

$$v_g = \frac{-\kappa}{\varepsilon \mu} \nabla P \quad \text{(Eq.3.17)}$$

where κ is the permeability of the porous media, μ is the dynamic viscosity of the gas, P is the pressure gradient across the reaction zone. The total gas pressure can be estimated from the ideal gas law under the assumption of local thermodynamic equilibrium. The conservation of energy is given by

$$\left(\rho_p c\right)_e \frac{\partial T}{\partial t} + \nabla \cdot \left((\rho c)_g \boldsymbol{v_g} T\right) = \nabla \cdot (k_e \nabla T) + \dot{Q}_{chem} \quad \text{(Eq.3.18)}$$

where ρ_p is the bulk density of the pellet, c_e is the effective specific heat capacity, k_e is effective the thermal conductivity, c_g is the specific heat capacity of the gas, and $\dot{Q}_{chem}$ is the energy release rate per unit volume (W/m^3) based on the Arrhenius equation,

$$\dot{Q}_{chem} = \rho_p H_c \, {d\alpha}/{dt} \quad \text{(Eq.3.19)}$$

where H_c is the heat release or reaction enthalpy. The effective specific heat capacity is a function of the heat capacities of the solid and gas phases as follows

$$c_e = (1-\varepsilon)c_s + \varepsilon c_g \quad \text{(Eq.3.20)}$$

The effective conductivity is also a function of the conductivities of the solid and gas phases (i.e. two phase heterogeneous mixture). The effective thermal conductivity of the porous structure is maximum in the parallel mode and minimum in the series mode as follows [134]

$$k_e|_{max} = (1-\varepsilon)k_s + \varepsilon k_g \quad \text{(Eq.3.21)}$$

$$k_e|_{min} = \left[\frac{(1-\varepsilon)}{k_s} + \frac{\varepsilon}{k_g}\right]^{-1} \quad \text{(Eq.3.22)}$$

The density, specific heat capacity and thermal conductivity of each component are available in the NIST Chemistry Webbook [135]. Prior to ignition, the energy equation can be simplified further since the gas generated from chemical reactions is negligible. In cylindrical coordinates, the energy equation is given by

$$(\rho_p c)_e \frac{\partial T}{\partial t} = \frac{1}{r}\frac{\partial T}{\partial r}\left(kr\frac{\partial T}{\partial r}\right) + \frac{\partial T}{\partial z}\left(k\frac{\partial T}{\partial z}\right) + \rho_p H_c \, {d\alpha}/{dt} \quad \text{(Eq.3.23)}$$

Boundary conditions are given by the following conditions: laser flux with radiation/convection on the laser heated surface, adiabatic on the surface opposite to the laser heated surface, and heat convection on the side surfaces [136] [34]. These heat flux boundary conditions are given by

$$\dot{q}''_{bottom} = 0 \quad \text{(Eq.3.24)}$$

$$\dot{q}"_{side} = -h(T - T_a) \quad \text{(Eq.3.25)}$$

where h is the free convection heat transfer coefficient, and T_a is the ambient temperature,

$$\dot{q}"_{top} = \alpha \frac{P}{\pi {r_o}^2} D - \varepsilon 6(T^4 - T_a^4) - h(T - T_a) \quad \text{(Eq.3.26)}$$

where α is laser absorption coefficient, P is the laser power, r_o is the laser spot size radius, D is a function dependent on the laser beam profile, where $D = 1$ for uniform beam, and $D = e^{-2/{r_o}^2 (x - x_o)^2}$ for Gaussian beam; x is the radial direction along the heated surface from its x_o center; ε is surface emissivity, and σ is the Stefan-Boltzmann constant.

3.2.5. Analysis of the ignition delay, burn duration, and reaction front/flame plume speeds in nanothermite pellets

The laser ignition and high speed imaging setup described in section 3.1.5 provides high speed images, photodiode emission and force data of the burning nanothermite pellet. These data are analyzed using the following procedures:

3.2.5.1. Ignition delay and burn duration

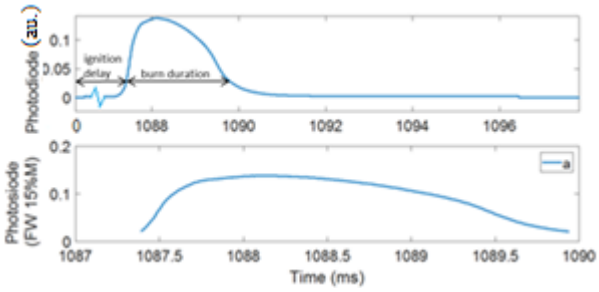

Figure 3.7: Example of a photodiode signal during nanothermite combustion

The ignition delay and burn duration are measured from the photodiode emission data and verified by time frames of the high speed images. Consider the photodiode signal during nanothermite combustion in Figure 3.7a, as measured by an unfiltered photodiode. The ignition delay is measured from the time the laser is triggered (t = 0) until 15% of the amplitude. The burn duration is given by the full width at 15% maximum (FW15%M) as shown in Figure

3.7b. The 15% maximum avoids any signal due to radiation form the laser and surface heating. The normalized time-averaged photodiode signal is computed from

$$\bar{Y}_n = {\int_0^t Y dt}/{(m\Delta t)} \quad \text{(Eq.3.27)}$$

where Y is the raw photodiode signal, Δt is the signal duration, and m is the sample mass. This normalized emission represents the average energy release rate by the nanothermite reaction.

3.2.5.2. Reaction front and flame plume speeds

The reaction front and flame plume speeds are measured from the high speed images. Consider the ignition and combustion of a consolidated nanothermite pellet shown in Figure 3.8. Ignition occurs at time t_o due to laser heating the pellet surface by forming an ignition spot, such that the heat release can sustain the combustion. The reaction front propagates through the unburned mixture, and the gas generated by the combustion expands in a flame plume. The reaction front is distorted due to the local heterogeneous reactions and gas turbulence. In order to estimate the speed of this reaction front, the ignition spot is assigned to position (0,0) at t = 0; then four points are selected on its trajectory, which are fitted with a line of best fit. The high speed images captures a 2D moving reaction front as shown in Figure 3.9. The speeds of the reaction front are calculated from

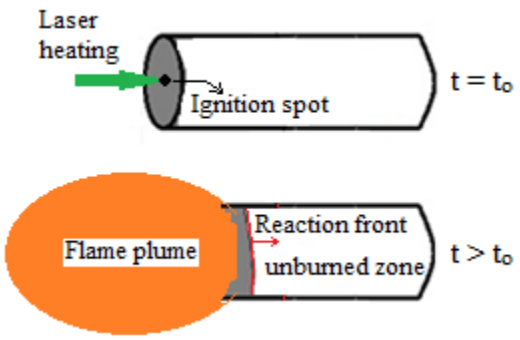

Figure 3.8: Laser ignition and combustion of a nanothermite pellet

$$v = {d_i}/{t_i} \quad \text{(Eq.3.28)}$$

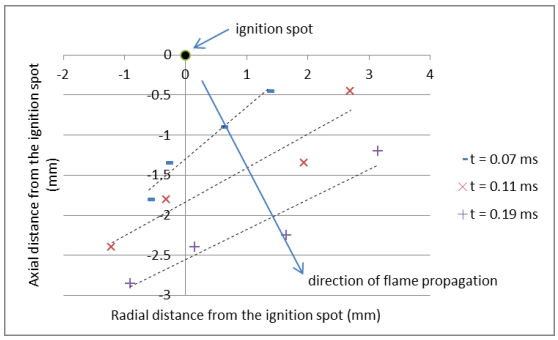

Figure 3.9: 2D representation of a moving reaction front

where d_i is the orthogonal distance and t_i is the time from the ignition spot to the i^{th} frame. The burning speed is determined from the average speeds of the reaction front. Despite the complex 3D morphology of the actual reaction front, its approximate speed in 2D is sufficient for the purpose of this research. The burning speed is a fundamental indicator of the reaction mechanism that self-sustains the combustion.

It is assumed that the flame plume has spherical geometry. The plume area captured by the high speed camera is not well defined due to local radiation/convective heat transfer nears its surface. The plume area is estimated by mearing the area of the saturated pixels. A notch filter is used to lower the radiation intensity that reaches the camera sensor such that the intensity of combustion does not saturate the entire image. Furthermore, it is assumed that the 2D area of the flame plume is equivalent to the area of a circle. Then, the initial velocity and acceleration of the flame plume is calculated by curve fitting the equation for average acceleration of the radius of this circle,

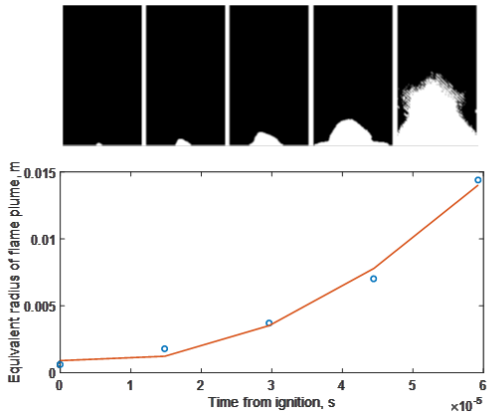

Figure 3.10: 2D accelerating frame plume

$$r = v_o t + {}^1\!/_2\, a t^2 \qquad \text{(Eq.3.29)}$$

where r is the equivalent radius of the flame plume, t is time from ignition, v_o is the initial velocity, and a is the average acceleration. An example of a 2D accelerating flame plume is shown in Figure 3.10.

3.2.6. Batch reactor model

The batch reactor experiments are used to study the reactions between aluminum powders and water under high pressure. These reactions are initiated thermally and self-sustained at high temperatures without reaching the boiling temperature of water due to the high pressure. Consider the batch reactor schematic illustrated in Figure 3.11. Before ignition, at time $t=0$, the condensed phase contains Al powder and water mixture, and the gas phase contains argon at high pressure. After ignition, the overall reaction proceeds as

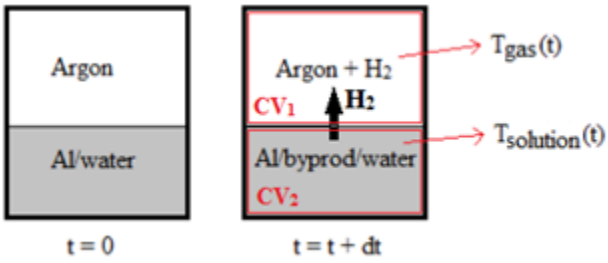

Figure 3.11: Batch reactor for Al/water reactions under high pressure

$$Al_{(s)} + H_2O_{(l)} \rightarrow AlO_xH_{y(s)} + H_{2(g)} \qquad \text{(R3.1)}$$

where the phase of the aluminum-hydroxide by-product is dependent on the thermodynamic stability of reactions R1.3 through R1.5 in section 1.3. The condensed phase contains the unreacted Al, the Al-hydroxide by-product and the unreacted water mixture (shown inside control volume CV2), and the gas phase contains the argon and the hydrogen gas product (shown inside control volume CV1). The temperatures of the condensed and gas phases are measured by thermocouples and the total gas pressure is measured by a pressure transducer, as described in section 3.1.7.

A semi-empirical model of the batch reactor is derived with the following assumptions that simplify the governing equations [137] [138]: 1) the chamber is adiabatic; 2) water evaporation is neglected; 3) the reaction rate is obtained by estimating the rate of hydrogen production; 4) the model is 0D, such that the advection and diffusion of mass and heat are ignored. The mass rates of the condensed and gas phases are given by

$$\dot{m}_{mix} = -n_0 M_{mix} \, {d\alpha}/{dt} \tag{Eq.3.30}$$

$$\dot{m}_g = n_0 M_{H2} \, {d\alpha}/{dt} \tag{Eq.3.31}$$

where n_o is the initial moles of Al, M_{mix} is the equivalent molar mass of the condensed phase, M_{H2} is the molar mass of hydrogen gas, and $d\alpha/dt$ is the reaction rate. The conservation of mass follows $\dot{m}_{mix} + \dot{m}_g = 0$ and the constant reactor volume follows $V_{mix} + V_g = V_{reactor}$.

The conservation of energy is formulated across the entire volume of the reactor (CV1 and CV2 in Figure 3.11) such that

$$\frac{d}{dt}(mcT)_{mix} + \frac{d}{dt}(mc_v T)_g = n_0 H_r \, {d\alpha}/{dt} \tag{Eq.3.32}$$

where c_{mix} is the specific heat capacity of the condensed phase, T_{mix} is the temperature of the condensed phase, c_{vg} is the specific heat at constant volume of the gas, T_g is the temperature of the gas, and H_r is the heat of the reaction. The specific heat capacities of the condensed and gas phases are given by the mass averaged heat capacities of the respective components,

$$c_{mix} = \frac{1}{m_{mix}} \sum_i m_i \, c_i \qquad \text{(Eq.3.33)}$$

$$c_g = \frac{1}{m_g} \sum_j m_j \, c_j \qquad \text{(Eq.3.34)}$$

where subscript *i* includes all components in the condensed phase: aluminum, water and aluminum-hydroxide; and subscripts *j* includes all components in the gas phase: argon and hydrogen. The specific heat capacity of each component is dependent on temperature and available in the NIST Chemistry Webbook [135].

After expansion and some mathematical manipulation, the energy equation reduces to

$$\begin{aligned} \dot{T}_{mix} \left((mc)_{mix} + T_{mix} \sum_i m_i \frac{dc_i}{dT} \right) + T_{mix} \left(\sum_i c_i \dot{m}_i + c_{mix} \dot{m}_{mix} \right) \\ + \dot{T}_g \left((mc_v)_g + T_g \sum_j m_j \frac{dc_j}{dT} \right) + T_g \left(\sum_j c_j \dot{m}_j + c_{vg} \dot{m}_g \right) \\ = n_0 H_r \, {}^{d\alpha}/_{dt} \end{aligned} \qquad \text{(Eq.3.35)}$$

Lastly, the ideal gas law is the equation of state for this batch reactor model. The extent of reaction is given by the ideal gas law for hydrogen,

$$\alpha = \frac{n_{H2}}{n_{H2t}} = \frac{\left({P_t V_g}/{R_u T_g} - n_{Ar} \right)}{n_{H2t}} \quad \text{(Eq.3.36)}$$

where n_{H2} are the moles of hydrogen gas produced, n_{H2t} are the theoretical moles of hydrogen gas produced if the entire mass of Al is reacted, P_t is the total gas pressure, V_g is the volume of the gas phase, R_u is the universal gas constant, and n_{Ar} are the constant moles of argon gas injected into the chamber. The pressure curve $P_t(t)$ obtained from the experiments is used to estimate the extent of reaction α.

4. Controlled oxidation and combustion of micro/nano Al particles in air

This chapter summarizes specific research on the controlled oxidation of micro and nano Al powders in air using thermogravimetric analysis with differential scanning calorimetry, and the combustion of laser ignited consolidated pellets made of Al nanoparticles. The research gap and objectives are outlined first, and followed by the experimental and theoretical results.

4.1. Role of Phase Transformations in Micro and Nano Aluminum Powders on Kinetics of Oxidation using Thermogravimetric Analysis

These results were published in reference [139]. The copyright permission was obtained from the journal. F. Saceleanu conducted the experiments, analyzed the experimental data, and wrote the manuscript; S. Atashin assisted with the experimental setup; J. Wen revised the manuscript and suggested changes for improving the quality.

4.1.1. Overview

Aluminum micro and nanoparticles are key ingredients in the synthesis of nano energetic materials. Hence it is important to characterize the kinetics and the rate controlling processes of oxidation. Literature shows that mass diffusion processes and phase transformations in the aluminum oxide are important. However, the physical processes regarding simultaneous oxidation and phase transformation are unclear. In this paper, controlled thermogravimetric oxidations of 40-60 nm and 1 μm Al powders are performed under constant heating rate and isothermal conditions, with variable pressure of air in argon. It is found that the core-shell model of homogenous oxidation is applicable when the shell does not undergo phase transformations, and the apparent activation energy values agree with the literature data. On the other hand, the simultaneous oxidation and phase transformation is shown to fit better to the JMAK model and its parameter defines the rate controlling processes. Diffusional processes are rate determining

steps in the oxidation of Al micro and nanopowders while the kinetics of the chemical reactions are very fast. Unlike the micron powders, the particle size distribution has a major effect on the shape of the oxidation curves of the nanopowders.

4.1.2. Objectives

The kinetics of oxidation of Al micro and nanoparticles are challenging to study due to the multi-scale nature of the problem. It is generally assumed that the particle maintains its spherical morphology and oxidation is homogenous. However, the diffusional paths in the alumina shell and the chemical reaction rates can vary if the alumina shell does not maintain its phase. The main objectives of this paper are to address the validity of the core-shell model at different oxidation stages using TGA/DSC under constant heating rate, and analyze the effects of phase transformations in the alumina shell on the kinetics of oxidation. The mechanisms of oxidation and respective apparent activation energies based on the core-shell model are validated with similar models in literature. However, isothermal oxidations at temperatures within the range of phase transformations indicate that oxidations are described by the JMAK model with a parameter that defines the rate controlling processes. It is shown that the phase transformations within the alumina shell control the kinetics of oxidation and the corresponding mass diffusivities.

4.1.3. Experimental

Aluminum powders with APS (Aerodynamic Particle Size) diameters of 40-60 nm and 1 μm were purchased from Skyspring Nanomaterials Inc. The powders were ultrasonicated in ethanol for 30 minutes to lower the degree of agglomeration. The alcohol was then evaporated at room temperature overnight. The powders were further pre-heated in the oven at 200 °C for 30 minutes to remove adsorbed moisture. Two types of experiments were conducted:

(1) Oxidation under 2 different flowrates of air in Argon, and constant total flowrate in the chamber. Assuming homogenous mixing, the partial pressure of air is approximately 10 mbar and 250 mbar, respectively. Temperature conditions were as follows:

a) Constant heating rate: 10, 20 and 30 °C/min, from 30 to 1200 °C

b) Isothermal: 550, 570, 590, 620, 700, 800 and 900 °C, for 30 min

(2) Phase transformation in an Argon only environment under constant heating rate of 10, 20 and 30 °C/min. For these experiments, a procedure described in [43] was used. The Al powder was first heated to near its melting point, then cooled to room temperature, and finally reheated past its melting point. Any phase transformation is expected to occur in the first heating stage. Hence the exothermic heat release is found by subtracting the DSC curves of the two heating stages.

4.1.4. Results and discussion

4.1.4.1. Stage of oxidation of the Al Powders

Figure 4.1 shows the TGA/DSC results of the 1 μm Al powder under a heating rate of 10 °C/min and partial air pressure of 10 mbar. Most of the oxidation occurs after the melting temperature of the aluminum core. This behavior is consistent with the oxidation of 3 to 5 μm Al particles [19]. The top DSC curve indicates that phase transformations occur in the alumina layer ahead of aluminum melting. The area under the exothermic peak is very small since the relative mass of the alumina is low (calculations show that the 1 μm Al powder has an active content of approximately 85%). The oxidation of the 1 μm Al powder can be split into 3 stages: stage 1 is the low temperature oxidation, which is the growth of the native alumina shell; stage 2 is defined by simultaneous oxidation and phase transformations; and stage 3 is the growth of the oxide after the melting of the aluminum core.

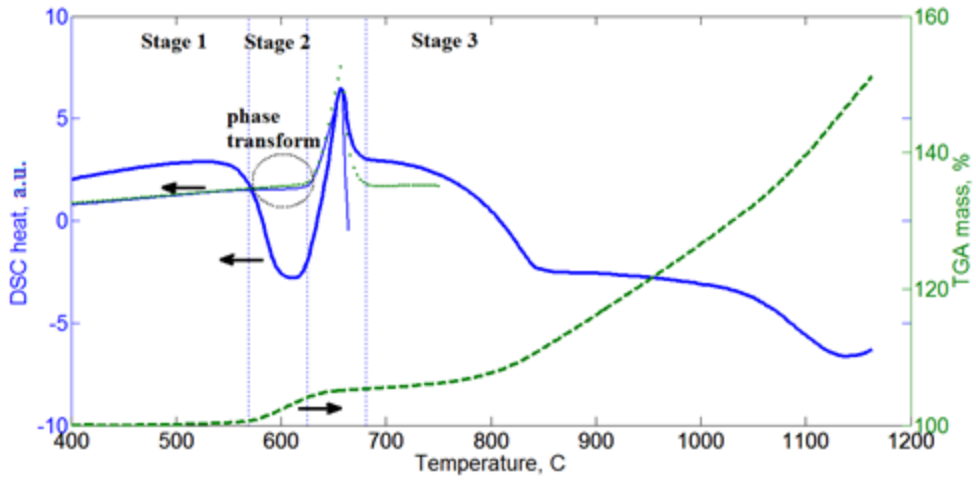

Figure 4.1: Oxidation stages of the 1 micron Al powder (heating rate 10 C/min, air pressure 10 mbar); NOTE: heat release due to phase transformation superimposed

The TGA/DSC results of the 40-60 nm Al powder oxidized under a heating rate of 10 °C/min and partial air pressure of 10 mbar are shown in Figure 4.2. Two TGA regimes are evident, which are separated by the melting peak of aluminum. It is important to note that Al nanoparticles below a certain size are expected to oxidize completely before melting. The complete oxidation of nanoparticles based on different size bins (10 to ~850 nm) was predicted in [51]. The authors' results indicate that particles less than 100 nm oxidize fully before melting. Based on the TGA data in Figure 4.2 and assuming that the 40-60 nm powder is monodisperse (particle diameter of 50 nm), the oxide thickness is estimated to increase to 8.5 nm by the end of stage 2. This value is in good agreement with the oxide growth predicted in fully oxidized monodispersed nanoparticles [51], which indicates that any oxidation past the melting of Al is caused by larger particles in the nano powder. Similarly to the micron powder, the oxidation of 40-60 nm Al powder is composed of a low temperature oxide growth in stage 1, followed by simultaneous oxidation and phase transformations in stage 2. Stage 3 will be ignored since it does not represent the kinetics of oxidation of the 40-60 nm particles.

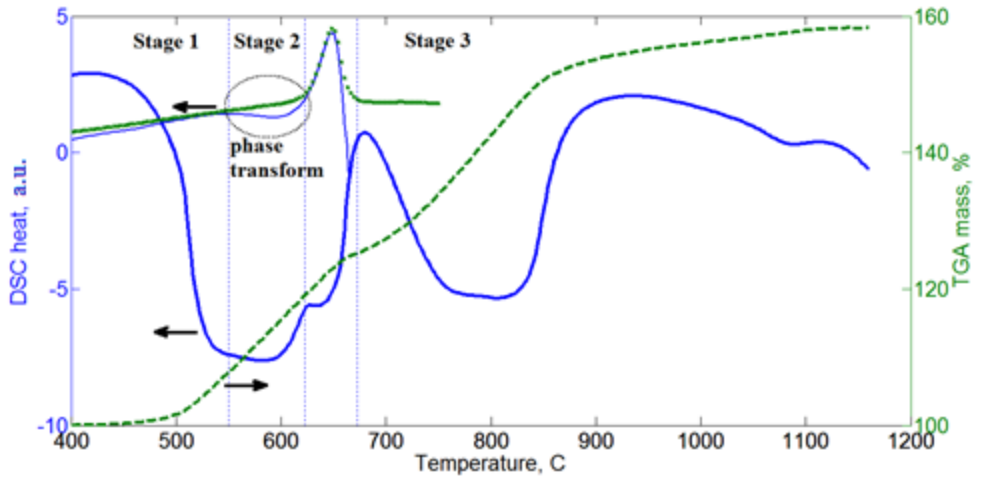

Figure 4.2: Oxidation stages of the 40-60 nm Al powder (heating rate 10 C/min, air pressure 10 mbar); NOTE: heat release due to phase transformation superimposed

At the nanoscale, particle size plays a critical role on the oxidation behavior. Experimental data shows a significant decrease in the active content of aluminum (from 90% for 100 nm particles to 30% for 20 nm particles [6]), since the relative mass of the native Al_2O_3 increases. Furthermore the thermochemical properties of nanoparticles approach those of a single atom since the number of surface atoms relative to the bulk increases significantly. Simulations based on the core-shell model show that the shape of the predicted TGA curve is highly sensitive to the particle size distribution [26]. In order to characterize the 40-60 nm Al powder, the particle size distribution was obtained by measuring the diameter of 250 particles using SEM images at two magnifications. Figure 4.3 indicates that the most probable particle diameter is within 40 to 60 nm; however, larger particles with diameters between 80 and 160 nm also have a significant contribution and their oxidation is expected to continue at higher temperatures (i.e. oxidation in stage 3 as illustrated in Figure 4.2).

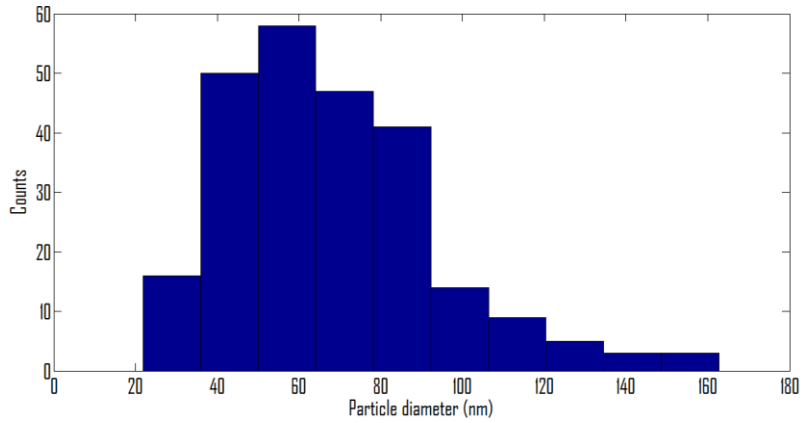

Figure 4.3: Particle size distribution of the 40-60 nm Al powder measured via SEM image analysis

It should be noted the TGA/DSC curves for the micro and nano Al powders shift to higher temperatures with increasing the heating rate since oxidations are thermally activated processes. Also, it was observed that under a constant heating rate, the TGA/DSC curve shits to lower temperatures with increasing the air pressure. This indicates that the rate of oxygen diffusion through the shell increases with the air pressure.

4.1.4.2. Characterization of the Al powders

SEM images of the 1 μm Al powder as-prepared and after oxidation to 600 °C and 1000 °C, are shown in Figure 4.4. The as-prepared micro powder is composed of distinguishable and spherical Al particles, with diameters centered around 1 μm as seen in Figure 4.4a. Oxidation to 600 °C does not change the morphology of the particles (see Figure 4.4b). However, oxidation at temperatures above the melting point of the aluminum core has a significant effect on the particle's surface. Rough, needle-like structures observed in Figure 4.4c are caused by molten aluminum that diffused through the alumina shell and oxidized non-homogenously on the outer surface. This is caused by the 6% volume increase of aluminum after melting [55], which creates tensile stresses in the core. The pressure gradients along with the enhanced diffusivity create a

flux of Al atoms toward the outer surface of the particle. The diffusion of aluminum is an important mechanism at high temperatures, which was also mentioned in [20]. Consequently, some particles sinter as highlighted in Figure 4.4c.

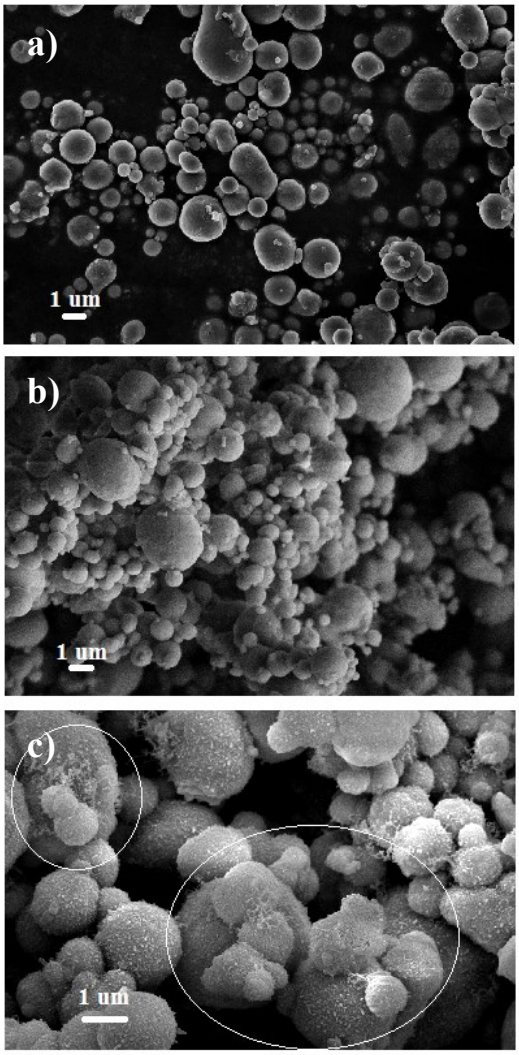

Figure 4.4: SEM images of 1 micron Al powder
a) as-prepared; oxidized to b) 600 C and c) 1000 C

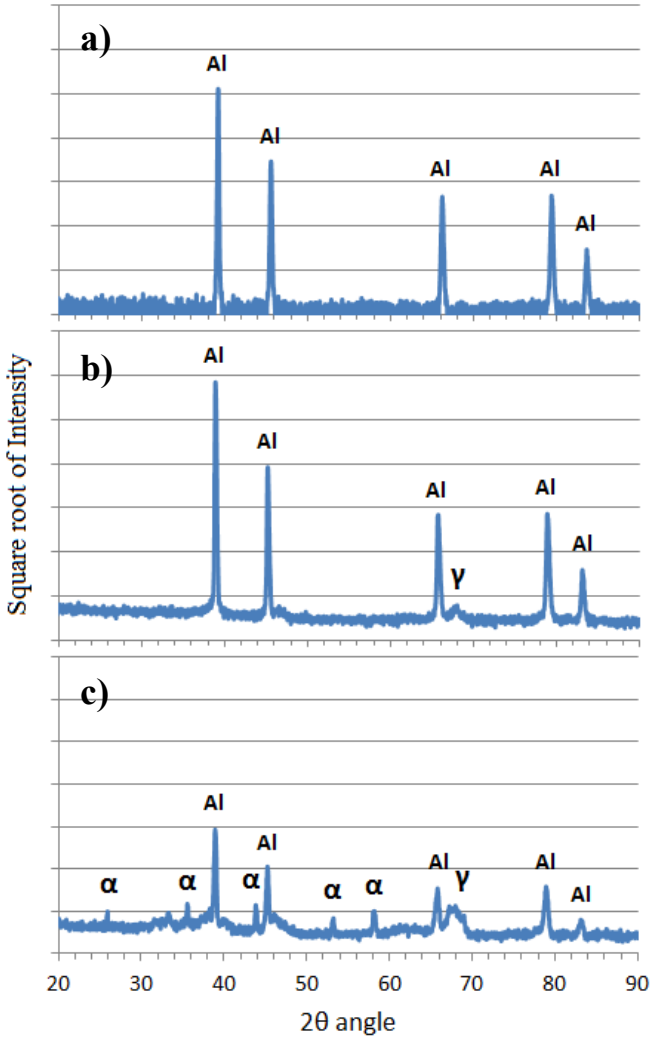

Figure 4.5: XRD results of 1 micron Al powder
a) as-prepared; oxidized to b) 600 C and c) 1000 C

XRD peaks of the 1 µm Al powder as-received and after oxidation to 600 °C and 1000 °C are shown in Figure 4.5. The Al and Al_2O_3 polymorphs were matched with the reference peaks in

[140] and [141] verified with the results in [51]. Figure 4.5a indicates that the native alumina shell is mostly amorphous. Partially crystallinity may exist, but the XRD signal is not detectable since the degree of oxidation is low. Figure 4.5b indicates a single peak of aluminum oxide (γ-Al_2O_3) at 600 °C, and Figure 4.5c indicates that most of the shell is α-Al_2O_3 at 1000 °C. These transitions in the alumina shell follow a series of phase changes (amorphous-γ-α) as predicted for the oxidation of 3 to 5 μm Al particles [19].

SEM images of the 40-60 nm Al powder as-prepared and after oxidation to 600 °C and 1000 °C, are shown in Figure 4.6. The as-prepared nanoparticles are spherical and indicate some degree of agglomeration. After oxidation to 600 °C, larger agglomerates are apparent as highlighted in Figure 4.6b. Molecular dynamics simulations indicate that nanoparticles can sinter at temperatures as low as 300 °K [142] due to the higher specific surface energy in comparison to micron particles. Figure 4.6c illustrates two different morphologies after oxidation to 1000 °C. No significant agglomeration is evident in the smaller nanoparticles, which indicates that these particles oxidized completely at lower temperature. These nano oxide particles melt at much higher temperature since bulk alumina melts around 2000 °C. However, the larger nanoparticles form sintered structures as highlighted in Figure 4.6c. This can be explained by molten aluminum that diffused outside the particles similar to 1 μm particles (refer to Figure 4.4c).

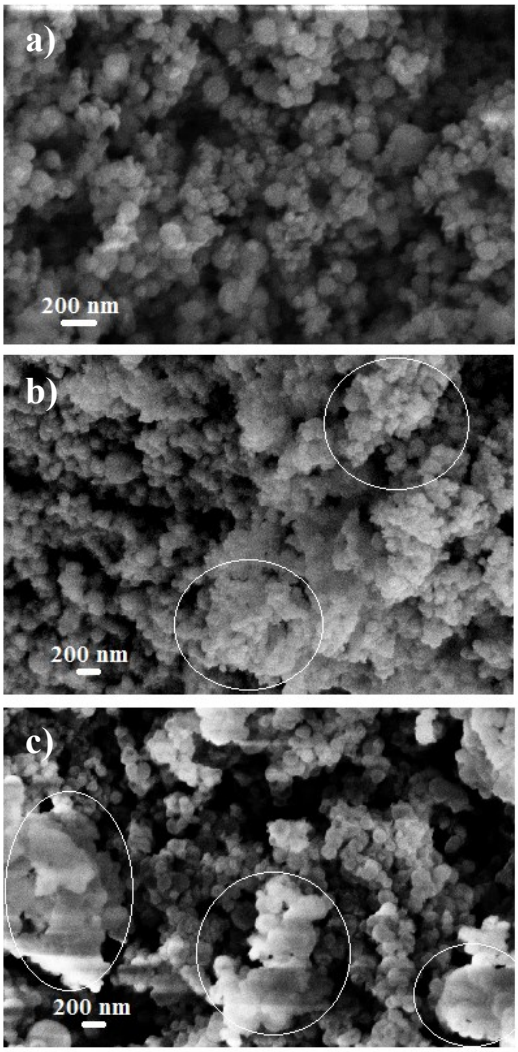

Figure 4.6: SEM images of 40-60 nm Al powder
a) as-prepared; oxidized to b) 600 C and c) 1000 C

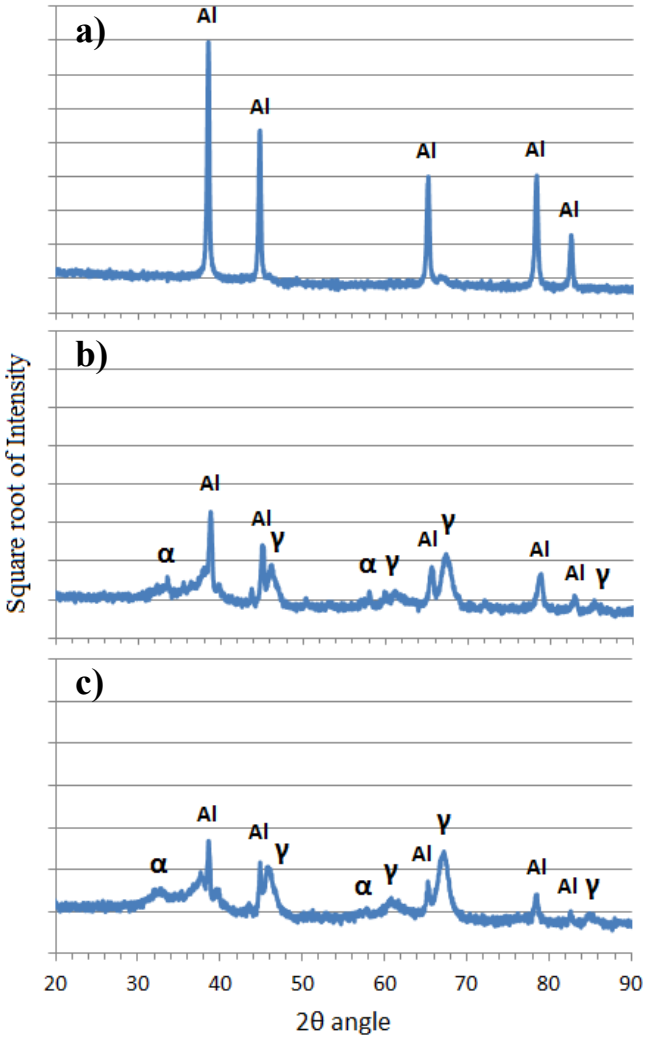

Figure 4.7: XRD results of 40-60 nm Al powder
a) as-prepared; oxidized to b) 600 C and c) 1000 C

XRD peaks of the 40-60 nm Al powder as-received and after oxidation to 600 °C and 1000 °C are shown in Figure 4.7. The Al and Al_2O_3 polymorphs were verified with the XRD data in [140] and [141]. Similarly to the 1 μm Al particles, the native alumina shell in the 40-60 nm particles is mostly amorphous. However, Figure 4.7b indicates significant amount of two polymorphs of Al_2O_3, γ and α, after oxidation to 600 °C, along with reduced intensity of aluminum. This is expected since the 40-60 nm particle are expected to oxidize completely before melting. Figure

4.7c indicates that a significant amount of aluminum remains after oxidation to 1000 °C, which is attributed to the larger nanoparticles in the powder.

4.1.4.3. Theoretical analysis

4.1.4.3.1. Controlling mechanism of oxidation

As illustrated in Figure 1.2, the alumina shell must be removed in order to study the chemical kinetics only. However, the Al particle always forms a protective alumina layer to prevent its core from oxidation. In order to estimate the kinetics of the $Al+O_2$ reaction, the Al powders were heated to temperature above melting of aluminum in an Argon only environment, and then oxygen was introduced. As shown previously in Figure 4.4c, molten aluminum diffuses outside the particle after melting. The reaction between molten Al and air was conducted in TGA/DSC experiments at 700, 800 and 900 °C. It was found that the reaction timescale at 700 °C was an order of magnitude smaller than at temperatures below melting (e.g. at 620 °C) under the same conditions. This indicates that the reaction kinetics is very fast. The apparent activation energy for the kinetically controlled oxidation was found to be 34 ± 8 kJ/mol and 37 ± 2 kJ/mol in 10 mbar and 250 mbar air, respectively. These values are significantly lower than the literature data for the diffusion controlled activation energy of oxidation in micro and nano Al powders [43] [49]. The reaction rate constant, k_s, was found to be on the order of 10^6 m/s; assuming a diffusivity of the Al cations through the shell of 10^{-20} m^2/s [43], calculations show that the resistance due to mass diffusion through the alumina shell is several orders of magnitude higher than the resistance due to chemical kinetics. It is determined that mass diffusion of oxygen and aluminum through the shell is the rate determining mechanism of oxidation at high temperatures.

However, the controlling mechanism in low-temperature oxidation is not fully understood. It has been suggested that low-temperature oxidation is driven by the diffusion of Al cations [43] [49], and initiated by the chemical reactions on the particle surface [52].

4.1.4.3.2. Kinetics of phase transformation in Al2O3 shell

Figure 4.8 shows the apparent activation energy for phase transformation using JMAK model (Eq. 3.14) and Kissinger's equation (Eq. 3.5). According to JMAK model, the growth of the new phase occurs randomly within the bulk and surface. Hence it is assumed that crystallization in the 40-60 nm and 1 μm Al powders have similar dimensions because the DSC has similar shape and occurs within the same temperature range.

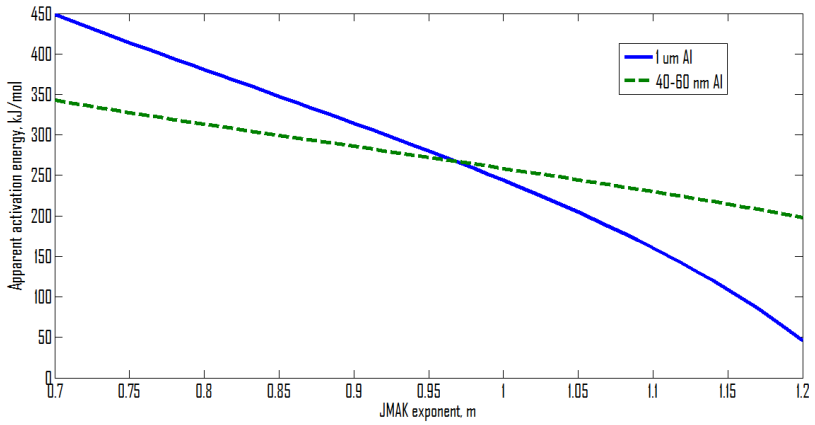

Figure 4.8: Apparent activation energy of the phase transformation using Kissinger method and JMAK model

Based on Figure 4.8, the phase transformation in the aluminum powders is characterized by E_a = 270 kJ/mol and m = 1. This apparent activation energy compares well with 250 kJ/mol found in [43]. Furthermore, m =1 indicates that the phase transformation is driven by surface crystallization.

4.1.4.3.3. Kinetics of oxidation: 1 µm Al powder

The kinetics of oxidation under constant heating rate (e.g. as shown in Figure 4.1) were analyzed using the derivative model (Eq. 3.12) and the integral model (Eq. 3.13a and 3.13b). Figure 4.9 shows an example of the processed TGA curve under constant heating rate of 10 °C/min and partial air pressure of 10 mbar. The apparent activation energy for O_2 or Al diffusion through the alumina shell is given by the slope of the fitted lines. The fitted E_a values of the 2 models are comparable in Stages 1 and 3, where the alumina shell is mostly in a single phase. This validates the applicability of the core-shell reaction model. Apparent activation energy for diffusion in stage 1 is approximately 160 ± 23 and 166 ± 19 kJ/mol in air pressure of 10 mbar and 250 mbar, respectively. The E_a values increase to 190 ± 34 and 180 ± 26 kJ/mol in stage 3, since mass diffusivity is higher in crystalline shell compared to amorphous. These values are the average of the 3 heating rates and are comparable to the values reported in [49] for 3-5 µm Al particles. However, a single E_a value is not representative of the oxidation kinetics in stage 2 since the phase transformations in the shell changes the effective diffusivity (i.e. no line of best fit in Figure 4.9).

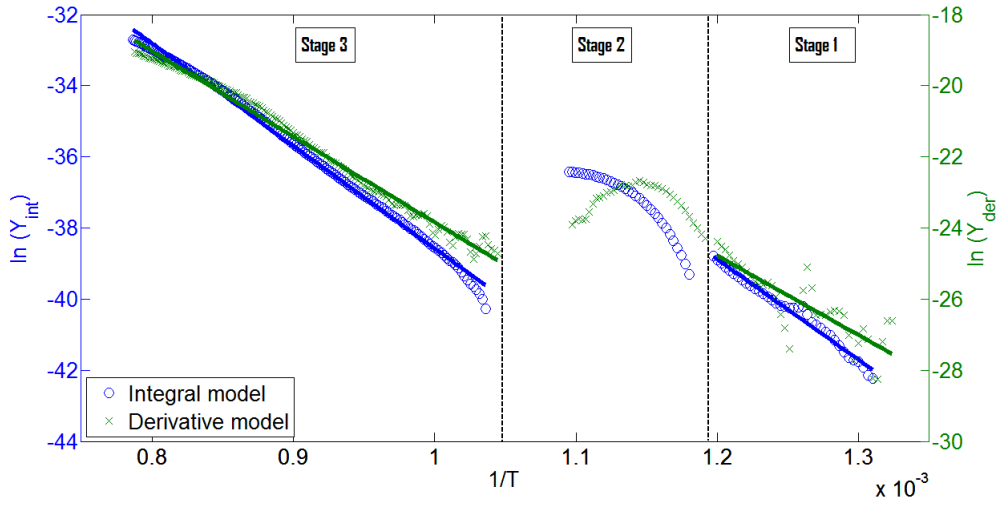

Figure 4.9: Processed TGA data for the oxidation of 1 micron Al powder (heating rate 10 C/min, air pressure 10 mbar)

Isothermal TGA experiments at temperatures within stage 2 were conducted to understand the kinetics of simultaneous oxidation and phase transformation. Figure 4.10a illustrates the TGA mass versus time for oxidation in 10 mbar air. It should be noted that the mass change is maximized at the lowest temperature (550 °C) and minimized at the highest temperature (620 °C), which seems to be counter-intuitive. More of the alumina underwent the phase transformation at higher temperature, thus the effective mass diffusivity was reduced. The core-shell model was applied using Eq. 3.13a and results are shown in Figure 4.10b. Mass diffusivity is given by the slope of the graph. It can be seen that diffusivity changes as temperature increases from 550 °C to 620 °C. At 550 °C, the slope of the graph in Figure 4.10b is relatively constant since the effects of phase transformations are less significant.

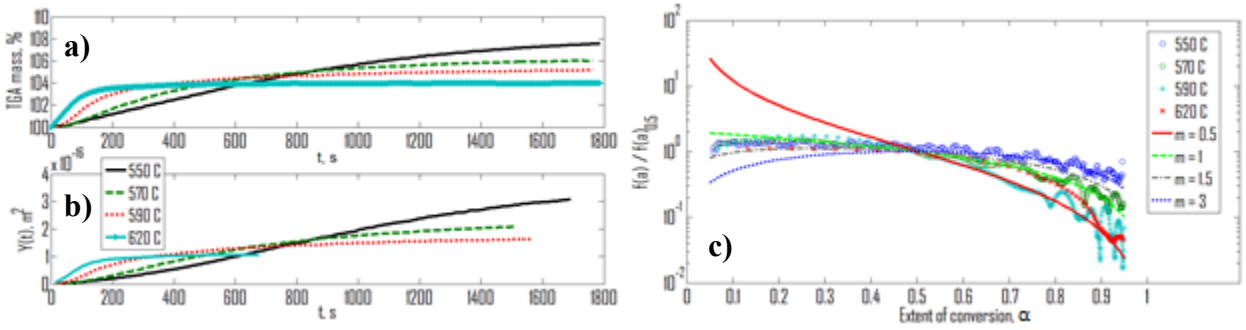

Figure 4.10: Isothermal oxidation of 1 micron Al powder a) raw TGA, b) processed TGA, c) master plot

Master plots analysis was conducted using the equality shown in Eq. 3.6. Literature shows various reaction models, *f(α)*, for solid-gas reactions such as power law, n^{th} order, surface controlled, bi- and tri-dimensional diffusion [50]. It was found that the JMAK model, as given by Eq. 3.14, has the best fit to the TGA data at the isothermal temperatures within stage 2. This indicates that the phase transformations within the alumina shell have a major contribution on the kinetics of oxidation. The JMAK model was also found to characterize the oxidation kinetics of

Cu nanowires [143] and Al nanoparticles [144]. An example of a master plot is shown in Figure 4.10c, at the temperatures of 550, 570, 590 and 620 °C. It is shown that the parameter *m* in the JMAK model of oxidation varies with the extent of reaction, from approximately 1.5 to 0.5. This indicates that as the phase transformation completes, the oxidation process is controlled by an effective mass diffusion through the newly formed crystalline shell. It has been previously explained that the value of *m* indicates the type of rate-determining mechanism at that temperature [132] (e.g. $m = 0.5$ for diffusion controlled reactions, and $m = 1$ for first order reactions).

The effective mass diffusion coefficients within the alumina shell and the parameters *m* vary with the extent of reaction as shown in Figure 4.11 (air pressure is 10 mbar). The effective diffusivity increases at higher temperature for most of the reaction (from $2 \cdot 10^{-19}$ m^2/s at 570 °C to $6 \cdot 10^{-19}$ m^2/s at 620 °C). These values decrease to approximately $5 \cdot 10^{-20}$ m^2/s and *m* approaches 0.5 toward the end of the reaction, which is characteristic of the diffusion resistance within the new alumina phase. Similar trend was observed for the isothermal oxidations in 250 mbar. However, effective diffusion coefficients were on average 1.5 times larger at the higher pressure. This suggests that phase transformations in the shell reduce the resistance to oxidation, such that a higher concentration gradient of air across the shell enhances the kinetics of oxidation.

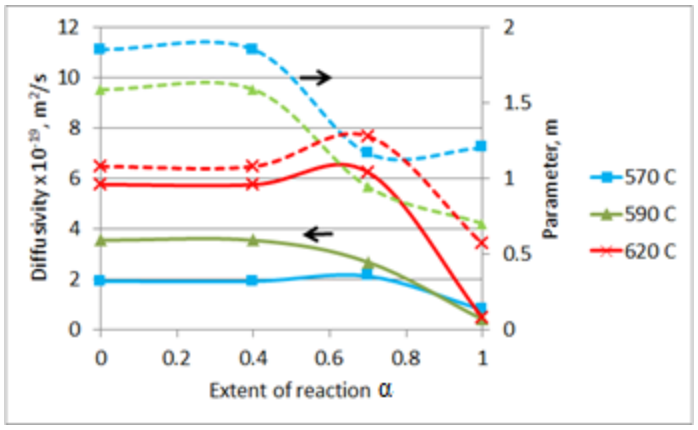

Figure 4.11: Variation in diffusivity and parameter 'm' for 1 micron Al powder within the stage 2 of oxidation

Table 4.1 summarizes the main results for the kinetics of oxidation of 1 μm Al powder. Values reported are the average of the 3 heating rates, and are believed to approximate the kinetics of oxidation under low heating rate. It is concluded that the apparent activation energy is higher in stage 3 compared to stage 1 since mass diffusivity is higher in a crystalline shell than an amorphous shell. Higher air pressure does not have a significant effect on the apparent activation energy for diffusion when the oxide shell is mostly in one phase. Oxidation kinetics in stage 2 can be explained by the JMAK model; however, apparent activation energy is not constant due to the phase transformations in the shell.

Table 4.1: Summary of the oxidation stages of 1 micron Al powder

	Stage 1		*Stage 2*		*Stage 3*	
Air pressure, mbar	*10*	*250*	*10*	*250*	*10*	*250*
E_a (shell diffusion), kJ/mol	160±23	166±19	n/a*		190±34	180±26
E_a (shell diffusion) [49], *kJ/mol*	120±26				228±7	
f(α) model	core-shell		JMAK		core-shell	

*** Shell is not homogenous due to the phase transformations**
Data for 3-5 μm Al particles [49]

4.1.4.3.4. Kinetics of oxidation: 40-60 nm Al powder

The same analysis described in section 4.1.4.3.3 was applied to describe the kinetics of oxidation of the 40-60 nm Al powder. Figure 4.12 illustrates the processed TGA data for oxidation under

10 °C/min and air pressure of 10 mbar. There are greater discrepancies between the activation energy for diffusion controlled oxidation calculated via the derivative and the integral models, which is caused by the size distribution in the 40-60 nm Al powder. As mentioned in section 4.1.4.1, oxidation in stage 3 is caused by nanoparticles larger than 40-60 nm; although shown here in Figure 4.12, this stage is not analyzed further.

The apparent activation energy for diffusion in stage 1 is approximately 159 ± 30 and 162 ± 35 kJ/mol in air pressure of 10 mbar and 250 mbar, respectively. These values are comparable to the activation energies of the 1 μm Al powder in stage 1, which indicates that the particle size is not an important factor at low temperatures. Similar values of E_a were reported for Al nanoparticles with a distribution centered near 70 nm [43]. For comparison, the activation energy for oxygen diffusion in amorphous alumina is 106 kJ/mol [43]. Higher E_a computed in stage 1 may be caused by partial particle agglomeration and partial crystallization of the shell. Similarly to the micron particles, the apparent activation energy for oxidation of 40-60 nm Al in stage 2 is not constant. However, these nanoparticles oxidize completely by the end of stage 2.

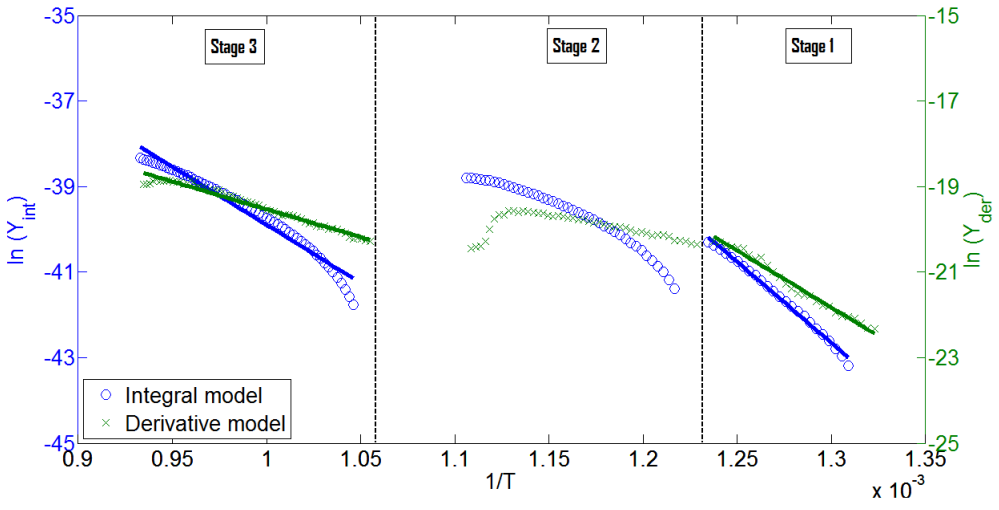

Figure 4.12: Processed TGA data for the oxidation of 40-60 nm Al powder (heating rate 10 C/min, air pressure 10 mbar)

Some results of the isothermal oxidation of the 40-60 nm Al powder within stage 2 are shown in Figure 4.13a for an air pressure of 10 mbar. It can be seen that even at the lower temperature of 550 °C in Figure 4.13b, the effective diffusivity in the shell is more non-linear compared to the micron particles. This indicates that phase transformations occur at lower temperatures in the nanoparticles. Similarly to the micron particles, the JMAK model describes the kinetics of oxidation of nanoparticles in stage 2. An example of a master plot is shown in Figure 4.13c, at the temperatures of 550, 570, 590 and 620 °C. The parameter *m* in the JMAK model of oxidation of nanoparticles also varies with the extent of reaction, from approximately 1.5 to 0.5. However, the value of *m* changes only toward the end of the stage (last 20% of the reaction). This suggests that although the phase transformation plays a role in the complete oxidation of 40-60 nm Al a particle, the shell is not necessarily fully crystallized before complete oxidation.

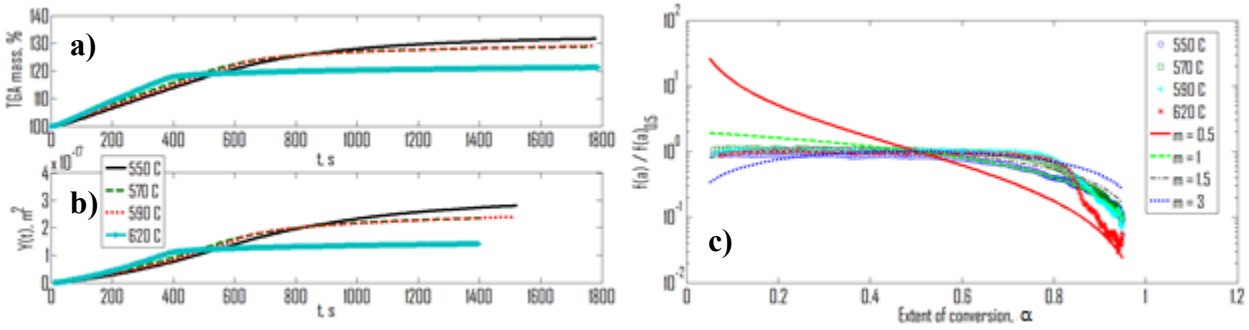

Figure 4.13: Isothermal oxidation of 40-60 nm Al powder a) raw TGA, b) processed TGA, c) master plot

The effective mass diffusion coefficients within the alumina shell and the parameters *m* vary with the extent of reaction as shown in Figure 4.14 (air pressure is 10 mbar). Similarly to the micron particles, effective diffusivity in the nanoparticle shell increases at higher temperature for most of the reaction (from $2 \cdot 10^{-20}$ m^2/s at 570 °C to $5 \cdot 10^{-20}$ m^2/s at 620 °C). The *m* values are greater than 1 for most of the reaction, which is explained by insufficient oxide layer thickness

and phase transformations which reduce the diffusion resistance. At 620 °C, effective diffusivity decrease to approximately $1.5 \cdot 10^{-20}$ m^2/s and *m* approaches 0.5 toward the end of the reaction, which indicates a diffusion controlled mechanism. It should be noted that the effective diffusivity values within the alumina shell computed for the 40-60 nm particles are an order of magnitude lower than those for the 1 µm particles. This can be explained by a lower number of grain boundaries during the crystallization of the nanoparticle shell, which translates to lower effective mass diffusion of oxygen or aluminum through the shell. Similar trend was observed for the isothermal oxidations in 250 mbar; the effective diffusion coefficients were on average 1.1 times larger at the higher pressure. The effect of ambient air pressure on the mass diffusivity in the shell is less pronounced in nanoparticles compared to micron particles.

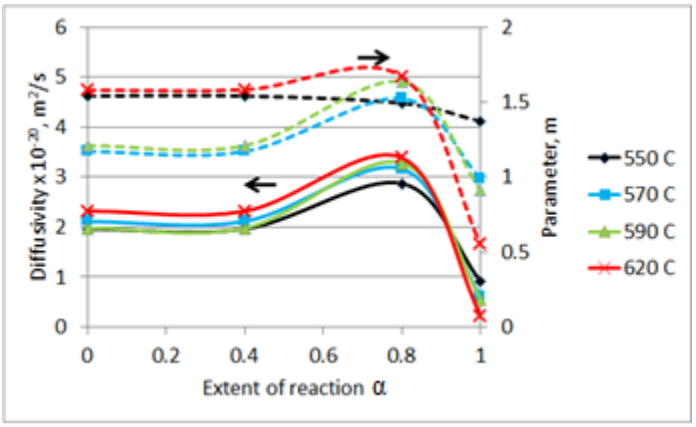

Figure 4.14: Variation in diffusivity and parameter 'm' for 40-60 nm Al powder within the stage 2 of oxidation

Table 4.2 summarized the results for the oxidation of 40-60 nm Al powder. The values reported are the average of the 3 heating rates, and are believed to approximate the kinetics of oxidation under low heating rate. Apparent activation energies for oxidation in stage 1 are comparable to those of the 1 µm Al powder. The oxidation kinetics in stage 2 is explained by the JMAK model.

Table 4.2: Summary of the oxidation stages of 40-60 nm Al powder

	Stage 1		*Stage 2*		*Stage 3*
Air pressure, mbar	*10*	*250*	*10*	*250*	n/a **
E_a *(shell diffusion), kJ/mol*	159±30	162±35	n/a*		
E_a *(shell diffusion)* [43]*, kJ/mol*	110-150				
f(α) model	core-shell		JMAK		

*** Shell is not homogenous due to the phase transformations**
**** Oxidation of nanoparticles larger than 40-60 nm**
Data for Al particles centered around 70 nm [43]

4.1.5. Summary

Experimental TGA/DSC results of the 1 μm and 40-60 nm Al powders indicate that most of the oxidation of the micron particles is above the melting temperature of aluminum, whereas the nanoparticles oxidize completely before melting. At low temperatures (approximately 400 to 550 °C), the apparent activation energy of oxidation is around 160 kJ/mol and independent of the constituent particle size. An intermediate stage before the melting of aluminum is characterized by simultaneous oxidation and phase transformation processes. Diffusional paths in the alumina shell are changing the resistance to oxidation. This stage is explained by the JMAK model; the parameter *m* varies from 1.5 to 0.5, which suggests the oxidation processes are controlled by fast transport of mass and heat prior to full crystallization of the shell. The effective mass diffusivities are on the order of 10^{-19} m^2/s and 10^{-20} m^2/s in the micro and nano powders, respectively. Above the melting temperature of aluminum, the oxidation kinetics of the micron powders has the apparent activation energy around 190 kJ/mol. However, in the nanopowder, particles larger than 40-60 nm are responsible for the oxidation above the melting temperature. The kinetics of the chemical reaction are very fast with an apparent activation energy of around 35 kJ/mol. SEM images illustrate that sintering occurs at temperature above the melting due to molten aluminum diffusing outside the particle.

4.2. Laser Assisted Ignition and Combustion Characteristics of Consolidated Aluminium Nanoparticles

These results were published in reference [35]. The copyright permission was obtained from the journal. F. Saceleanu analyzed the experimental data and wrote the manuscript; J. Wen conducted the experiments and revised the manuscript; M. Idir set up the experimental apparatus; N. Chaumeix revised the manuscript.

4.2.1. Overview

Aluminium (Al) nanoparticles have drawn much attention due to their high energy density and tunable ignition properties. In comparison with their micron scale counterpart, Al nanoparticles possess large specific surface area and low apparent activation energy of combustion, which reduce ignition delay significantly. In this paper, ignition and subsequently burning of consolidated Al nanoparticle pellets are performed via a CO_2 continuous laser in a closed spherical chamber filled with oxygen. Pellets are fabricated using two types of nanoparticle sizes of 40-60 nm and 60-80 nm, respectively. A photodiode is used to measure the ignition delay, while a digital camera captures the location of the flame front. It is found that ignition delay reduces with increasing the oxygen pressure or using the higher laser power. Analysis of the flame propagation rate suggests that oxygen diffusion is an important mechanism during burning of these porous nanoparticle pellets. The combustion characteristics of the Al pellets are compared to a simplified model of the diffusion controlled oxidation mechanism. While experimental measurements of pellets of 40-60 nm Al particles agree with the computed diffusion limiting mechanism, a shifted behavior is observed from the pellets of 60-80 nm Al particles, largely due to the inhomogeneity of their porous structures.

4.2.2. Objectives

The core-shell combustion model of single particles, which is extensively used in literature, computes the burning rate of one nanoparticle from the effective flux of oxidizer reaching the solid surface. This model can be extended to the pellet scale by computing the effective flux of O_2 reaching the reaction interface around pores. These factors have not yet been sufficiently addressed in the literature. The size dependent mechanisms of ignition and burning of Al nanoparticles are still not well understood and usually heavily depends on the type of experiments. Most results came from TG analyses with moderate heating rates. This paper investigates the effects of the laser power, O_2 pressure and Al nanoparticle size on the ignition delay, flame kernel growth rate and burn time of Al pellets. One of our major objectives is to examine the validity of the oxygen diffusion controlled reaction model in elucidating experimental measurements from laser ignited combustion of Al nanoparticle pellets. Since the combustion model is based on the effective mass transport of O_2, its diffusion is dependent on the nanoparticle size and pellet porosity. Pellets consisting of Al particles with average diameters of 40-60 nm and 60-80 nm are examined. It should be noted that although the ignition of an Al pellet is expected to be a multi-scale problem involving heating individual nanoparticles and subsequent heat and mass transfer across the surface and throughout the pellet, the focus here is to characterize the burning mechanism at the macro scale (taking the pellet as a porous structure). The Al particles are consolidated in pellets of a higher porosity in order to address the following issues. First, a large diffusion length between individual particles means O_2 can be transported easily in the porous structure. In this case, the classical diffusion limiting rate is expected. Secondly, since the pellet has a clearly defined physical structure, its ignition and burning may be modelled numerically using CFD software which solves the conservation equations in the continuum regime.

4.2.3. Experimental

4.2.3.1. Pellet preparation

Aluminium nanoparticle powders were obtained from Skyspring Nanomaterials Inc. with the following APS (Aerodynamic Particle Size) diameters: 40-60 nm and 60-80 nm (data provided by the manufacturer). The nanoparticle powders were dispersed in 10 mL of hexane and sonicated for 20 minutes in order to reduce particle agglomerations. The solution was then dried in a fume hood for 10 hours. Dried samples were mechanically consolidated in a casting vessel to form cylindrical pellets with a diameter of 6 mm. Density variations among the pellets varied from 1.2 to 1.6 g/cm^3. The mean porosity of the pellets was estimated using the density of bulk aluminium as the theoretical maximum density (TMD). Mean porosities were found to be 49% and 46% TMD for the 40-60 nm and 60-80 nm pellets, respectively.

4.2.3.2. Laser ignition setup

The experimental setup shown in Figure 3.2 was used. The Al pellet was supported on a T-shape bracket within a spherical stainless steel vessel equipped with quartz viewing windows. A Spectra-Physics 2017-04S 4 W continuous wave (CW) Argon laser (1.4 mm beam diameter at 1/e^2 wave attenuation) was used to ignite the pellet by heating its top surface. After the shutter was on, an electro-mechanical device triggered the photodiode (Thorlabs, Model DET36A), which was mounted orthogonally to the viewing chamber. Meanwhile a 15 fps digital camera (Canon, PowerShot S3 IS) was initiated to visualize the flame propagation. Video recordings and light emissions were captured simultaneously. An oxygen tank, a vacuum pump and a pressure transducer were used to regulate the O_2 pressure. The following two test cases were analyzed for each nanoparticle size: 1) O_2 pressure was fixed at 3.15 bar, and laser power was varied from 2.5, 3, 3.5 to 4 W; 2) Laser power was fixed at 3.5 W, and O_2 pressure was varied from 2.14,

2.64, 3.14, 3.64, 4.14 to 4.64 bar. Each operating condition was repeated up to eight times in order to improve experimental uncertainties.

4.2.4. Results and discussion

4.2.4.1. A simplified diffusion controlled model for Al nanoparticle pellet

A simple diffusion controlled combustion model describes the burning of an Al pellet by assuming that combustion is limited by the O_2 diffusion through the reaction interface.

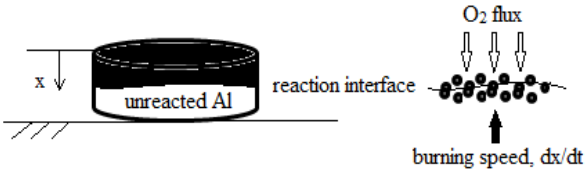

Figure 4.15: Sketch of the diffusion combustion model (Al particle reacts instantaneously with oxygen)

Figure 4.15 depicts a simplified model of diffusion controlled burning of an Al pellet. As illustrated in Figure 4.15, the burning speed is estimated using the flux of O_2 through the reaction zone interface. At the macro scale, this flux is proportional to the effective diffusivity of oxygen within the porous structure. Assuming a constant diffusivity of O_2, the burning velocity, *dx/dt*, is defined as

$$\frac{dx}{dt} = v_b = \frac{D_e c_{oxy,bulk}}{x c_{Al}} \qquad \text{(Eq.4.1)}$$

where D_e is the effective diffusivity of oxygen in the pellet, $C_{oxy,bulk}$ is the bulk concentration of oxygen given by its pressure, C_{Al} is the concentration of aluminium given by the pellet density, and x is the distance measured from the laser heated surface. It should be noted that according to the diffusion controlled mechanism, the chemical reaction is infinitely fast (i.e. Al nanoparticle

reacts instantaneously when it comes in contact with O_2). Eq. 4.1 indicates a hypothetical infinite burning velocity at the laser heated surface since there is no barrier to diffusion. In fact, the actual O_2 diffusion is also dependent on the heated zone which moves together with the flame front [3]. However, this is not considered here. Eq. 4.1 is then integrated along the height of the pellet to estimate the burn time,

$$t_b = \frac{h^2 c_{Al}}{2 D_e C_{oxy,bulk}} \quad \text{(Eq.4.2)}$$

where h is the height of the pellet. Eq. 4.2 indicates that the burn time reduces with the oxygen concentration. In order to determine the effective diffusivity of O_2, the Knudsen number is needed as shown in Eq. 2.1, with the mean free path of oxygen in a porous Al pellet with a mean particle diameter. At the temperature of 600 ºC, which is near to the melting temperature of 40 nm to 80 nm Al particles [57], the mean free path of oxygen is $\lambda oxy \approx 210$ nm, and Knudsen number is $Kn \approx 2.5$ to 5. For this study it is reasonable to assume the effective diffusivity, D_e, is equivalent to the Knudsen diffusivity, D_k. Then according reference [145]

$$D_e = D_k = \frac{d_{pore}}{3} \sqrt{\frac{8RT}{\pi M_{oxy}}} \quad \text{(Eq.4.3)}$$

where d_{pore} is the mean pore diameter, R is the universal gas constant, T is gas temperature, and M_{oxy} is the molecular weight of oxygen. It should be noted that this gas diffusion value is several orders of magnitude larger than the diffusion of O_2 within the alumina shell at the nano scale. For instance, at T = 600 C and d_{pore} = 100 nm, the Knudsen diffusivity through the pellet is approximately $2.6 \cdot 10^{-5}$ m^2/s, whereas the solid shell diffusion within an Al nanoparticle was estimated to be on the order of 10^{-13} m^2/s [46] [53]. In addition, the theoretical analysis in this

work does not account for the initial amorphous alumina shell that protects the Al core. The model predicted pellet burning times will be compared to the measured values in the following sections.

4.2.4.2. SEM images

Figure 4.16 shows SEM images near the center top surface of 40-60 nm and 60-80 nm Al pellets, at 30k and 80k magnification. Laser irradiance is highest in these regions during ignition. The top images (30k magnification) suggest that surface of the 40-60 nm Al pellet is smoother than that of the 60-80 nm Al pellet. Upon closer inspection at a magnification of 80k, as shown in the bottom images, some agglomerates (highlighted on the images) are visible in both samples. Due to larger size of individual nanoparticles in the 60-80 nm pellet, the agglomerates in this sample exhibit a larger size than those in the 40-60 nm sample. The particle distribution on the surface plays a significant role in the ignition characteristics of the pellet. These effects are discussed in the subsequent sections.

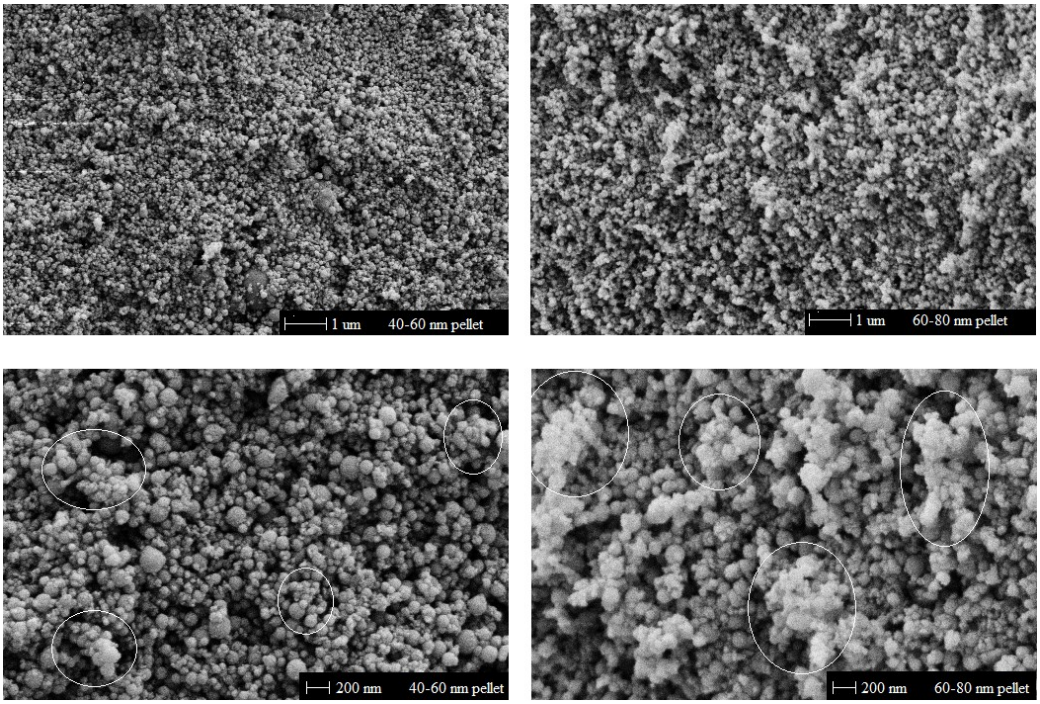

Figure 4.16: SEM images of Al nanoparticle pellets. Top: 30k magnification; Bottom: 80k magnification

4.2.4.3. Ignition Delay, Flame Propagation and Burn Time Measurements

The ignition delay was determined from the photodiode data. This instant was estimated by a sudden increase followed by a nearly uniform signal histogram, which indicates steady flame propagation. The ignition delay was also validated with the ignition delay computed via the images. It should be noted that localized surface reactions followed by material ablation were observed in some ignited pellets (in particular, the 60-80 nm pellets). Multiple ignitions of the ablated material and aluminium vapor were also observed in the photodiode signal. Such unwanted ignitions were caused by thermal instabilities within the pellet which can be attributed to larger nanoparticle agglomerates on the heterogeneous surface. Although this phenomenon is directly related to energy absorption on the surface, it is beyond the scope of this work.

The expansion of the gas products during the propagation of the flame front creates a flame plume that can be captured by the camera. The velocity of the flame plume expansion can be

determined by processing the video files using the Vision Research Phantom Control Camera (PCC) imaging software. It should be noted that the velocity of the flame plume is proportional to the velocity of the flame front, since the reactants and products fluxes are equivalent at the reaction zone. Since the flame cannot be clearly identified under the normal illumination, a 3x3 edge filter was utilized. Figure 4.17 illustrates the ignition and evolution of the flame plume for a 40-60 nm Al pellet. The laser was activated in the first frame and some illumination was observed due to light reflection, as shown in Figure 4.17. Ignition occurred after 12.2 s, shown in the second frame, when a clearly identifiable flame plume was developed. The growth direction of the flame plume after ignition is shown in the third frame by the vectors. Unlike the highly exothermic nanothermite reactions, the reaction between the Al pellet and O_2 does not vaporize material significantly and the pellet remained intact. As indicated in Figure 4.17, the height of the pellet is approximately 2.3 mm. Average flame plume velocities were computed by the software by measuring the flame displacement between sequential frames.

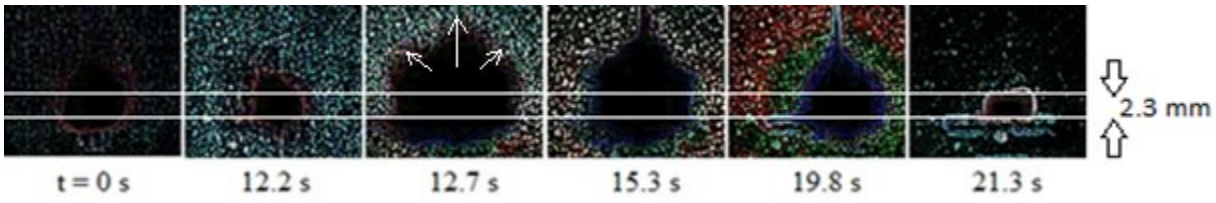

Figure 4.17: Evolution of the flame front for a 40-60 nm pellet ignited at 3.5 W and an oxygen pressure of 2.14 bar

Figure 4.18 shows the variation of the average flame plume velocities calculated from the flame images of three 40-60 nm Al pellets. These pellets were ignited at 3.5 W and 2.14 bar O_2 pressure. On average, after ignition the flame expands with a velocity of about 0.01 m/s, and then shrinks with a velocity of about 0.005 m/s before die-out. Figure 4.19 illustrates the light emission measured by the photodiode from these 40-60 nm Al pellets. In some cases, localized

ignition events were observed and led to a large error bar of measured ignition delay. Top image of Fig. 4.19 shows one example of these cases. Three pellets of 40-60 nm Al nanoparticles were ignited with a laser power of 3.5 W and an O2 pressure of 2.14 bar. The first pellet was able to ignite after many localized ignition events. The second pellet was able to ignite after a longer delay. The third pellet experienced difficulty to ignite as well. The comparison between Figures 4.18 and 4.19 suggests that the ignition delays measured by the photodiode signal and the flame images are comparable. The ignition delay values and flame burning periods are summarized in Table 4.3 for different nanoparticle sizes with specified laser power and O_2 pressure. The light emission curves with a great amount of noises were excluded.

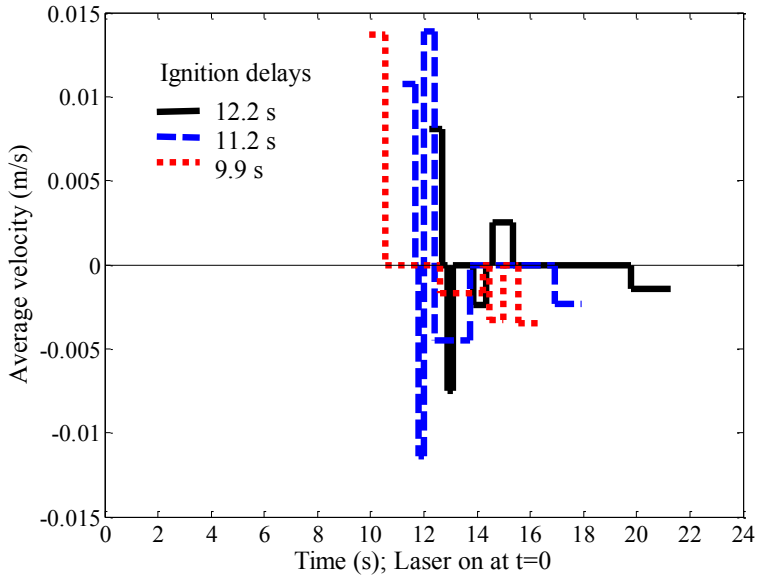

Figure 4.18: Average flame velocity for 40-60 nm Al pellets (3.5 W, 2.14 bar)

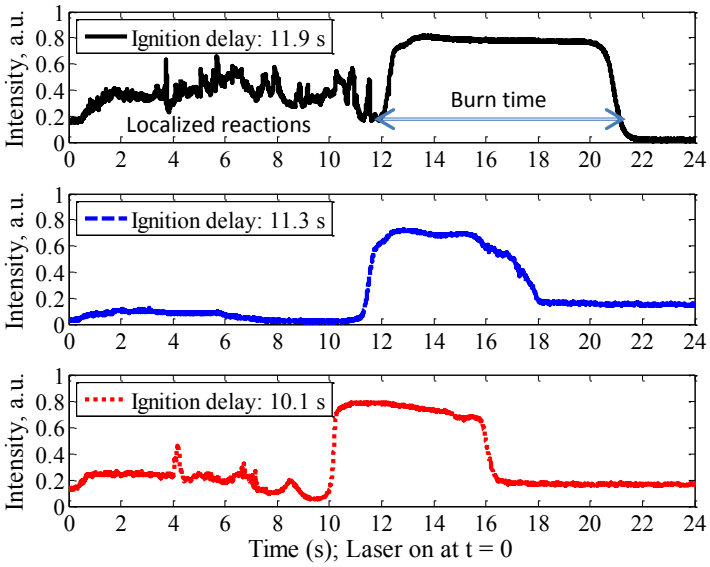

Figure 4.19: Light emission of 40-60 nm Al pellets (3.5 W, 2.14 bar)

It should be noted that ignitions of the 60-80 nm pellets at 3.15 bar O_2 pressure and 2.5 W laser power, and also at 3.5 W and 2.14 bar were not successful, unlike the more reactive 40-60 nm pellet which ignited at these conditions. Ignition delay and burn time data analyzed further in this paper are obtained from the photodiode signals.

Table 4.3: Summary of the ignition delay and burn time data

O_2 pressure fixed: 3.15 bar	**Laser power (W)**	40 nm – 60 nm		60 nm – 80 nm	
		Ignition delay (s)	Burn time (s)	Ignition delay (s)	Burn time (s)
	2.5	13.9±2.8	4.0±0.1	n/a	n/a
	3	12.8±2.7	3.6±0.4	20.9±5.9	3.8±0.9
	3.5	9.3±1.2	5.0±1.3	15.9±2.7	4.4±0.9
	4	4.4±0.2	3.8±1.1	12.2±0.3	3.9±1.3
Laser power fixed: 3.5 W	**O_2 pressure (bar)**	40 nm – 60 nm		60 nm – 80 nm	
		Ignition delay (s)	Burn time (s)	Ignition delay (s)	Burn time (s)
	2.14	11.1±0.8	7.4±1.2	n/a	n/a
	2.64	13.5±3.6	7.1±0.9	15.2±5.0	4.5±1.6
	3.14	9.3±1.2	5.0±1.3	15.9±2.7	4.4±0.9
	3.64	8.6±0.2	3.8±0.3	22.6±0.5	3.2±0.3
	4.14	5.8±3.3	3.5±1.0	9.9±3.8	3.3±0.7
	4.64	4.7±1.4	3.1±0.6	9.8±2.5	4.1±1.5

4.2.4.4. Ignition delays

Pellets made out of smaller nanoparticles are ignited faster if O_2 pressure or laser power is fixed, as illustrated in Figure 4.20. This can be attributed to higher specific surface areas in smaller particles which enhances reactivity due to larger specific surface energy [52]. It should be noted that ignition initiates on the laser irradiated surface of the pellet. Thus, in order to assess the ignition delay of Al pellets fundamentally, it is important to consider the surface microstructure and propose a criterion for ignition. Under ideal conditions, the surface microstructure is homogenous. However, particle agglomeration provides a heat shield for the inner particles, which accelerates ignition. Assuming that the mechanism of ignition in Al pellets is similar to thermal ignition of condensed phases, then ignition occurs when the rate of energy release from the reactions is greater than the rate of energy conduction and radiation away from the surface [7]. Prior to ignition, conduction is the dominant heat transfer mechanism and is proportional to the ambient gas pressure and particle diameter squared.

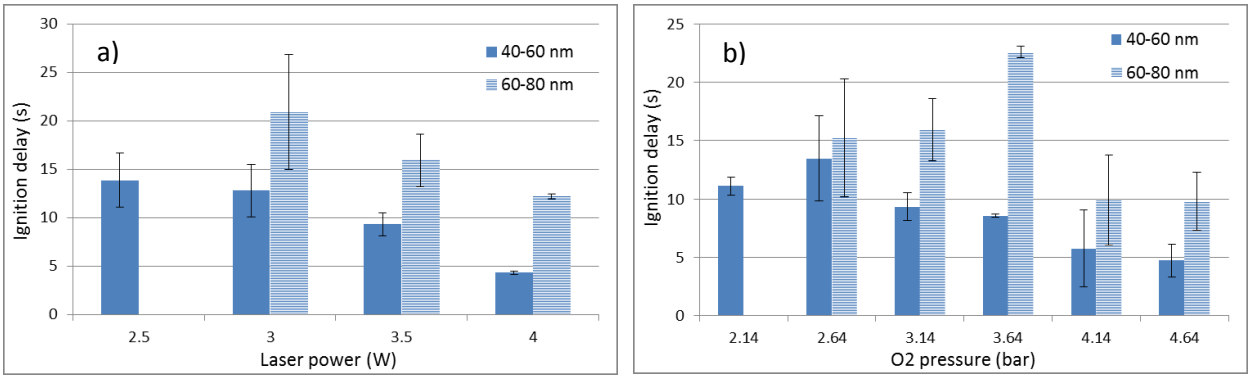

Figure 4.20: a) Ignition delay at fixed oxygen pressure: 3.15 bar; b) Ignition delay at fixed laser power: 3.5W

Figure 4.20a shows the ignition delay of the Al pellets at a constant O_2 pressure of 3.15 bars. Both types of nanoparticle show an almost linear decrease of the ignition delay with higher laser power. For the 40-60 nm pellets ignition delay reduces from 14 s at 2.5 W, to 4 s at 4 W, and for

the 60-80 nm pellets, it reduces from 21 s at 3 W to 12 s at 4 W. Higher laser irradiance enhances the rate of chemical energy release on the surface and O_2 diffusivity, which accelerates ignition. However, heat transfer on the surface increases with particle diameter, and thus ignition is delayed in larger nanoparticle pellets. Figure 4.20b shows the ignition delay of the Al pellets at a constant laser power of 3.5 W. Ignition delay appears to be inversely proportional to the O_2 pressure in the 40-60 nm pellets. It reduces from 13 s at 2.64 bar to 4 s at 4.64 bar. The higher bulk O_2 concentrations near the surface enhance the reaction rate. The enhanced reaction kinetics accelerates the chemical energy generation, which lowers the ignition delay. However, ignition delay of the 40-60 nm pellets at an O_2 pressure of 2.14 to 3.14 bar is uniform. This indicates that the heat transfer mechanism is an important factor in the pre-ignition reactions. Because the continuum regime is dominant at higher pressure, a uniform ignition delay within the range of 2.14 to 3.14 bar can be attributed to the limit of the non-continuum regime. However, the ignition delay with pressure in the 60-80 nm pellets has a non-linear trend. For O_2 pressures below 3.64 bar, ignition delay is 18 s (on average), whereas above 4.14 bar, it is about 10 s. This behavior may be explained by the transition regime between heat transfer in the Knudsen regime and continuum regime. The oxidation of individual Al nanoparticles below 100 nm is mainly controlled by reaction kinetics [7]. However, sintering and agglomeration of particles may shift the ignition mechanism toward the continuum regime. Within the Knudsen regime, heat transfer is governed by chemical reactions between Al and O_2 particles and diffusivity within the Knudsen layer. However, as O_2 pressure increases, the effect of continuum heat transfer, governed by O_2/O_2 inter-collisions is more dominant. This transition hypothesis explains the sudden decrease in ignition delay between the O_2 pressures of 3.64 bar and 4.14 bar. The size distribution of agglomerates may be a critical factor for understanding the transition regime.

SEM images in Figure 4.16 illustrate a highly non-uniform particle size distribution within the 60-80 nm Al pellet, which may be the source of relatively large error bars shown in Figure 4.20b. Alternatively, since the packing density of agglomerates is lower than the packing density of particles, thermal conductivity decreases. Hence the surface of agglomerates may enhance the ignition process at higher O_2 pressure due to less efficient heat transfer.

4.2.4.5. Burning times

The burning time of the Al pellet is governed by both heat and mass transfer within its porous structure. Pellets made of smaller nanoparticles have larger interfacial contact areas which enhance heat conduction. However, pellets made of larger particles may have higher mean temperatures prior to ignition due to longer heating periods (i.e. longer ignition delay). The mass transfer within a porous pellet is controlled by O_2 diffusivity and the length of the nanoparticles which is proportional to the particle size. Figure 4.21 illustrates the burning time of the Al pellets when a) O_2 pressure is fixed, and b) laser power is fixed.

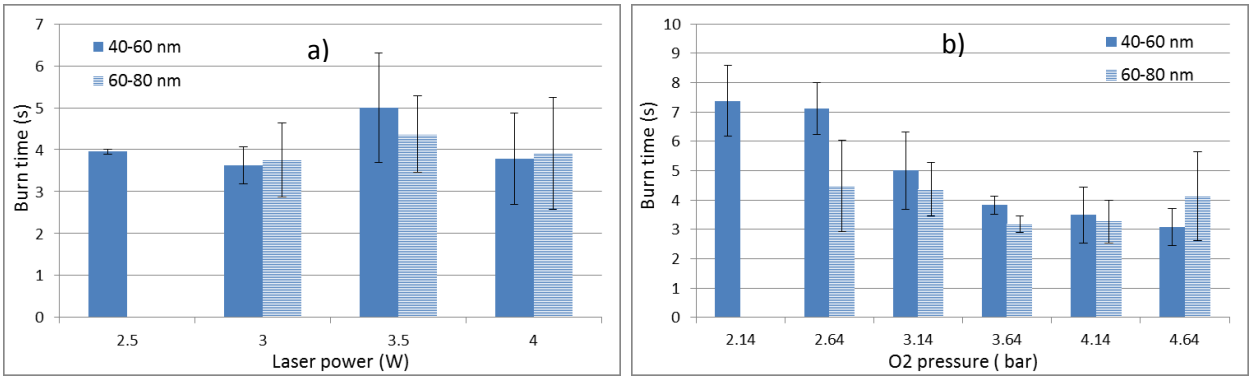

Figure 4.21: a) Burning time at fixed oxygen pressure: 3.15bar; b) Burning time at fixed laser power: 3.5 W

Figure 4.21a shows the burning time of the Al pellets at a constant O_2 pressure of 3.15 bar. Burning times appear to be independent of laser power, with all 40-60 nm and 60-80 nm pellets

having an average burn time of about 4 s. The smaller diffusion lengths in 40-60 nm pellets or the smaller interfacial heat transfer in the 60-80 nm pellets does not play a dominant role on the overall rate of combustion. Although higher laser irradiance enhances the heating rate on the surface, the relatively constant burn time indicates that bulk combustion is controlled by the chemical energy release during oxidation. Figure 4.21b shows the burning time of the Al pellets at a constant laser power of 3.5 W. Higher oxygen pressure reduces the burning time of the 40-60 nm pellets, from 7 s at 2.64 bar to 3 s at 4.64 bar. Since higher pressures enhance oxygen diffusivity, the overall burning rate increases. However, the burning time of the 60-80 nm pellets remains relatively constant between 3 and 4 s. This indicates that oxygen diffusivity may have saturated. As shown in Eq. 4.3, Knudsen diffusivity is proportional to the pore diameter and bulk gas pressure; then, the effective diffusion of oxygen saturates faster in larger particles if the mean pore diameter increases with the mean particle size. Furthermore, agglomerates and non-uniform particle size distribution increase the average pore size within the pellet. Hence the burning time of 60-80 nm Al pellets may be controlled by inhomogeneity of the pellet morphology. Additional experiments along with a more advanced theoretical model are not within the scope of this paper.

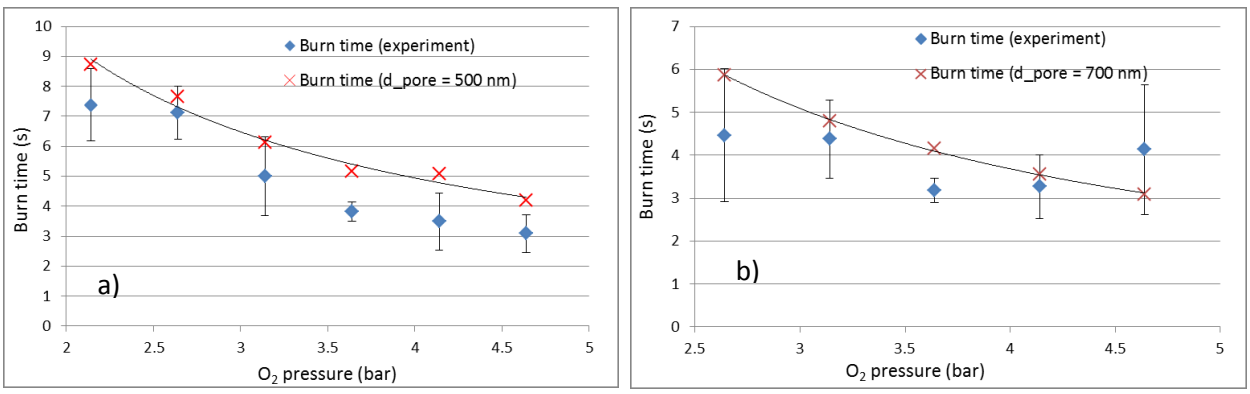

Figure 4.22: Experimental and theoretical burn time at fixed laser power: 3.5 W for a) 40-60 nm pellets; and b) 60-80 nm pellets

Figure 4.22 compares the experimental and theoretical burning times of the Al pellets at a constant laser power of 3.5 W. Theoretical burning time of porous Al pellets based on the diffusion controlled model is inversely proportional to Knudsen diffusivity, as indicated by Eq. 4.2. Based on the theoretical model sketched in Figure 2, the moving flame front ignites the Al nanoparticles instantly. Hence the burning rate must be controlled by diffusive oxygen transport. In the case of a porous structure, burning rate can be approximated by oxygen diffusing through the average pore. The mean free path under the conditions of these experiments was shown to be an order of magnitude larger than the particle size (refer to section 4.2.4.1). Because burning rate is diffusion controlled, the mean pore diameter is assumed to be on the same order of magnitude as the mean free path of oxygen (i.e. an order of magnitude larger than the mean nanoparticle diameter). This assumption gives good agreement between the burning rates calculated theoretically and those calculated via the processed images. Figure 4.22 shows that the diffusion controlled burning time has the same trend as the experimental results for the 40-60 nm pellets, but fails to describe the burning time of the 60-80 nm pellets. It should be noted that molecular diffusion is enhanced at higher pressures; hence the effective diffusion within the pellet may occur in the transition zone. For example, the harmonic mean of molecular and Knudsen diffusivities were used to model the ignition of an isolated Al nanoparticle [68]. Furthermore, since Knudsen diffusion is reduced as the mean particle diameter increases, heat transfer in the continuum regime may become an important factor in the combustion of larger nanoparticles.

4.2.4.6. Flame kernel growth rates

Several assumptions are required in order to estimate the flame kernel growth rates. First, a self-sustained flame kernel must be generated at ignition and its development is independent of the laser power. Secondly, the kernel growth rate is constant and equivalent to the acceleration of the

flame plume between two sequential frames. Using Figure 4.17 as an example, the PCC imaging software is used to calculate the average velocity, $\boldsymbol{v}$, of the flame plume boundary using the displacement vectors of the next frame after ignition. Using the average acceleration equation, the flame kernel growth rate is

$$\boldsymbol{a}_{kernel} = \frac{2\boldsymbol{v}}{\Delta t} \qquad \text{(Eq.4.4)}$$

where Δt is the time between ignition and the next frame (e.g. 12.2 to 12.7 s in Figure 4.17). Evidently, the accuracy of this result is limited by the resolution and response time of the digital camera. Figure 4.23 illustrates the flame kernel growth rates of the Al pellets.

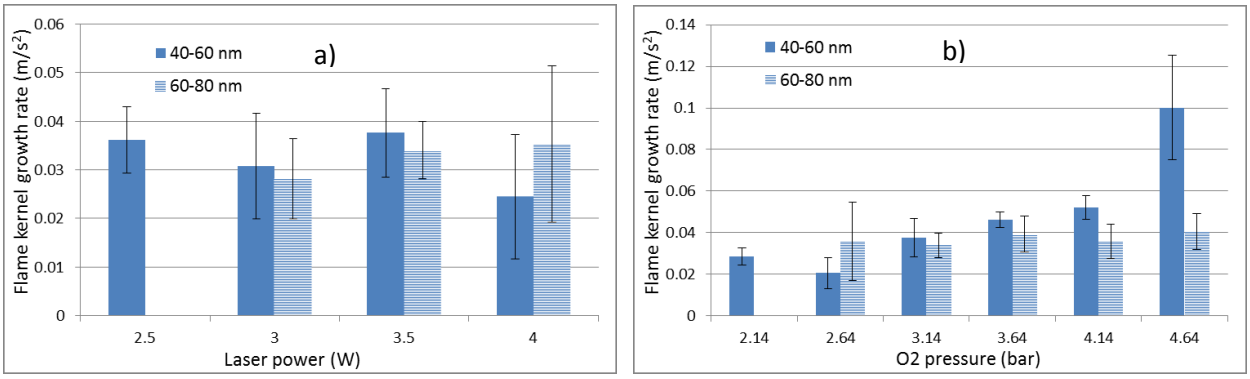

Figure 4.23: Flame kernel growth rate at: a) Fixed oxygen pressure: 3.15 bar; b) Fixed laser power: 3.5 W

Figure 4.23a shows the flame kernel growth rates at a constant O_2 pressure of 3.15 bar. The flame kernel growth rate appears independent of laser power and it averages around 0.03 m/s^2. Hence the amount of laser irradiance on the surface does not play a role on the growth rate of the flame kernel at ignition. Then, surface and bulk properties, and reactant availability at the reaction zone must dictate the pellet reactivity at ignition. Despite the higher reactivity of smaller nanoparticles, the rate of the flame kernel growth does not show any statistically significant

differences. Figure 4.23b shows the flame kernel growth rates at a constant laser power of 3.5 W. The two types of Al pellets react differently under increasing O_2 pressures. For the 40-60 nm pellets, the kernel growth rate increases from 0.03 m/s^2 at 2.14 bar to 0.1 m/s^2 at 4.64 bar. These results are expected since the reactions rates are proportional to the concentration of reactants. Hence after ignition, the rate of energy release must be proportional to the concentrations of oxygen. However, the kernel growth rate in the 60-80 nm pellets is relatively low compared to the 40-60 nm pellets. It is approximately 0.04 m/s^2 and uniform with O_2 pressure. This indicates that the amount of O_2 available for reaction is limited in larger nanoparticles, or, as mentioned previously, oxygen diffusion has saturated.

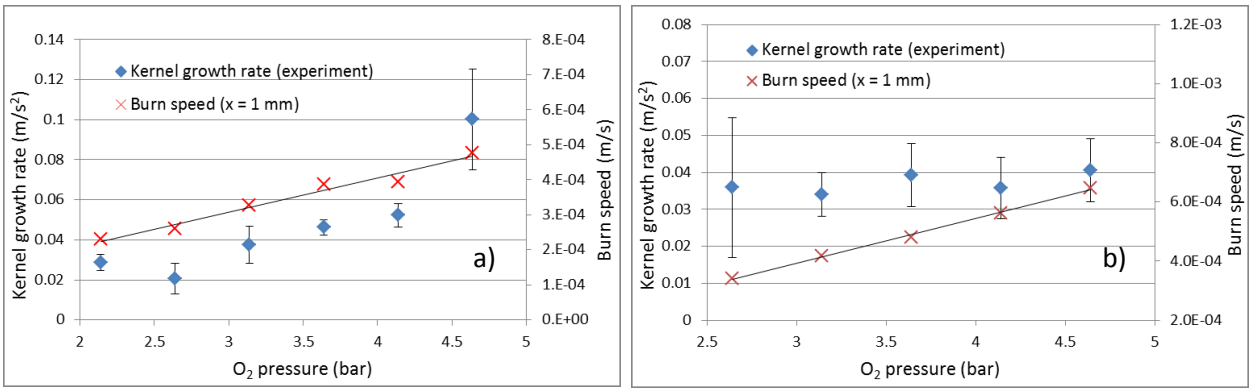

Figure 4.24: Experimental kernel growth rate vs hypothetical burn speed at fixed laser power: 3.5 W for a) 40-60 nm pellets; and b) 60-80 nm pellets

Figure 4.24 compares the kernel growth rates determined from the experimental data with the burn velocities estimated from the simplified combustion model, at a constant laser power of 3.5 W. Burn velocities are calculated using Eq. 4.1 with x = 1 mm. Recall that these velocities are hypothetical and only account for resistance to O_2 diffusion through the pellet, assuming uniform porosity and ignoring heat transfer of the moving pre-heating front. If oxygen diffusion to the reaction zone is the controlling mechanism for combustion of an Al pellet, then changes in the

burning velocity with O_2 should follow the same trend as growth of the flame kernel with O_2. Based on the hypothesis above, the plots in Figure 4.24 indicate that diffusion of O_2 within a porous Al pellet controls the burning rates of 40-60 nm Al pellets, but not the burning rates of 60-80 nm Al pellets. These results indicate that for larger nanoparticles, the controlling mechanism of ignition occurs in a transition zone. It should be noted that the burning velocities predicted are higher for pellets made out of larger nanoparticles because the effective oxygen diffusivity is higher.

4.2.4.7. Factors that affect the kinetics of combustion of Al pellets

Some of the factors that have not been accounted for in the combustion model are the pre-heating front, particle size distribution, heterogeneous porosity, the amount of active Al content within the Al nanoparticle, and the conversion of Al to Al_2O_3. The factors alter the heat transfer and mass burning rates through the pellet, and are necessary to formulate more refined models of ignition/combustion of consolidated Al nanoparticles or nanothermites. As shown in the SEM images of Figure 4.16, a heterogeneous porosity model may be necessary to obtain the effective diffusion of O_2. Such model can be developed using the analogy of effective heat diffusion in embedded structures, if the pore size distribution is known [36]. It is expected that 60-70% of aluminium is active in 40-60 nm particles, whereas 60-80 nm particles are about 80% active. However, these percentages are also dependent on the method of synthesis of nanoparticles [53]. The amount of active Al content influences the thermodynamics of combustion since it limits the energy release during oxidation. Generally, the rate of energy release during the exothermic reaction is based on the Arrhenius activation energy [52] [59]. At the macro scale, it is important to resolve the size of the pre-heated zone in order to model the heat transfer at the reaction zone accurately. Also, boundary conditions of the pellet must be known. On the laser ignited surface,

the effective heating rate depends on the particle agglomeration, absorption coefficient, and the heating rates of the laser. Within the pellet, the heat transfer is dependent on the local porosity and the conversion rate of Al to Al_2O_3, which acts like a progressive heat sink due to the much lower thermal conductivity of Al_2O_3. It is also important to consider the timescale of chemical reactions and heat transfer. Since energy release rates are controlled by reaction kinetics at the nano scale, whereas burning of the pellet is a heat diffusion problem, then appropriate numerical schemes must be used to resolve the temperature distributions.

4.2.5. Summary

The effects of laser power and oxygen pressure on the ignition and burning characteristics of Al pellets were analyzed using two different nanoparticle sizes, 40-60 nm and 60-80 nm, respectively. It was found the ignition delay is reduced by increasing the laser power at constant oxygen pressure, or increasing the oxygen pressure at constant laser power. The rate of growth of the flame kernel was found to be dependent on the oxygen pressure and not affected by the laser power. Burning times decreases with increasing the oxygen pressure. The Knudsen diffusivity of oxygen at the macro scale was shown to be the controlling mechanism in the pellets made out of smaller nanoparticles. However, larger nano-particles exhibited the non-linear burning characteristics. It was hypothesized that a heat transfer mechanism within the transition regime may be used to address ignition and combustion of larger Al nanoparticles within the pellets. The results of these experiments illustrate the importance of oxygen diffusivity on the ignition and oxidation of consolidated Al nanoparticles. There are some factors that must be addressed in the future in order to improve experimental uncertainties, such as particle agglomeration on the surface, density and porosity variations within the pellet.

5. Combustion of Al/CuO nanothermites in argon

This chapter summarizes specific research on the ignition and combustion of consolidated pellets of Al/CuO nanothermites in argon using laser ignition and high speed imaging. The research gap and objectives are outline first, and followed by the experimental and theoretical results.

5.1. Combustion Characteristics of Physically Mixed 40 nm Aluminum/Copper Oxide Nanothermites using Laser Ignition

These results were published in reference [146]. The copyright permission was obtained from the journal. F. Saceleanu conducted the experiments, analyzed the experimental data, and wrote the manuscript; M. Idir set up the experimental apparatus and assisted with the experiments; N. Chaumeix and J. Wen revised the manuscript and suggested changes for improving the quality.

5.1.1. Overview

This paper reports on the ignition and flame propagation characteristics of aluminum/ copper oxide (Al/CuO) nanothermite at different packing density, manufactured from 40 nm commercial Al and CuO nanopowders. A 3.5W continuous wave laser was used to ignite the samples in argon at atmospheric pressure, and a high speed camera captured the flame propagation. The high speed images revealed that the fast laser heating creates significant material ablation, followed by heat transfer along the heated surface. The bulk ignition occurs near the edge of the top surface, followed by the self-sustained burning. Lightly pressed powders (90% porosity) ignited in approximately 0.1 ms and the burning front propagated at around 200 m/s, while the dense pellets (40 to 60% porosity) ignited in approximately 1 ms and the burning front propagated at around 10 m/s. These results indicate that the reaction mechanism changes from mass convection to heat diffusion with increasing the packing density. The ignition and burn speeds of these Al/CuO nanothermites at different equivalence ratios, along with SEM images of

pre and post-combustion, illustrate that the homogeneity of the mixture is a critical parameter for optimizing the performance. The Al rich mixtures show significantly lower ignition delays and higher burn speeds.

5.1.2. Objectives

The objective of this paper is to observe and analyze the ignition and burning speeds of Al/CuO nanothermites that are consolidated at different densities using physically mixed 40 nm nanopowders. The effect of nanoparticle ablation on the ignition delay and the effect of stoichiometry on the burning speeds are discussed. Similar experiments in literature focus mostly on the ignition delay and flame velocity. However, in this paper high speed and resolution images of the ignition and combustion processes illustrate specific macroscopic features of the Al/CuO mixtures prior and post ignition. A new method is proposed for calculating the speed of the burning front from the reacted zone to the unreacted zone. The heat and mass transfer processes that occur at the macroscopic scale determine the nanothermite performance both kinetically, in terms of the ignition delay and flame speeds, and thermodynamically, in terms of the combustion efficiency. It is found that the reactivity of the nanothermite mixture is strongly affected by the homogeneity of the reactants, and the fuel rich mixtures show reduced ignition delay, faster burning speeds and higher pressurization rates compared to the stoichiometric mixtures.

5.1.3. Experimental

5.1.3.1. Materials and setup

Aluminum and copper oxide nano powders with APS (Aerodynamic Particle Size) diameters of 40 nm were purchased from US Research Nanomaterials Inc. The powders were added to a glass vial according to the stoichiometric or fuel rich ratios (equivalence ratio (ER) of 1.5 and 2),

assuming that the aluminum nanoparticles are 65% active (based on the oxidation limits in a thermogravimetric analyzer). Hexane (10 mL) was added to the Al/CuO mixture (1000 mg) and ultra-sonicated for 20 min to reduce agglomeration. The suspension was dried in a fume hood overnight on an evaporating plate, and then placed on a heating plate for 30 min to remove adsorbed species. The reactant mixture was consolidated at various densities using a pellet cast (6 mm diameter) and a hydraulic press, or packed lightly in an acrylic tube (7 mm inner diameter and 15 mm length). The final sample mass was 200 ± 20 mg.

The laser ignition and high speed imaging setup in Figure 3.2 was used. The pellet was held near the center of a cylindrical vessel (inner diameter of 100 mm), which was fitted with quartz windows on the ends. A continuous wave argon laser (3.5 W, 100 ms pulse duration) was used to ignite the pellet by heating its top surface, using a focusing lens to increase the power density from 225 W/cm^2 to 40 kW/cm^2. The signal from a photodiode (1 ns response time) was used to trigger a Phantom high speed camera, which was set to record at 200,000 fps and 500 ns exposure time with extreme dynamic range (EDR). A piezoelectric pressure transducer (1 μs response time) was installed on the vessel wall. Two oscilloscopes were used in order to capture high time resolution signals, and the full duration signals at lower time resolution. All tests were carried in argon at 1 atm

5.1.3.2. Methods

The ignition delay was measured using the high speed images, as the time difference between the initial laser light and the formation of the ignition front. This was also validated using the delay measured by the photodiode. The average burning speed within the nanothermite microstructure was estimated using the filtered high speed images, assuming a 2D planar burning front. Details of this procedure are described in section 3.2.5.2. The normalized time-averaged photodiode and

pressure signals were calculated according to Eq. 3.27. Additionally, SEM images of the mixed Al/CuO reactants and the combustion products were taken, and EDX analysis of the products was performed.

5.1.4. Results and discussion

5.1.4.1. Reactat characterization

The as-received Al nanopowder is spherical, with an APS diameter and a specific surface area (SSA) of 40 nm and 30-50 m^2/g, respectively. Furthermore, thermogravimetric analysis at a heating rate of 10 ˚C/min up to 1200 ˚C indicates that the active Al content is 65% by mass. Under these conditions, the Al oxidizes fully to Al_2O_3. Theoretically, a 40 nm Al particle with an active content of 65% has a SSA of 53.33 m^2/g. The higher SSA can be attributed to the particle size distribution and soft agglomeraton/aggregation of the nanoparticles. The as-received CuO nanopowder is nearly spherical, with an APS diameter and a SSA of 40 nm and 20 m^2/g, respectively. Theoretically, a 40 nm CuO particle has a SSA of 23.44 m^2/g. The SSA of the CuO nanopowder is much closer to the theoretical SSA compared to the Al nanopowder.

Figure 5.1 shows SEM images, at a magnifications of 50k, of the as-prepared Al/CuO nanothemites with ER of 1 and 1.5, and their particle size distribution (based on the diameters of 300 particles at higher magnifications, 100k to 110k). It can be seen that the stoichiometric mixture forms larger agglomerates, whereas the fuel rich mixture has larger particles. Since hexane is a nonpolar and hydrophobic liquid, the bulk density of the mixture may play a major role on the homogeneity of the suspension. The stoichiometric mixture has a higher bulk density compared to the fuel rich mixture due to the denser CuO. The most probable particle sizes are around 67 and 72 nm for the ER of 1 and 1.5, respectively. These values are larger than the APS diameters of the Al and CuO nanoparticles due to sintering during the sonication process.

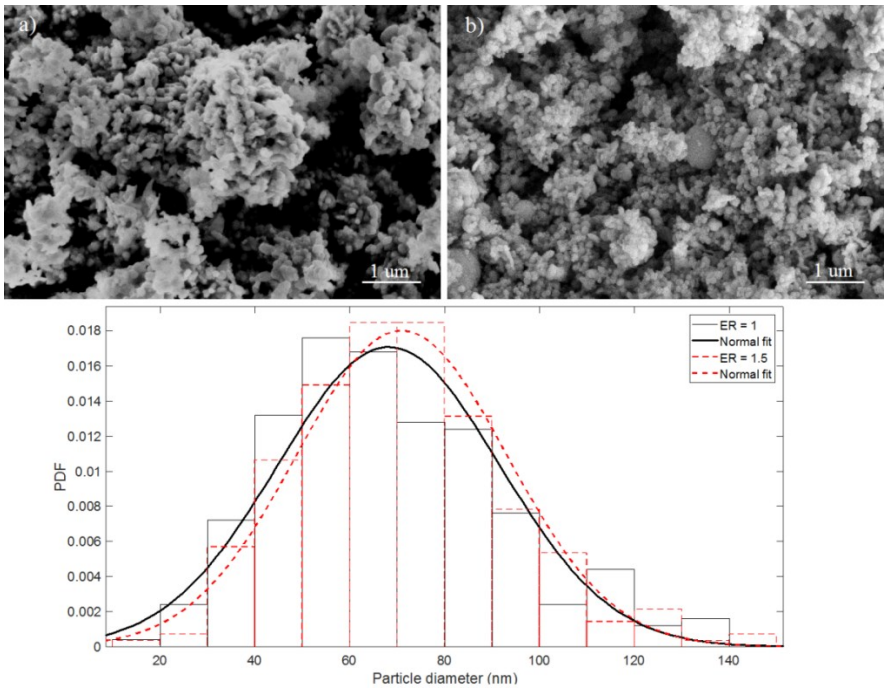

Figure 5.1: SEM images of as-prepared Al/CuO a) stoichiometric mixture, ER = 1, and b) Al rich mixture, ER = 1.5; c) Particle size distribution of the stoichiometric and Al rich mixtures

The reference theoretical maximum densities (TMD) for mixed Al/CuO nanopowders are calculated using the weight average of the Al, Al_2O_3 and CuO densities. The TMD for equivalence ratios of 1, 1.5 and 2 are 4.94, 4.61 and 4.37 g/cm^3, respectively. The bulk density of the pellets and the lightly packed powders is relative to these TMD values.

5.1.4.2. High speed imaging of the ignition and flame propagation

Figure 5.2 illustrates the high speed frames of the ignition and flame propagation in a) an Al/CuO pellet with ER = 2 and density = 37.3 %TMD, and b) Al/CuO powder in acrylic tube with ER = 2 and density = 13.8 %TMD. The 5x5 edge hipass filter in the Phantom PCC software is used to clearly show the location of the burning zones.

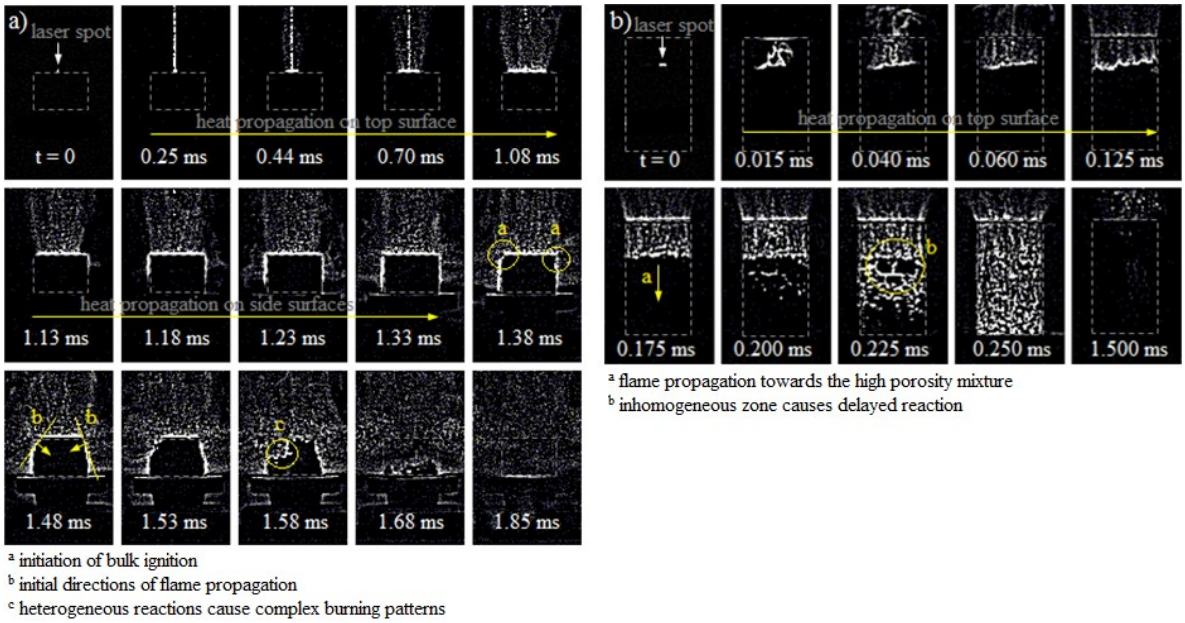

Figure 5.2: High speed frames of the ignition and propagation of the burn front within the Al/CuO mixtures for a) pellet, and b) lightly packed powder

The camera frames in Figure 5.2a show that the laser creates significant nanopaticle ablation on the pellet surface. The heat produced by the laser propagates on the top and side surfaces due to the low thermal conductivities of the Al and CuO nanoparticles, while the nanoparticle ablation continues. The time frames indicate that heat propagates faster on the side surfaces, since the heat conductivity is enhanced axially due to the compaction. The bulk ignition occurs after 1.38 ms, around the top edge of the pellet. The edges shown in Figure 5.2a are preferential locations for ignition due to the elliptical shape of the laser beam. Then, the reaction self-propagates into the unburned mixture until the pellet is disintegrated at 1.85 ms. The flame front is well defined but non-planar due to the heterogeneous reaction sites. The low porosity of the pellet impedes the combustion gases to propagate into the unburned zone; hence the heat diffusion is a major component of the heat transfer that maintains the self-propagated sustainable reaction.

The photos in Figure 5.2b show that the laser also creates significant nanopaticle ablation on the surface of the lightly pressed powders. Similarly to the pellet, the heat propagates first on the top surface. The bulk ignition of the nanothermite powder starts after 0.175 ms, and the reaction propagates downwards into the unburned mixture. The reaction front is faster and disordered due to the high porous microstructure. The reaction zone reaches the end of the unburned mixture after 0.250 ms. It is expected that the large pores reduce the resistance to mass diffusion, and gaseous and molten products penetrate through the unburned zone to break the adjacent agglomerates and effectively reduce the diffusion lengths for the reaction; hence the mass convection is a major process in the self-propagated reaction.

5.1.4.3. Ignition and ignition delay

The bulk ignition of the Al/CuO pellet was consistently initiated near the edges of the top surface, away from the laser heating spot. This phenomenon is caused by the combined effects of nanoparticle ablation and net heat transfer on the surface. Ignition temperature is not reached in the laser vicinity since the heated nanoparticles are continuously removed from the surface. Theoretically, the energy balance on the laser heated surface can be simplified to

$$\rho c_p \frac{\partial T}{\partial t} = \alpha \dot{Q}_{laser} - \left(\dot{Q}_{mix} + \dot{Q}_{Ar}\right) + \dot{Q}_{chem} \qquad \text{(Eq.5.1)}$$

where ρ is the packing density, c_p is the effective specific heat capacity, α is the absorption coefficient, $\dot{Q}_{laser}$ is the constant laser irradiance, $\dot{Q}_{mix}$ is the rate of heat transfer due to heat conduction and convection within the mixture, $\dot{Q}_{Ar}$ is the rate of heat convection and radiation to the argon, and $\dot{Q}_{chem}$ is the rate of heat release by the nanothermite reaction where its value depends on the local temperature relative to T_{ign}, the ignition temperature

$$\dot{Q}_{chem} = 0 \; for \; T < T_{ign} \quad \text{(Eq.5.2)}$$

$$\dot{Q}_{chem} > 0 \; for \; T > T_{ign} \quad \text{(Eq.5.3)}$$

The ignition temperature is reached by minimizing the $\left(\dot{Q}_{mix} + \dot{Q}_{Ar}\right)$ term. It can be assumed that the heat convection to the argon is much lower compared to the heat transfer within the mixture, which is dominated by the heat conduction since gas generation is very low before ignition. Hence the optimal conditions for the bulk ignition (thermal runaway) is around the edge of the laser heated surface, where the net heat transfer losses and nanoparticle ablation are minimized.

Figure 5.3 shows that the ignition delays increases with the packing density and the fuel rich mixtures have reduced ignition delays. As explained above, the ignition delay is controlled by the effective thermal conductivity coefficient (i.e. the porosity weighted average of the heat conductivities for the Al/CuO solid phase and the argon fluid phase). It has been shown that thermal conductivity increases linearly and absorption coefficient is uniform with density in consolidated aluminum pellets (40 %TMD to 75 %TMD) [31], and the same trend is expected to exist for Al/CuO. Therefore ignition is delayed in the denser pellets due to the larger heat diffusion on the surface and within the pellet.

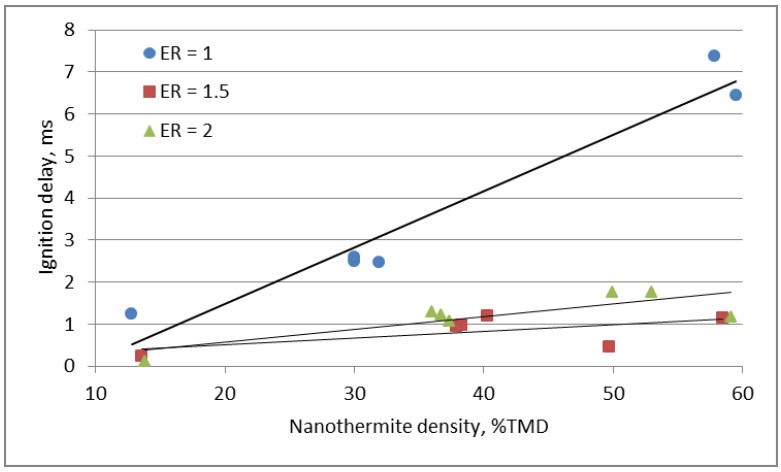

Figure 5.3: Ignition delays of the Al/CuO mixtures at different packing densities

On the other hand, for a fixed density, the fuel rich mixture with ER = 1.5 has the shortest ignition delay. This suggests that the ignition delay is controlled by both the thermal properties of the mixture and the Al/CuO interfacial homogeneity, which controls the decomposition of CuO that provides the O_2 required for the ignition. If the mixture is too fuel rich (ER = 2), the additional Al enhances the overall thermal conductivity, which delays the ignition.

It should be noted that the alumina passivation layer has a significant effect on the thermal properties of the aluminum nanoparticles used in these experiments. The thermal conductivities Al_2O_3 and CuO are equivalent, whereas the thermal conductivity of Al is an order of magnitude larger. Furthermore, the thermal conductivity of these components decreases with temperature [147]. The effective thermal conductivity is higher in the Al rich mixtures, and the laser heating propagates faster on the surface to reach the optimal conditions for ignition.

5.1.4.4. Average burning speed and reaction mechanism

The average burning speed is calculated following the procedure in 3.2.5.2. It should be noted that bulk ignition does not occur at a single location (refer to Figure 5.2a); in this paper, the

flame speeds are calculated using the reference ignition spot that provides that fastest propagation. The combustion front of the nanothermite has complex 3D burning features; however, in this paper it is assumed that the fastest 2D flame speeds define a specific Al/CuO mixture. Figure 5.4 shows the average burning speeds of the stoichiometric and the fuel rich Al/CuO mixtures. Two regimes are observed: the burning speed is on the order of 10 m/s in the consolidated pellets, and increases to the order of 100 m/s in the lightly pressed nanothermites. The tube confinement of the lightly pressed nanothermites plays a role on the flame speeds since the tube alters the rate of pressurization during combustion and the heat transfer to the argon; however, these effects are expected to be less significant than the porosity within the unreacted mixture.

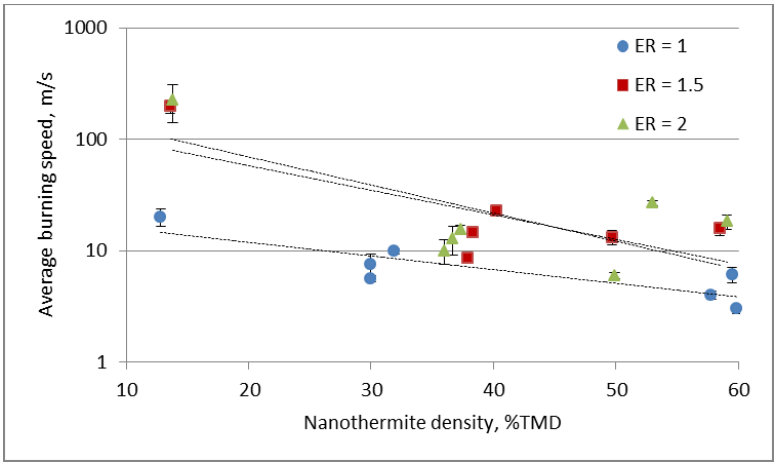

Figure 5.4: Average burning speeds in Al/CuO nanothermites at different packing densities

A similar trend was observed in Al/WO_3 nanothermites [79], and 80 nm Al nanoparticles/CuO nanorods [148]. It should be noted that the burning speeds obtained in these experiments are relatively low compared to literature data [148] since the 40 nm Al particles have significantly more alumina mass, which reduces the thermal conductivity. The 80 nm Al particles have an active content of 80% [6], compared to 65% of the Al particles used in these experiments. The

effect of the large alumina shell mass is more pronounced in the consolidated pellets due to the higher local concentration of the alumina. The flame propagation is reduced since the pressed alumina shells increase the diffusion resistance.

To further examine the effects of the bulk density on the burning velocity, the Andreev number, *An*, is examined. This has been proposed recently to explain the transition from conductive to convective reactive flow in porous media [73]. The *An* number is defined as the ratio of the convective heat transfer coefficient to the heat conduction coefficient,

$$An = \frac{\rho u d_\varepsilon c_p}{k_g} \quad \text{(Eq.5.4)}$$

where ρ is the packing density of the nanothermite, u is the average burning velocity, d_ε is the mean pore diameter, c_p is the specific heat capacity of the nanothermite, and k_g is the thermal conductivity of the gas. The mean pore diameter is found using Kozeny's equation for spherical particles [149],

$$d_\varepsilon = \frac{2}{3}\left(\frac{\varepsilon}{1-\varepsilon}\right) d_p \quad \text{(Eq.5.5)}$$

where ε is the porosity, and d_p is the mean particle diameter. The specific heat under constant pressure is determined using the porosity averaged heat capacities of the solid and gas phases. The specific heat capacity and thermal conductivity values are examined at 2000 ˚K [150] [151], assuming that the adiabatic flame temperature of 2800 ˚K is not reached. Also, it is assumed that the gas phase is a mixture of argon and oxygen, which is the major gaseous species during the reaction [152]. Table 5.1 outlines the Andreev number for the stoichiometric and fuel rich Al/CuO mixtures. Generally, *An* is between 1 and 10 in the slow burning regime, indicating that heat conduction is significant for the self-sustaining reaction. In the fast burning regime, *An* is

between 100 and 1000, which indicates that thermal and mass convection drive the flame propagation.

Table 5.1: Andreev numbers for the Al/CuO mixtures at different packing densities

ER = 1							
%TMD	12.8	31.9	30	30	57.8	59.5	59.9
An	16.5	6.5	5.1	3.8	1.7	2.5	1.2
ER = 1.5							
%TMD	13.6	37.9	38.3	40.3	58.5	49.7	
An	151.0	4.9	8.3	12.5	6.2	6.2	
ER = 2							
%TMD	13.8	36.7	36	37.3	59.1	53	49.9
An	165.6	7.2	5.7	8.6	6.9	11.5	2.7

Overall, the fuel rich Al/CuO mixtures generated higher flame speeds than the stoichiometric mixtures. Similarly, maximum pressures and burn speeds in pressure cell experiments were obtained under fuel rich conditions (ER = 1.1) [29], and this was assumed to be due to higher thermal conductivities [153]. Fuel rich Al/MO_3 also showed improved propagation velocities compared to stoichiometric mixtures, due to optimum gas and liquid Mo generation that enhances the convective heat transfer [154]. As noted in Table 5.1, the fast burning regime is reached in the fuel rich lightly packed mixtures, but not in the stoichiometric mixture. These observations indicate that the mixture homogeneity is a critical parameter for fast flame propagation, and the local reaction rates control the gas generation that drives the convective burning. In [148], the self-assembled Al/CuO composites produced higher combustion rates compared to the physically mixed powders due to the larger interfacial area.

To further study the nanothermite reaction, post-combustion SEM images of the consolidated pellets and lightly packed powder under stoichiometric and fuel rich conditions are shown in Figure 5.5. Generally, the products of the nano scale reactants are on the micro scale, and

composed of spherical Cu particles and aggregates of Al_2O_3 and $Al_xCu_yO_z$ intermetallics. Similar structures have been observed in [75] and [153].

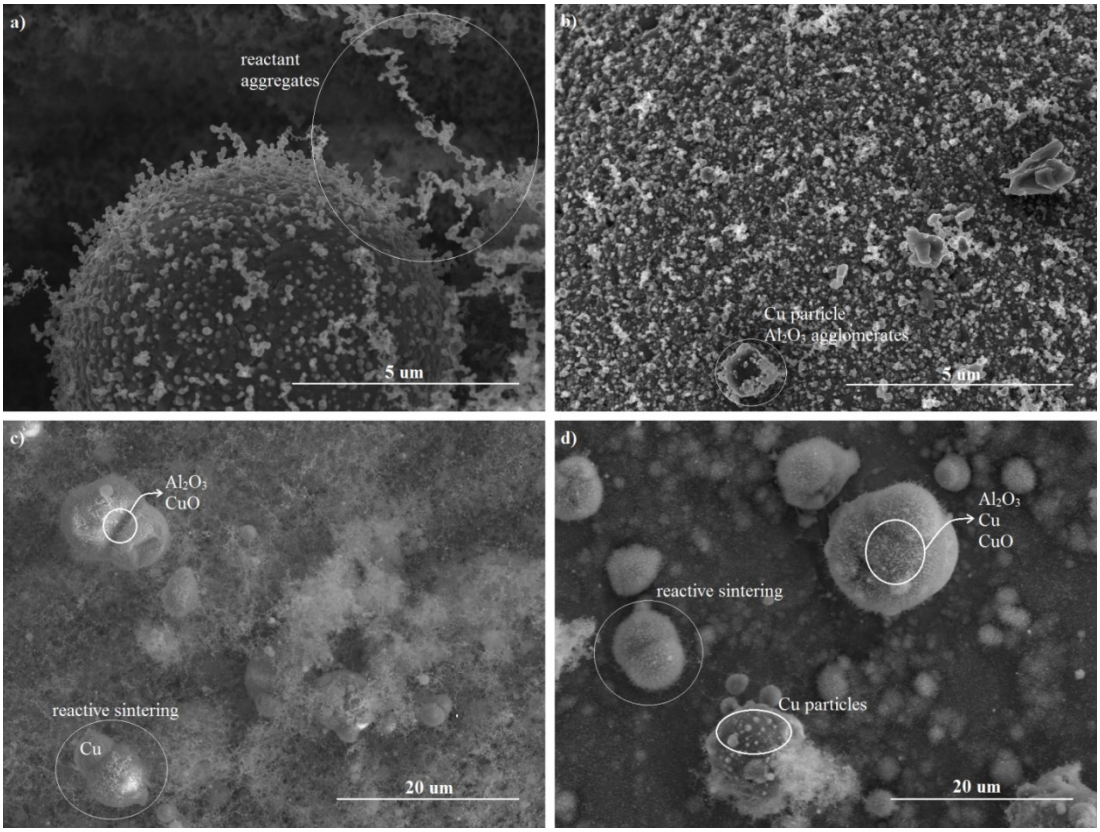

Figure 5.5: Post-combustion SEM of high density pellets with a) ER = 1 (59.5 %TMD) and b) ER = 1.5 (58.5 %TMD); and low density powders with c) ER = 1 (12.8 %TMD) and d) ER = 1.5 (13.6 %TMD)

Although the initial pellets densities of the stoichiometric and fuel rich mixture in Figures 5.5a and 5.5b are similar, the morphologies of the products are different. The reactant aggregates observed in the post-combustion of the stoichiometric pellet indicates a highly incomplete combustion. This is attributed to the larger reactant agglomerates, and inhomogeneous mixing, shown previously in Figure 5.1a as compared to Figure 5.1b. The products of the lightly pressed nanothermites in Figures 5.5c and 5.5d show that reactive sintering occurs in the highly porous mixtures. Despite the high porosity that promotes convection, the condensed phase reactions are

much faster than the heterogeneous reactions. For example, the reaction time of Al and CuO in condensed phase is on the order of 1 μs [155], much faster than the burning time of Al nanoparticles in an oxygen atmosphere which is on the order of 100 μs [44]. It should be noted that significant reactant aggregates exist in the products of the stoichiometric loose powders (Figure 5.5c), which is evidence of an incomplete combustion. Incomplete Al/CuO reactions have also been reported in [153] [156]. The large ignition delay and the low burning speeds of the stoichiometric mixtures are mainly caused by inhomogeneous mixing of the reactants that limits the local Al-CuO reactions in the condensed and heterogeneous phase. Consequently, this limits the gas generation that promotes the mass convection, and the combustion temperature that promotes the heat conduction.

5.1.4.5. Reaction performance of the pellets

The photodiode and pressure signals were analyzed for the different pellet densities in order to assess their performance. The key factors depend on the application. For example, propulsion and igniter applications required fast pressurization rates, whereas welding applications require high reaction temperatures. It should be noted that the pressure transducer was not installed in the reaction zone; hence the pressure signals are only used for comparison purpose.

Figure 5.6 shows the raw signals of the photodiode and pressure transducer during the combustion of a high density Al/CuO pellet with ER = 1.5. The reaction occurs before the gas release, and the burn duration is faster than the pressurization time. It should be noted that some researchers observed the decomposition of CuO prior to the ignition; however, the pressure transducer in these experiments can only measure the overall pressurization near the vessel walls.

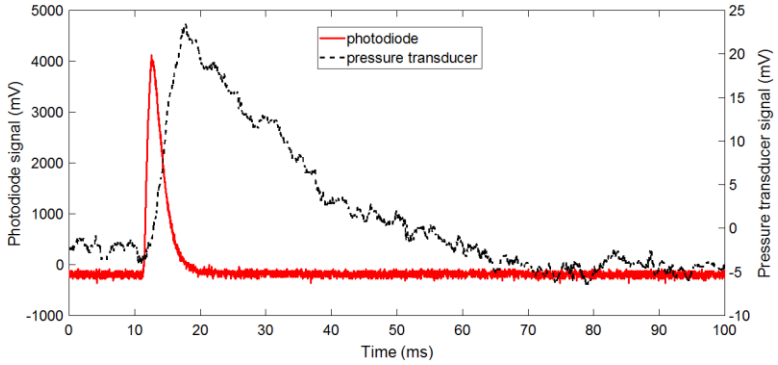

Figure 5.6: Raw photodiode and pressure signals for a high density pellet with ER = 1.5

Figure 5.7 shows the normalized and time-averaged photodiode and pressure signals of the Al/CuO pellets. The normalized time-averaged photodiode signal term represents the specific energy release rate by the reaction. This term is independent of the density, which indicates that the degree of oxidation of Al is similar. The mixtures with ER of 1.5 have a larger normalized photodiode signal compared to the mixture with ER of 2 since the extra Al in the richer mixture acts as a heat sink.

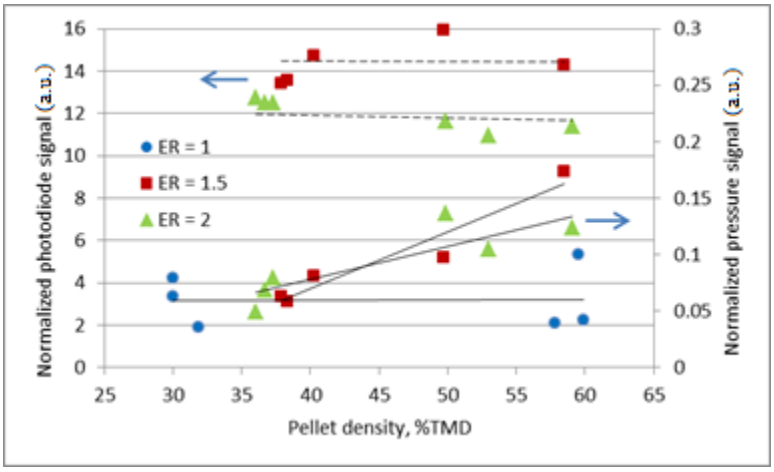

Figure 5.7: Normalized photodiode and pressure signals of the Al/CuO pellets at different packing density

The normalized time-averaged pressure signal increases linearly with the pellet density. A similar linear increase with the density was also observed for the pressurization rate, which is estimated from the slope of the raw pressure curve. The higher pressure rates in the denser pellets are caused by the reduced volume for gas expansion, which is also predicted by a theoretical model assuming local thermodynamic equilibrium [152]. Furthermore, it is expected that the consolidated Al and CuO reactants have more reactive interfaces, which enhance the initial reaction rates in the condensed phase. In [156], the maximum pressure and pressurization rates of Al/CuO pellets also increase with the %TMD. Theoretically, much higher pressures are predicted since the actual gas phase chemistry is unknown. It should be noted that the normalized pressure signals of the stoichiometric Al/CuO pellets are low compared to the fuel rich mixtures, and independent of density. This is further indication that the local reaction rates are inhibited by the homogeneity of the mixture.

The burning durations of the Al/CuO nanothermites in these experiments, as measured by the duration of the photodiode signal, are an order of magnitude longer than the durations of flame propagation. This indicates that the degree of oxidation of the Al nanoparticles is limited by the heterogeneous $Al - O_2$ reactions. In [153], temporal temperature measurements in Al/CuO nanopowders were near the flame temperature of Al particles in air (~ 4000 ˚K). Thus, in order to improve the reactivity of these nanothermites, the Al-CuO interfaces should be optimized to ensure that most of the reaction initiates in the condensed phase, and oxygen decomposition from the CuO can readily react with the Al.

5.1.5. Summary

The experiments show that the reactivity of physically mixed Al/CuO nanothermites is highly sensitive to the homogeneity, equivalence ratio and packing density of the mixture. The fuel rich

mixtures burned much faster than stoichiometric mixtures due to formation of smaller agglomerates in the reactants. The ignition delay on the pellet surface is controlled by the nanoparticle ablation and the net heat transfer on the surface, such that the pellet edges are the preferential spots for the bulk ignition. The propagation speed of the burning front increases from an order of 10 m/s in the consolidated pellets (40 to 60 %TMD) to an order of 100 m/s the in lightly packed powders (10 %TMD). Enhanced flame speed is caused by a change in the controlling mechanism from heat conduction to mass convection with decreasing the packing density. The reactivity of the Al/CuO pellets increases generally with the packing density, whereas the normalized pressurization rate increases linearly with the density.

5.2. Low-power Laser Ignition of Al/CuO Nano powders and Al/Cu_2O Nanolaminates

Parts of these results were published in reference [157]. The copyright permission was obtained from the conference. F. Saceleanu prepared the mixtures, analyzed the experimental data, and wrote the manuscript; L. LeSergent and H. Sui prepared the mixtures; J. Wen and C. F. Petre revised the manuscript; D. Chamberland, P. Beland and T. Ringuette set up and run the experiments.

5.2.1. Overview

Nanothermites are a class of highly energetic materials composed of solid state fuel and solid state oxidizer with tunable combustion properties. This study investigates the ignition and reactivity of Al/CuO mixed nano powders, and multi-layered micro structures, and Al/Cu_2O sputtered nanolaminates. A low power (2.97 W) diode laser was used to ignite the thermites in atmospheric air, and a photodiode and high speed camera were used to measure the ignition delay and the rate of expansion of the flame plume, which were related to the energy release rate.

The ignition mechanisms of the powder and sputtered structures are fundamentally different. Energy balance on the laser heated surface controls the ignition delay in mixed powders and multi-layered micro structures, which depends on the net thermal conductivity and the resistance to heat diffusion. Ignition delays of the mixed nano powders and multi-layered micro structures range from 1 ms to 100 ms. Reactivity can be optimized by homogenizing the Al/CuO interfaces. On the other hand, laser energy absorption is mandatory for the ignition of the sputtered nanolaminates. Since the size of the sputtered layers is on the nano scale, laser penetration can reach the Al/CuO interface. The ignition delay can be minimized by finding the optimum Cu_2O thickness that maximizes both the absorption coefficient and the oxygen diffusion rates. Localized laser heating of the top Al/Cu_2O interface causes rapid Cu_2O decomposition and subsequent reaction of the Al layer with the oxygen. Ignition delays of the sputtered nanolaminates range from 0.1 to 0.8 ms.

5.2.2. Objectives

The purpose of this study is to measure the ignition delay and reactivity of Al/CuO nano powders and multi-layered micro structures, and Al/Cu_2O sputtered nanolaminates. We focus on the Al/Cu_2O nanolaminate since decomposition of CuO to Cu_2O and O_2 occurs prior to oxidation of Al to Al_2O_3, hence the Al-Cu_2O interaction may be a controlling mechanism of combustion [158]. The laser pulse provides non-intrusive ignition energy, and has been used successfully in few previous experiments [136] [32]. The ignition delay, reactivity, and reaction mechanisms of the nanothermite structures are determined by analyzing the photodiode, high speed camera frames, and SEM data.

5.2.3. Experimental

Aluminum and copper oxide nano powders, with mean particle diameters of 40 nm, were purchased from US Research Nanomaterials. TGA analysis indicated that the Al nanoparticles were 65% active. The nanopowders were mixed in a glass vial using ethanol, followed by ultra-sonication to reduce agglomeration, and the suspension was dried overnight in a fume hood. The reactant mixture was consolidated using a pellet cast and the resulting density was measured relative to the theoretical maximum density (TMD). The multi-layered micro structures were formed via vacuum filtration. Al or CuO suspensions were ultra-sonicated in ethanol, and the layer thickness was varied by controlling the deposition rates on filter paper substrate. Each structure had a total of 11 layers.

The sputtered nanolaminates were formed via magnetron sputtering from Al and Cu targets onto a photoresist covered glass substrate. The Al layers were sputtered in an argon atmosphere to ensure that pure Al was deposited, whereas the Cu was sputtered in an Ar-O_2 environment to ensure that Cu_2O was deposited. The deposition process is highly controllable; the nano layer thickness was varied by controlling the deposition time on glass substrate. After sputtering is complete, the photoresist layer is dissolved so that the nanolaminates are free standing, and they form small flakes. Details of this procedure can be found in reference [159].

A diode laser (2.97 W, 200 ms pulse duration, 808 nm wavelength) was used to ignite the nanothermites that were contained in a small crucible. A photodiode (Osram SFH206K) was used to record the light intensity, and a high speed camera (Photron Fastcam SA1.1) operated at 100,000 fps was used to record the combustion event. An experimental setup similar to the setup shown in Figure 3.2 was used.

5.2.4. Numerical models

5.2.4.1. Laser ignition of Al/CuO pellets

The ignition delay of laser heated Al/CuO nanothermite pellets was simulated using the Ansys Fluent software, following the model described in section 3.2.4. The solver uses the 2D axisymmetric transient scheme. The uniform quad meshing method was implemented with an element size of 0.005 mm and 51340 elements. Iterations were made in choosing this size mesh and it was concluded that results do not change by more than 5% if mesh is refined more. The convergence criterion was set to 10^{-8} for the scaled residuals of temperature and simulations are initiated at an ambient temperature of 300 K with fixed time-step of 10 μs. This ensures Von Neumann numerical stability. The heat transfer coefficient for natural convection in air was assumed to be 10 W/m^2K and the surface emissivity was set to 0.9 for the radiation heat transfer. The activation energy for consolidated Al/CuO nanoparticles was not found in literature; instead, the E_a values for nano layered Al/CuO [160] and Al/air [161] was used since the Al/CuO pellets were ignited under atmospheric conditions. The E_a was set to 50 kJ/mol and the pre-exponential was set to 10,000,000 Hz, and these values have similar magnitudes to other laser ignited nanothermite studies in literature. The enthalpy of combustion was set to the theoretical value of 4075 kJ/mol. The model simulates the heat equation prior to ignition, hence only a solid domain was defined. The model was validated by decreasing the element size in the mesh until the maximum temperature and temperature rate on the laser heated surface did not vary by more than 10%.

Figure 5.8 illustrates an example of the temperature distributions in the modeling domain just prior to ignition. Note that the temperature is in degrees Kelvin, and is lower than the melting

temperature of Al nanoparticles. Hence the onset of the exothermic reaction is expected to occur in solid state, which agrees with literature data.

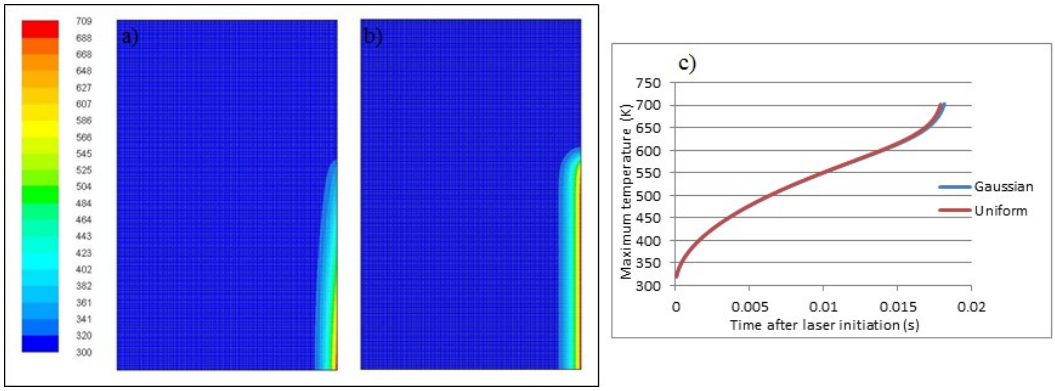

Figure 5.8: Temperature distributions in the center plane of the 2D axisymmetric domain for a) Gaussian laser beam, and b) uniform laser beam; c) maximum temperatures on the laser heated surface

Figures 5.8a and 5.8b illustrate that most of the pellet remains at ambient temperature, and a thin thermal layer forms near the heated surface. This thin heated region is more developed for the uniform beam distribution, since laser fluence decreases exponentially for the Gaussian beam. However, the temperature gradients on the laser heated surface are similar as shown in Figure 5.8c. The thickness of the thermal heated region is approximately 0.2 mm due to the low effective thermal conductivity of the nanothermite pellet. This thickness is similar to the results of theoretical model in literature. The thermal heated region decreases for higher laser powers since the heating rate on the surface increases. As shown in Figure 5.8c, the ignition delay is approximately 18 ms for either the Gaussian or uniform beam distributions. This ignition delay is caused by the asymptotic increase in the maximum temperature of the domain due to the exothermic reaction. Furthermore, the heating rate prior to ignition is approximately 13,000 ˚K/s; however, the maximum heating rate reaches 1,000,000 ˚K/s at ignition. It should be noted experimental data shows that optimal ignition delay is attributed to a laser power that maximizes

heat flux and minimizes ablation at the surface. Ablation was observed due to thermal stress at the surface that causes reacted and unreacted material to be removed [136] [146]. The ablation peaks were determined by measuring the photodiode intensity, and were observed at about 2 ms for mid and high power laser fluences. Hence the assumption of isotropic material properties in the domain is largely dependent on the laser fluence. In these simulations it was found that the heat release due to localized combustion has major contribution to the global heating rate prior to ignition. By monitoring the maximum temperature on the heated surface and the maximum temperature in the solid domain, it was found that the rate of heating on the surface or inside the domain was similar for a given laser power.

5.2.4.2. Laser absorption in Al/Cu_2O nanolaminates

The laser absorption in the Al/Cu_2O nanolaminate structures was simulated using the model in reference [159]. The Lumerical software, based on the finite-difference time-domain method (FDTD), was used to create the domain shown in Figure 5.9. The electromagnetic radiation from the laser is absorbed in the Al/Cu_2O nanolaminate using the material properties such as index of refraction, permittivity) in the Lumerical database.

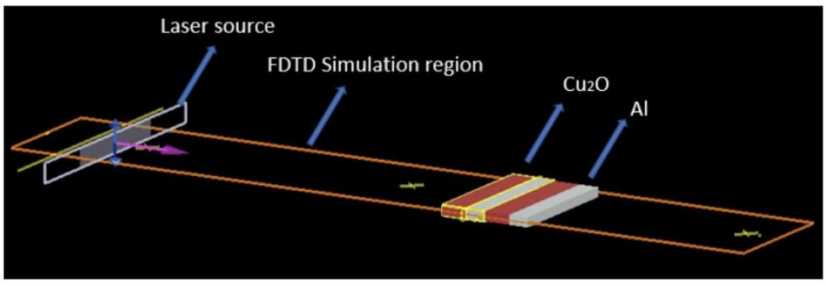

Figure 5.9: Simulation region for the laser absorption model (the work was performed in collaboration with Yiqi Zhang)

The laser absorption data from reference [159] was used to complement the ignition delays determined experimentally.

5.2.5. Results and discussion

5.2.5.1. Ignition of the consolidated Al/CuO pellets

Figure 5.10 shows that the ignition delay of stoichiometric and fuel rich (ER = 1.5) Al/CuO nanothermite powders increases with density from 1 ms at 10 %TMD to 100 ms at 50 %TMD. This can be explained by the energy balance on the laser heated surface, which is given by the constant laser power, and losses due to conduction within the powder and convection/radiation to the surrounding air. It has been shown that thermal conduction increases linearly with bulk density [31], and thus the total energy loss is greater in denser nanothermites. Furthermore, the fuel rich mixtures are ignited faster, due to better mixture homogeneity [146] that increases the number of fuel-oxidizer interfaces. The simulations also show higher ignition delays with the thermite density; however, the trend is not identical to the experimental trend. As illustrated in Figure 5.10, the short ignition delays in the lightly packed pellets are predicted better for the serial mode of the effective thermal conductivity, whereas the long ignition delays in the dense pellets are predicted better for the parallel mode of the effective thermal conductivity. It is expected that the actual effective thermal conductivity of the pressed nanothermites is between the series and parallel modes.

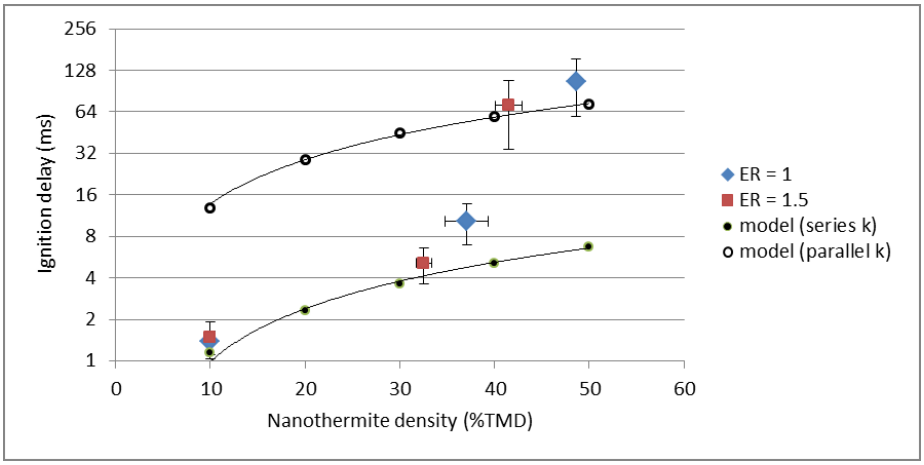

Figure 5.10: Ignition delays of Al/CuO pellets with density

The time-averaged photodiode signal normalized by the sample mass (0.012- 0.013 μA/mg) is independent of the density as shown in Figure 5.11a. This means that the normalized average energy release is constant with density. However, the initial rate of expansion of the flame plume increases with density from 0.35 m^2/s (10 %TMD) to 1.6 m^2/s (50 %TMD). The Al/CuO reactants are in closer proximity in compressed mixtures, and this increases the number of interfaces and interfacial area, thus enhancing the reaction rates. Figure 5.11b shows the initial flame velocities and the average acceleration of the flame plume, which were calculated following the procedure in section 3.2.5. The initial velocity is higher in the denser pellets due to the higher density of Al/CuO interfaces where the reactions initiate. However, the average acceleration is higher in the lightly packed pellets since the higher porosity allows for faster gas expansion.

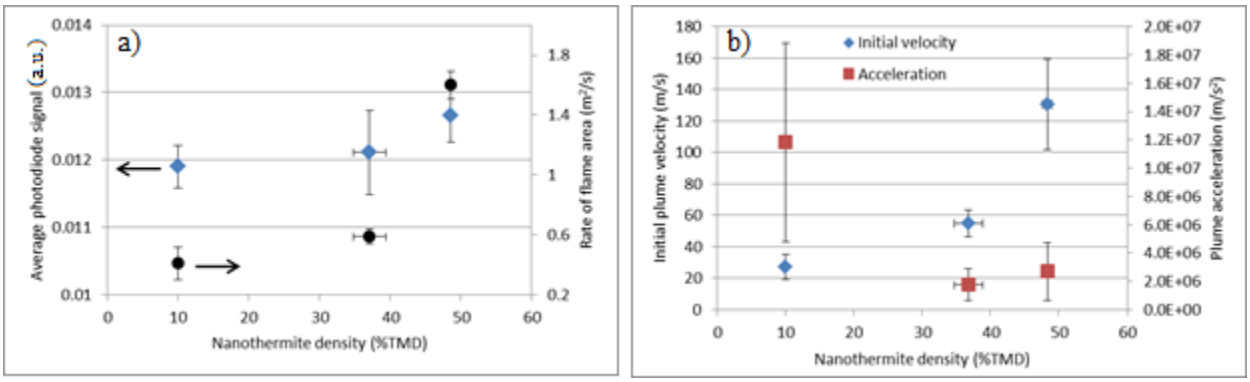

Figure 5.11: a) Reactivity of the stoichiometric Al/CuO pellets with density; b) Flame plume velocities and accelerations

Figure 5.12a is an SEM image of the mixed and sonicated Al/CuO nano powders, where some degree of agglomeration can be observed. The SEM images in Figures 5.12b and 5.12c illustrate the product morphology for initially 50 %TMD and 36 %TMD pellets, respectively. The reaction products are particles and agglomerates on the micron scale. This indicates that most of the

reaction went through a condensed phase mechanism, such as reactive sintering [28]. The spherical particles/agglomerates are mostly Cu, which are contained in Al_2O_3 matrices. The higher porosity in a pellet facilitates CuO dissociation, and O_2 gas and reaction products to move into the unreacted zone with the flame propagation. The smaller size of Cu agglomerates in Figure 5.12c compared to Figure 5.12b indicates that the heat release density is smaller in the lower density pellet. Also, the solidified pools of Al_2O_3 rather than Al_2O_3 matrices around the Cu particles indicate that molten Al_2O_3 moved with the gas propagation within the pellet and solidified upon cooling at the end of the reaction. Porosity plays a key role, and it has been proposed that the controlling mechanism of combustion changes from thermal conduction to mass convection with increasing porosity [33] [162].

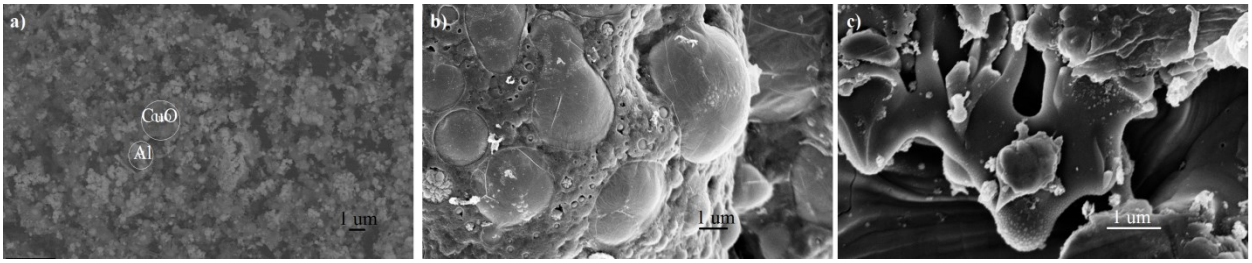

Figure 5.12: SEM images of nano powders with ER = 1, a) reactants, b) products, 50 %TMD, and c) products, 36 %TMD

5.2.5.2. Ignition of Al/Cu_2O nanolaminates

Figure 5.13 shows the ignition delay of the sputtered nanolaminates with constant Cu_2O or Al thickness. The ignition delay does not show significant variation for a constant Cu_2O layer and different Al layer thicknesses. However, for a constant Al layer thickness (45 nm), there is an optimal Cu_2O layer thickness (approximately 60 nm) that minimized the ignition delay to approximately 200 µs. The concave up dependence of the ignition delay on the Cu_2O thickness indicates that the energy required to reach ignition is a trade-off between laser energy absorption and mass diffusion. The laser energy absorption is reduced in the thinner Cu_2O layers [163],

which causes an increase in the ignition delay. Additionally, the oxygen has a further diffusion distance, upon decomposition of Cu_2O, for thicker Cu_2O layers, which can also causes an increase in the ignition delay [164]. Thus, the ignition delay will be minimized when the O_2 diffusion distance and the laser absorption in the Cu_2O layers are optimized. Furthermore, the simulated absorption coefficients agree with the experimental trends of the ignition delay. The absorption coefficient in the Al nano layer is about 10% and relatively constant with the layer thickness. However, laser absorption is optimized with Cu_2O nano layer thickness, around 50 nm, which gives the minimum ignition delay. This correlation indicates that the first Al/Cu_2O interface reaches the ignition temperature quick due to the energy input provided by the power absorbed in the Cu_2O nano layer. There are several factors that explain the slight shift between the optimum thicknesses for the ignition delay and power absorbed: a) the surface properties such as roughness and reflective index are different in the sputtered nano laminates compared to the idealized material; b) the simulation does not consider the thin CuO surface layer on Cu_2O that forms due to oxidation [159].

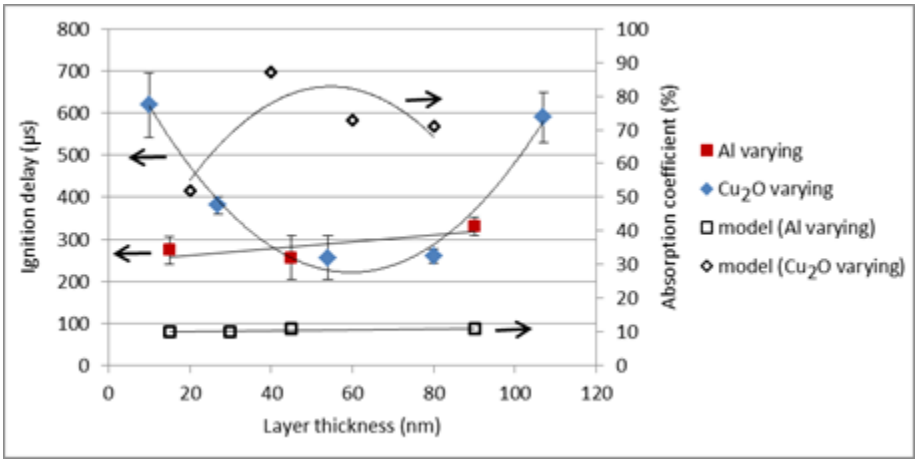

Figure 5.13: Ignition delays of Al/Cu_2O nanolaminates with layer thickness (the work was performed in collaboration with Yiqi Zhang)

The mechanism of ignition in nanolaminates is fundamentally different than surface heating/heat conduction in the layer-by-layer micro structure. The laser penetrates into the sample, and most of its energy is absorbed by the Cu_2O layer. When enough energy is absorbed, Cu_2O decomposes to its sub-oxides and O_2 gas, which reacts with the Al layer. For a constant Cu_2O layer thickness (54 nm), the ignition delay is relatively constant with Al thickness (Al/Cu_2O interface area does not change). This result indicates that laser absorption is significantly higher in the denser Cu_2O layers, which agrees with the simulated results of the absorption coefficient.

The time-averaged photodiode signal and the rate of expansion of the flame plume area, increase with the Cu_2O thickness as illustrated in Figure 5.14a (note that the ignition delay shows an opposite trend in Figure 5.13). This result suggests that the mixture stoichiometry for optimal heat release (ER = 1) is obtained for nanolaminates with Al of 45 nm and Cu_2O of around 60 nm. Also, the rate of expansion of the flame plume area is also optimized at these layer thicknesses, which is representative of maximum reaction rates. Since the apparent activation energy of the reaction is independent of the layer thickness, the enhanced reaction rates are caused by higher O_2 concentrations at the reactive interface as the Cu_2O layers reach the decomposition temperature more quickly. It should be noted that the time-averaged photodiode signal and the rate of expansion of the flame plume area are on the order of 0.01 μA/mg and 0.1 m^2/s respectively, similar to the consolidated Al/CuO pellets. Thus the sputtered nanolaminates and the mixed nano powders have similar reactivity.

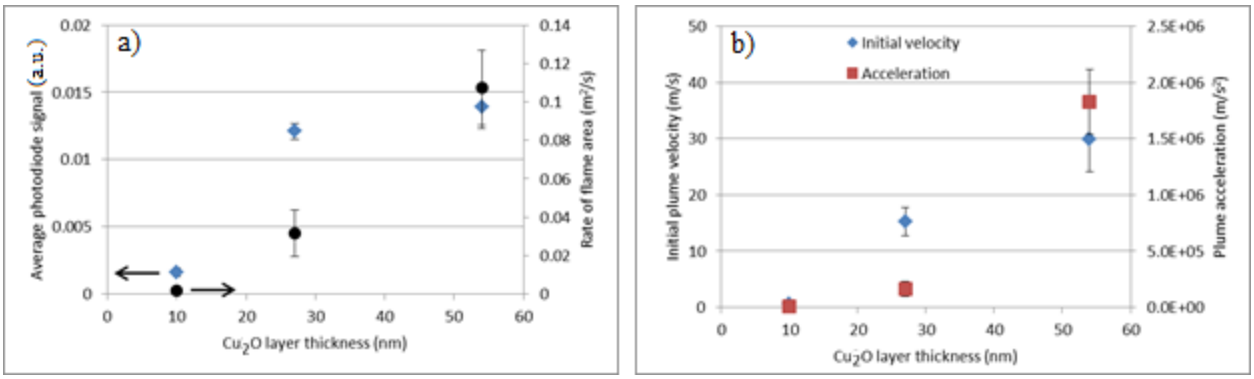

Figure 5.14: a) Reactivity of the sputtered Al/Cu_2O nanolaminates with layer thickness; b) Flame plume velocities and accelerations

Figure 5.14b shows the initial flame velocities and the average acceleration of the flame plume, which were calculated following the procedure in section 3.2.5. The initial velocity and acceleration of the flame plume are maximized for the optimum Cu_2O thickness that minimized the ignition delay. It should be noted that the combustion was not self-sustained after ignition for the nanolaminates with Cu_2O thicknesses larger than the optimal thickness. This can be explained by the large CuO mass that behaves like a heat sink for the heat of reaction, such that the next Al/Cu_2O interface does not reach the ignition temperature. Hence there are not data points displayed in Figure 5.14b.

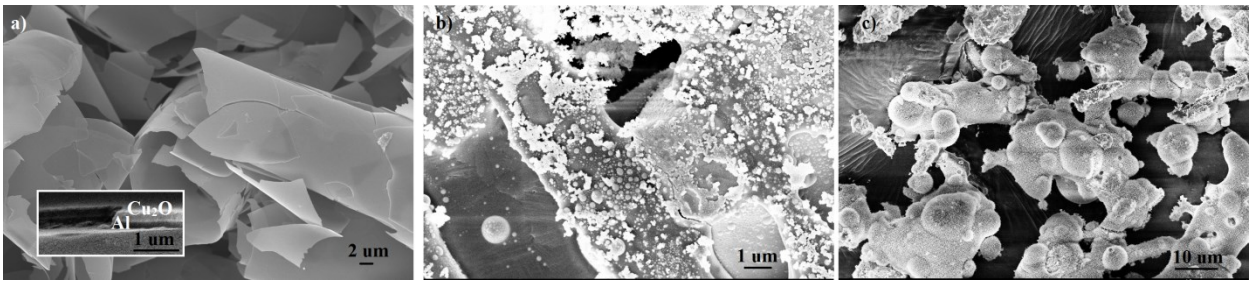

Figure 5.15: SEM images of sputtered nanolaminates, a) reactants, b) products, 27 nm Cu_2O, and c) products, 54 nm Cu_2O

An SEM image of a sputtered Al/Cu_2O nanolaminate and a typical bilayer cross section is shown in Figure 5.15a. It can be seen that the nano layers have a uniform thickness and homogeneous interface. Figures 5.15b and 5.15c show SEM images of the product morphology for nanolaminates with initial Cu_2O thicknesses of 27 nm and 54 nm, respectively. The reaction of the thinner Cu_2O nanolaminates produces Cu nanoparticles on the surface of the reacted Al_2O_3/Cu laminate. The spherical shape of the Cu nanoparticles indicates that these formed from the vapor phase. Thus the local reaction temperature was near the adiabatic flame temperature, which is close to the vaporization temperature of Cu. However, the nanolaminates with thicker Cu_2O layers indicate a more complete reaction, and higher bulk temperatures, since the Al_2O_3/Cu laminates melted. It should be noted that the product morphology shown in Figure 5.15c corresponds to the nanolaminates with the minimum ignition delay in Figure 5.13a.

5.2.6. Summary

The ignition delay in mixed nano powders (order of 1 to 100 ms) is proportional to the density and the initial rate of energy release increases with density. Condensed phase reactions play an important role on the combustion mechanism. The ignition delay in multi-layered micro structures (order of 10 to 100 ms) increases with the layer thickness, while the average and initial rate of energy release decrease with the layer thickness. Heat diffusion is an important component of the reaction mechanism. The ignition delay in sputtered nanolaminates (order of 0.1 to 1 ms) is minimized for an optimal Cu_2O thickness. The mechanism of ignition is fundamentally different than the surface heating of multi-layered structures, and there is a trade-off between laser energy absorption and oxygen diffusion.

6. Controlled oxidation and combustion of micro/nano Al particles in water

This chapter summarizes specific research on the controlled oxidation of micro and nano Al powders in water using isothermal micro-calorimetry, and the self-sustained reactions of Al powders in water under high pressure using a batch reactor. The research gap and objectives are outline first, and followed by the experimental and theoretical results.

6.1. Tunable Kinetics of Nano and Micro Aluminum Powders Reacting with Water to Produce Hydrogen

These results were published in reference [165]. The copyright permission was obtained from the journal. F. Saceleanu analyzed the experimental data and wrote the manuscript; T. Vuong set up and run the experiments; E. Master and J. Wen revised the manuscript.

6.1.1. Overview

This paper reports on the kinetics and reaction processes of 40 nm and 1 μm aluminum powders with water to produce hydrogen at atmospheric pressure. This reaction produces aluminum hydroxide with irregular morphologies as by-products. It was found that the nucleation and growth of the aluminum hydroxides affect the kinetics of the reaction and thus the hydrogen production. The heat release in isothermal micro-calorimetry and hydrogen production in a non-isothermal batch reactor were used to determine the rate-determining steps of the reaction mechanism and the corresponding activation energies. Model and model-free methods have been implemented to describe the reaction sequence between aluminum particle and water while the phase of newly produced aluminum hydroxide in the system plays an important role. The reaction of nano aluminum particles and water, being more sensitive to temperature, goes to completion to produce bayerite, $Al(OH)_3$ at 30˚C and boehmite, AlOOH at 50˚C, whereas the

micro aluminum particles do not react completely and produce only bayerite at 30 ˚C and also low amount boehmite at 50 ˚C. Nevertheless, these processes exhibit two distinct and sequential stages: a kinetically controlled stage with the apparent activation energy (E_a) of 100 to 110 kJ/mol, where nucleation and growth are limited by the chemical reactions on the surface of aluminum; and a diffusion controlled stage with E_a of 44 kJ/mol for the 40 nm Al/water reaction and 86 kJ/mol for the 1 μm Al/water reaction, where growth is limited by the mass diffusion through the aluminum hydroxide by-products. The separation of these two stages is more obvious under isothermal conditions. For non-isothermal conditions, two stages are overlapped and the one with a lower E_a dominates.

6.1.2. Objectives

Despite substantial literature work on the kinetics of Al/water reactions, there are still some unanswered questions regarding its heterogeneous mechanism and how to tune the reaction kinetics. First of all, it is well known that the morphologies of the aluminum hydroxide by-products are irregular structures such as laminates and highly porous fibers, which can be at much larger length scales than the original Al particles [86] [90]. Consequently, the nucleation and growth mechanism of these structures would be more appropriate than the core-shell model for developing reaction kinetics. However, to our best knowledge, a model describing the nucleation and growth of aluminum hydroxide and effects of its phases on the reaction mechanism is not currently available in the literature. Secondly, thanks to the formation of different phases of by-products, the heat release from the reaction is closely associated to the amount of hydrogen release. Different experiments involving varying energy release rates are therefore highly desirable to study the reaction kinetics of hydrogen generation. The goal of this work is to identify the rate-determining stages of the Al/water reaction to produce hydrogen,

using two representative length scales of Al particles (40 nm and 1 μm). These particle sizes were chosen because their active contents and specific surface areas are significantly different. Analyses based on these two particles sizes should be able to derive the representative thermo-physical properties and reaction kinetics of both nano- and micro-sized Al particles. A general heterogeneous reaction model is applied to derive the activation energy for each reaction stage and then a model-free approach is implemented to validate the experimental finding. Isothermal experiments have been performed in a micro-calorimeter, while non-isothermal experiments have been conducted in a high-pressure batch reactor. With examining the correlation between the kinetic stage and the microstructure of as-produced aluminum hydroxides, the dependence of the apparent activation energy on the progress of the Al/water reaction is investigated.

6.1.3. Experimental

Aluminum powders with aerodynamic particle sizes of 40 nm and 1 μm were purchased from US Nanomaterials Inc. The as-received Al was reacted with distilled water at an equivalence ratio of 500 (i.e. 500 times more water mass than the stoichiometric ratio). A high equivalence ratio was chosen to prevent large temperature variations around the Al powder. Two types of experiments were performed as described below.

6.1.3.1 Isothermal micro calorimetry

The isothermal experiments were performed at temperatures of 30, 40, and 50 ˚C and under the atmospheric pressure, following the procedure in section 3.1.6. Approximately 2 mg of Al powder was added the vessel, and 1 mL of pre-heated distilled water was added to the Al. The heat released by the reaction was measured relative to the same mass of distilled water in the adjacent reference vessel. The heat flow rates during the extent of reaction were used to study the kinetics of the reaction.

6.1.3.2. Non-isothermal batch reactions

The batch reactor experiments were performed using a non-stirred high pressure/temperature batch reactor, following the procedure in section 3.1.7. Approximately 100 mg of Al powder was added to the vessel, and 50 mL of distilled water was added to the Al. The temperature of the mixture was increased to 30, 40, and 50 ˚C using an external electric heater, and then turned off when the temperatures were set. After initiation, the reaction temperature increased approximately linearly. The hydrogen pressures during the reaction were used to study the kinetics of the hydrogen generation.

6.1.4. Results and discussion

6.1.4.1. Reactant and product characterization

Detailed physical and thermodynamic properties of the 40 nm and 1 μm Al powders can be found in the references [146] and [139]. Figure 6.1a shows the TGA/DSC of the reaction between the 40 nm Al powder and air at a constant heating rate of 30˚C/min, and Figure 6.1b shows the particle size distribution of this powder. The Al nano powder reacts in one exothermic step without melting due to its small particles ranging from 10 to 100 nm. Using the normal distribution, the mean particle size is 50.4 nm and standard deviation is 20.5 nm. The active content is 70% assuming that Al oxidizes fully to Al_2O_3 based on the mass increase. The remaining 30% by weight is the protective alumina layer around the nanoparticles.

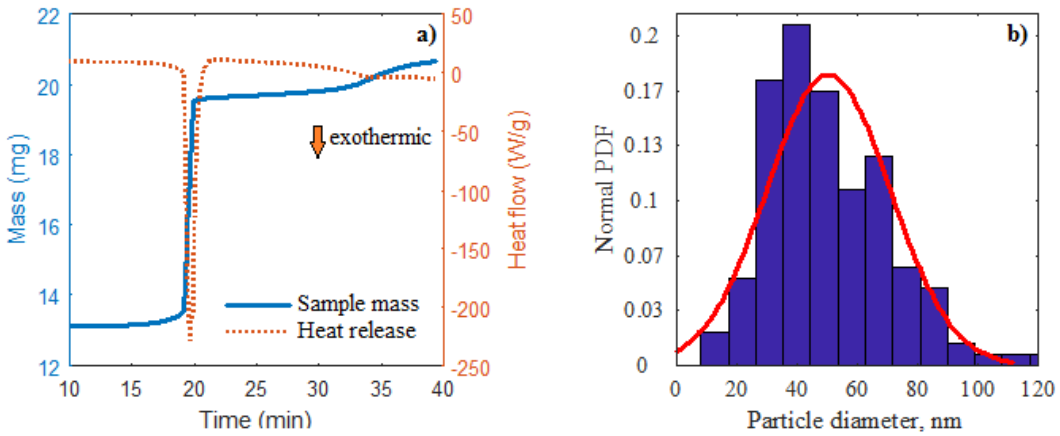

Figure 6.1: a) TGA/DSC of 40 nm Al powder and air reacting at 30 C/min; b) Particle size distribution of 40 nm Al powder

Figure 6.2a shows the TGA/DSC of the reaction between the 1 µm Al powder and air at a constant heating rate of 30˚C/min, and Figure 6.2b shows the particle size distribution of this powder. The micro powder reacts in two major steps, before and after melting. The earlier exothermic step is due to the smaller particles (order of 100 nm). Using the normal distribution, the mean particle size is 0.98 µm and standard deviation is 0.46 µm. The active content is 96% assuming that Al oxidizes fully to Al_2O_3 based on the mass increase.

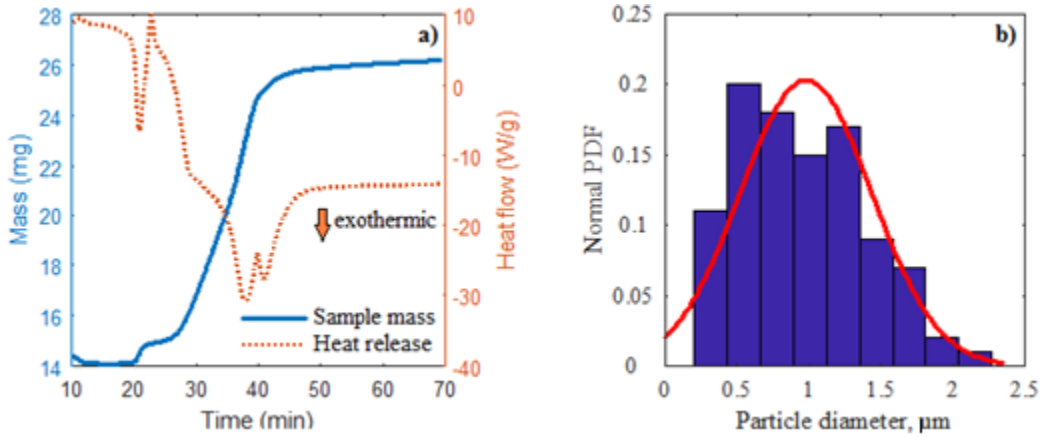

Figure 6.2: a) TGA/DSC of 1 micron Al powder and air reacting at 30 C/min; b) Particle size distribution of 1 micron Al powder

SEM images of the 40 nm Al powder and the by-products after reacting with water isothermally at 30˚C and 50˚C are shown in Figures 6.3a, 6.3b, and 6.3c, respectively. Also, XRD results of these nano structures are shown in Figures 6.3d, 6.3e and 6.3f, respectively. The as-received 40 nm particles are spherical and composed of pure Al. The protective Al_2O_3 was not detected due to its thin layer. The by-products of the nano Al/water reactions were mostly bayerite with laminate morphology and small amount of boehmite at 30˚C, and mostly boehmite with highly porous/fibrous morphology and small amount of bayerite at 50˚C. It is interesting to note that the by-products were on a much larger length scale compared to the Al nanoparticles, which suggests that the nucleation and growth of the new phase is an important component of the reaction mechanism. A standard method for determining average grain size, based on the planimetric procedure [166], was used to determine that the $Al(OH)_3$ and AlOOH grains have an effective average diameter of 900 nm and 140 nm, respectively.

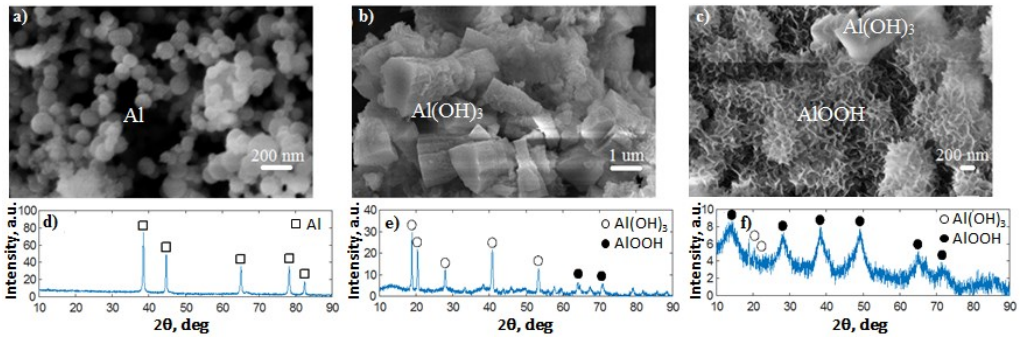

Figure 6.3: SEM images of a) 40 nm Al powder and by-products after isothermal reaction at b) 30 ˚C and c) 50 ˚C; XRD of d) 40 nm Al powder and by-products after reaction at e) 30 ˚C and f) 50 ˚C

SEM images of the 1 μm Al powder and the by-products after reacting with water isothermally at 30˚C and 50˚C are shown in Figures 6.4a, 6.4b, and 6.4c, respectively. Also, XRD results of these micro structures are shown in Figures 6.4d, 6.4e and 6.4f, respectively. The as-received 1 μm particles are spherical and composed of pure Al. The by-products of the micro Al/water

reactions were only bayerite with laminate and needle morphology and uncreated Al at 30˚C, and mostly bayerite with small amount of boehmite and unreacted Al at 50˚C. The length scale of the bayerite structures was similar to that of the 1 μm Al particles. Based on the planimetric procedure [166], the $Al(OH)_3$ and AlOOH grains have an effective average diameter of 0.55 μm and 0.18 μm, respectively. It should be noted that the fibrous AlOOH phase is fully detected in Figure 6.3c since the 40 nm Al particles were fully reacted, whereas it is only present in very small amount in Figure 6.4c on the surface of the 1 μm Al particles due to incomplete reactions. Based on classical thermodynamics, $Al(OH)_3$ is thermodynamically favourable at these low temperatures as shown by reactions R1.3 and R1.4. Hence the AlOOH formed by the nano Al particles suggests that the local temperature at the reaction interface may be higher in nano sized particles and the excess surface energy on the nanoparticle surface may be an important factor on the thermodynamic stability of the by-products.

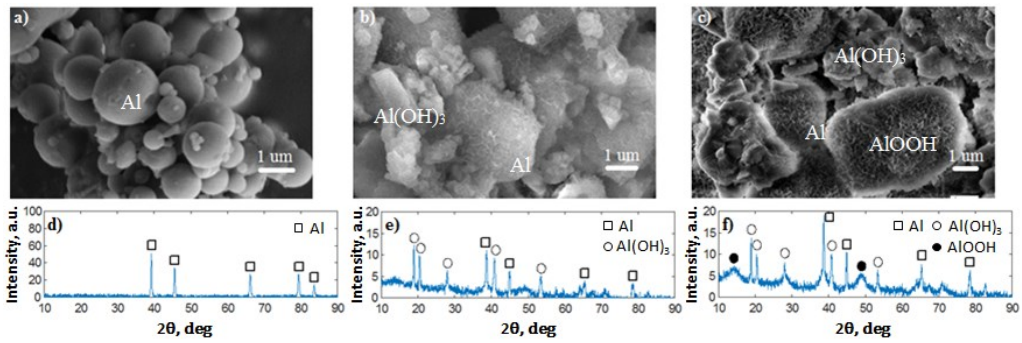

Figure 6.4: SEM images of a) 1 μm Al powder and by-products after isothermal reaction at b) 30 ˚C and c) 50 ˚C; XRD of d) 1 μm Al powder and by-products after reaction at e) 30 ˚C and f) 50 ˚C

6.1.4.2. Methodology for microstructure dependent kinetics

The Al/water reaction results from a complex heterogeneous system. Unlike homogenous reactions, the heterogeneous reactions are strongly affected by the thermodynamics, material and textural properties of reactants, surface adsorption and desorption, structural defects, diffusion

paths of reactive species, and products' morphologies, among other factors. Nevertheless, the kinetic parameters of Arrhenius equation (activation energy and frequency factor) are still valid to describe a heterogeneous reaction mechanism. Worthwhile to mention, the effective activation energy of a heterogeneous reaction is cumulative from individual reaction steps based on their contributions to the overall reaction rate. Furthermore, using the effective activation energy often under-weigh the roles of elementary steps, and the mechanism is characterized by the rate-limiting process only. The resulting kinetic parameters are apparent and dependent on the extent of the reaction (e.g. species concentration or pressure, heat flow rates, etc.). Meanwhile, it is possible to use Arrhenius equation with varying activation energy to describe the sequential thermally activated processes such as nucleation, growth and diffusion in a heterogeneous reacting system [132] [139].

Characterization of the as-received Al powders and the Al-hydroxide by-products indicated that the morphology and length scales of the by-products are very sensitive to the reaction temperature. Hence the Al/water reaction may be understood by the microstructure dependent kinetics. In this paper, the model and model-free methods were combined in order to determine and validate the reaction mechanism and the apparent activation energies. These methods are described in section 3.2.1. Specifically, the variation of E_a was derived from the model-free method, which was then used to adjust the E_a in the model based method. The algorithm is shown schematically in Figure 6.5.

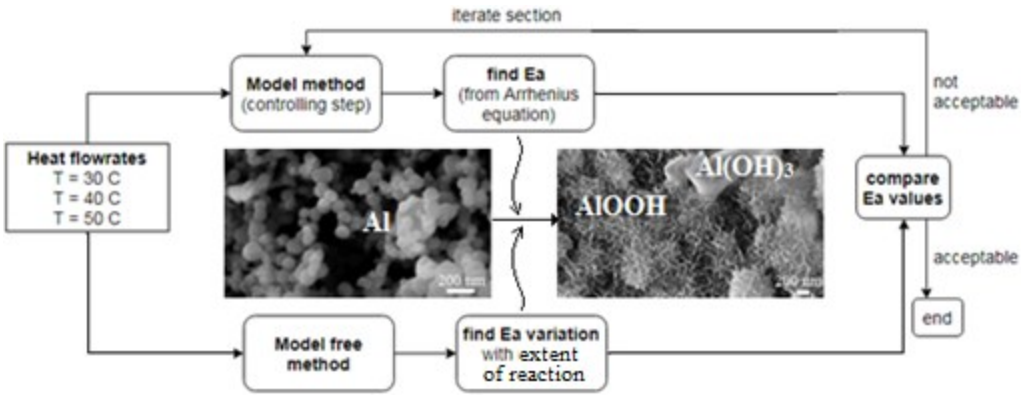

Figure 6.5: Schematic of the algorithm to determine the reaction mechanism from model and model-free methods

The heat flowrates at isothermal temperatures were used to determine the extent of reaction with time, and then Eq. 3.7 was used to find the variation of the apparent activation energy with the extent of reaction. The extent of reaction, $0 \leq \alpha \geq 1$, was split into a number of sections, dependent on the location of the heat flow maxima. Then, Eq. 3.6 was used to determine the rate-controlling steps, from the known heterogeneous reaction models in literature, which gave the best fit to the experimental data. The apparent activation energy for the rate-controlling step is determined by Eq. 3.3. It is found that the variations of both the magnitudes of E_a and the dependence of E_a on α are less than 20%, when the solutions from the model-free and model-based methods are compared. While the goal of this algorithm is to identify the major rate-controlling steps that contribute to the reaction mechanism of Al and water, a reasonable agreement between the model-free and model-based methods should be sufficient to justify the finding.

6.1.4.3. Activation energy and mechanism of the reaction

Figures 6.6a and 6.6c show the isothermal heat flow rates at 30, 40 and 50˚C for the 40 nm Al/water and the 1 μm Al/water reactions, respectively. The multiple peaks in the heat flow curve at 30˚C illustrate the multi-step nature of the reaction (note that the scale is shown on the

secondary y-axis). However, it is not possible to distinguish the contributions from individual reaction steps at 40 and 50˚C. Note that the measured heat flow per unit mass changes dramatically with temperature: from 0.1-0.5 W/g at 30˚C, to 1-13 W/g at 50˚C. With increasing temperature, a single peak in the heat flow curves can be representative of consecutive steps in the mechanism; whereas the higher rate of energy release can be representative of competitive/parallel steps in a step-wise mechanism [167]. The dependence of the heat flow on temperature also indicates that the major processes in the Al/water reaction mechanism are thermally activated. The total heat release as measured by the isothermal micro-calorimeter was 12.68, 16.01 and 14.29 kJ/g at 30, 40 and 50˚C for the 40 nm Al/water reactions, and 12.50, 15.75 and 12.74 kJ/g at 30, 40 and 50 ˚C for the 1 μm Al/water reactions. The lower heat release of the micro Al/water reactions confirms that the micron powders were not fully reacted, as determined from the XRD data. Also, the lower heat of reaction at 50˚C is due to the formation of AlOOH instead of $Al(OH)_3$, which lowers the reaction enthalpy as indicated by reactions R1.3 and R1.4.

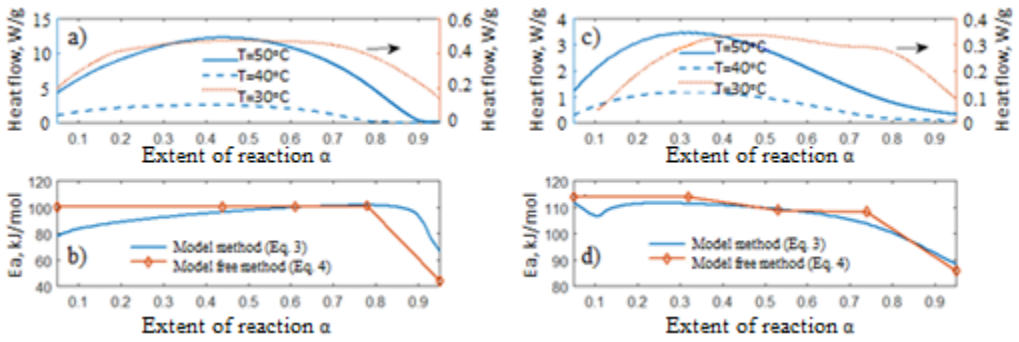

Figure 6.6: Isothermal heat flow and dependence of the apparent activation energy on the extent of reaction for: a) and b) 40 nm Al/water; and c) and d) 1 micron Al/water

The methodology described previously in the previous section was used to determine the rate-controlling stages in the reaction mechanism. The most common heterogeneous reaction models,

such as 2-dimensional and 3-dimensional diffusion, n^{th} order, interface driven, JMAK and power rate nucleation and growth, were taken into consideration [121]. Figures 6.6b and 6.6d show the progress of the apparent activation energy for the 40 nm Al/water and the 1 μm Al/water reactions, respectively. Note that with the varying phases and microstructures of the reaction by-product, the activation energy may change following the progress of the reaction [168]. The model free and model based methods illustrate a similar dependence of the apparent activation energy on the extent of reaction. There are two sequential rate-determining stages: JMAK's model of nucleation and growth and the power law model of constant nuclei growth. This result indicates that the reaction rate is controlled by the formation and nature of the by-product, aluminum hydroxide, on the surface of the Al core, from redox reactions at the Al/hydroxide interface. The $g(\alpha)$ functions for the JMAK and power law models are given in Table 3.1. It should be noted that the dominant heat and mass transfer processes that determine the growth dimensions are controlled by temperature and morphology of the by-products, among other factors.

According to the algorithm in Figure 6.5, the nucleation and growth mechanism, $g(\alpha,m)$ with a unique value of the nucleation/growth dimension m, represents the rate determining step. However, the values of m are changing along the reaction since the rate determining steps are changing according to the apparent activation energies shown in Figure 6.6. The apparent activation energies and the parameters m for the 2-stage Al/water reactions are given in Table 6.1.

Table 6.1: Rate-controlling steps and the activation energies and the nucleation and growth parameter, m, of the Al/water reaction mechanism for 40 nm Al and 1 micron Al

Stage	Controlling mechanism	40 nm Al				1 µm Al			
		E_a, *kJ/mol*	*m, 30 ˚C*	*m, 40 ˚C*	*m, 50 ˚C*	E_a, *kJ/mol*	*m, 30 ˚C*	*m, 40 ˚C*	*m, 50 ˚C*
1	JMAK	101	3.1→2.8	4.1→1.6	7.4→4.1	110	4.8→4.1	4.1→1.6	5.6→2.1
2	Power	44	0.8	0.2	0.1	86	1.3	0.3	0.4

The first stage is controlled by JMAK's nucleation and growth; the activation energies are 101 and 110 kJ/mol for the 40 nm Al/water and 1 µm Al/water reactions, respectively. Initially, the 3-dimensional growth of the aluminum hydroxides occurs simultaneously with random nucleation (hence $m > 3$). However, the morphology of the by-product with time also impedes the sites for nucleation and creates geometrical constraints, which subsequently restrains the growth to a 1- and 2-dimensional process ($1 < m < 2$). It should be noted that m also changes with temperature, since there is larger percentage of available nucleation sites at the higher temperature. The values of $m > 1$ indicate that the initial reaction between Al and water is kinetically controlled redox reactions on the surface of the Al core. Any of the reactions R1.3 through R1.5 may occur at this stage, depending on the local reaction temperature. The second stage is controlled by the power law model of constant nuclei growth; the activation energies are of 44 and 86 kJ/mol for the 40 nm Al/water and 1 µm Al/water reactions, respectively. At this stage, the reaction rate is limited by the mass transport of the soluble molecules and ions through the well-developed Al-hydroxides. The values of $m < 1$ indicate that the Al/water reaction becomes limited by mass diffusion. It should be noted that the nano Al particles have lower activation energies in both stages due to their high specific surface area and surface energy which lower the energy barrier for nucleation and growth. Also, E_a is much lower in the second stage due to the reduced rate of formation of the aluminum hydroxides. This is shown by the decreasing heat flow rates in Figures 6.6a and 6.6c. Theoretically, it can be shown that activation energy decreases with the

extent of reaction in consecutive chemical reactions where the activation energy of the first reaction is higher [168], as well as in chemical reactions complicated by mass diffusion [169]. Similarly, the Al/water system exhibits a chemical reaction mechanism complicated by mass diffusion: the nucleation and growth of the aluminum hydroxide by-products is first controlled by the redox reactions, and then by the mass diffusion of the ions in water through the by-products.

It has been shown that the nucleation and growth mechanism of the Al/water reaction provides a better fit to the experimental data compared to the core-shell model [165]. The microstructure dependent reaction mechanism between Al and water that generated AlOOH by-product is shown schematically in Figure 6.7. It should be noted that although the laminated $Al(OH)_3$ phase forms at the lower temperatures, the reaction mechanism is similar. In the first stage, the by-products form outside the spherical Al particles due to the redox reactions that oxidize the Al and reduce H_2O. This kinetically controlled stage can be modelled by the JMAK nucleation and growth with a higher E_a of around 100 kJ/mol and a decreasing parameter *m* due to the increasing diffusion resistance of the by-products. In the second stage, the reaction is controlled by the diffusion of OH^- and H_2O through the by-products, and can be modelled by the power law growth with a lower E_a of around 50 kJ/mol and a parameter *m* less than one.

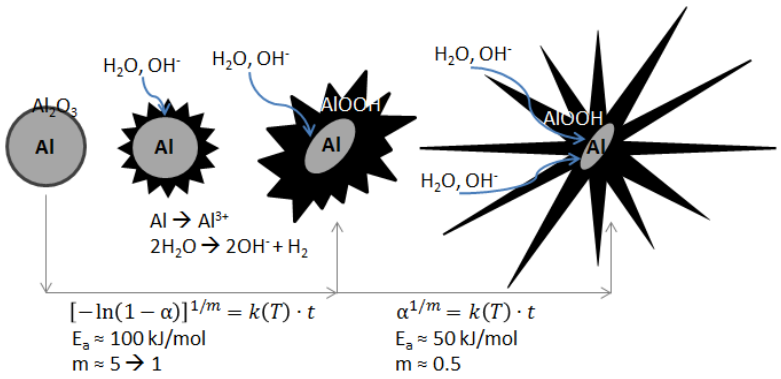

Figure 6.7: Schematic of the microstructure dependent reaction mechanism between Al and water

6.1.4.4. Kinetics of hydrogen release

The kinetics of hydrogen release from the Al/water reactions is determined from the non-isothermal batch reactor experiments as described in section 3.1.7. These experiments are representative of large scale applications for H_2 production from Al/water, since a high temperature can enhance the kinetics of the reaction. Hydrogen pressure and the extent of reaction were calculated from the ideal gas law as shown in section 3.2.6.

Figures 6.8a and 6.8c show the hydrogen pressure generated by the 40 nm Al/water and 1 μm Al/water reactions, respectively. The higher rates of hydrogen release when using nano sized Al particles can be attributed to the higher specific surface area available for reaction. Also, the rates of hydrogen release increase with the higher set temperature, which is an expected result for thermally activated processes. It should be noted that the heating rate of the mixture inside the batch reactor was approximately linear after initiation, and controlled by the reactor set temperature (i.e. a lower set temperature resulted in a lower heating rate). These heating rates were used to estimate the apparent activation energies.

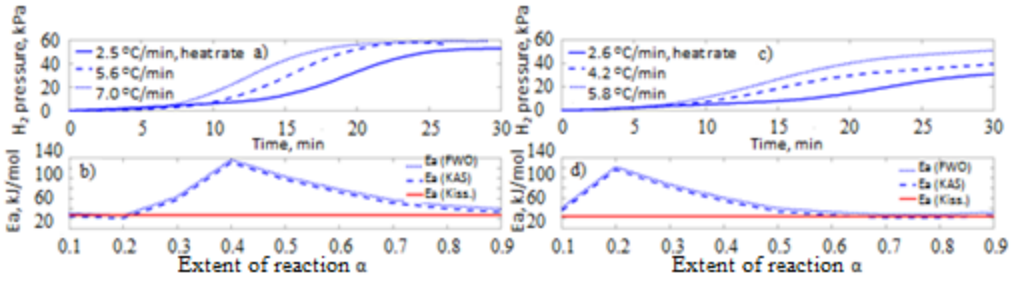

Figure 6.8: Hydrogen pressure and dependence of the activation energy on the extent of reaction in the batch reactor, for a) and b) 40 nm/water; and c) and d) 1 micron Al/water

Figures 6.8b and 6.8d show the progress of the activation energies for the 40 nm Al/water and 1 μm Al/water reactions, respectively. The apparent activation energies calculated by the model free methods increased then decreased with the extent of reaction from approximately 120 kJ/mol to 20 kJ/mol. However, the final E_a values are similar to those obtained by the Kissinger method. This can be explained mathematically by the Arrhenius kinetics where the reaction rates increase faster with temperature for processes with the higher E_a. Hence in the self-sustained Al/water reaction mechanism, the steps with higher E_a steps are overshadowed by the steps with lower E_a. It should be noted that the dependence of E_a with the extent of reaction resembles the 2-stage nucleation and growth mechanism determined for the isothermal reactions in Table 6.1. For comparison, E_a was found to be 41 kJ/mol and independent of the Al particle size [22], and about 65 kJ/mol for small Al particles (100 nm to 1 μm) [87].

The kinetics of hydrogen release from the batch reactions and kinetics of heat release from the isothermal calorimetry show similar dependence of the apparent activation energy with the extent of reaction. This indicates that the nucleation and growth stages described in section 6.1.4.3 are fundamental stages in the Al/water reaction mechanism. However, the transition of E_a with the extent of reaction, from kinetic to diffusion controlled processes, is not identical for the different types of experiments. Certain processes such as adsorption and desorption will only

contribute to the isothermal heat release data. On the other hand, the non-isothermal batch reactions may go through larger temperature variations that result in larger contributions of the elementary steps to E_a compared to the isothermal reactions. Furthermore, the pressure increase in the batch reactor affects the kinetics of the reaction since it increases the critical H_2 pressure which is required to break the hydrated alumina film and sustains the reaction [107].

6.1.5. Summary

The kinetic mechanism and reaction processes of nano and micro aluminum particles and water to produce hydrogen were studied using isothermal calorimetry and non-isothermal batch reactions at atmospheric pressure and moderate temperatures. The 40 nm Al/water reactions were very sensitive to temperature and reacted completely to produce bayerite with low amount of boehmite at 30˚C and boehmite at 50˚C. The 1 μm Al/water reactions did not go to completion at these temperatures and produced bayerite at 30 ˚C and bayerite with low amount of boehmite at 50 ˚C. The heterogeneous reaction mechanism is driven by the nucleation and growth of the aluminum hydroxide by-products. There are two rate-determining stages. The first stage is controlled by redox reactions at the aluminum/ hydroxide interface with the apparent activation energy of 100-110 kJ/mol. Random nucleation and unrestricted phase growth occur simultaneously. The second stage is controlled by mass transport through the by-product layers with the apparent activation energy of 44 kJ/mol and 86 kJ/mol for the 40 nm Al/water and 1 μm Al/water reactions, respectively. The phase growth is restricted by the morphology of the by-products. These activation energies were validated by correlating the model and model-free methods. These stages are also apparent in the non-isothermal batch reactions, where the apparent activation energies for hydrogen production are similar to the heat flow rates under isothermal conditions.

6.2. Kinetics of Self-Sustained Aluminum/Water Reactions under High Pressure

This is unpublished material. A manuscript on the results in this section, supported by the batch reactor model in section 3.2.6, will be submitted to a journal.

6.2.1. Overview

The kinetics of Al/water reactions in distilled water, sodium hydroxide (NaOH) solution and catalyzed by Al-hydroxide byproducts, are characterized under high argon pressure by estimating the respective apparent activation energies. It is found that E_a for initiating the reaction of the 5 μm Al powders is 35 kJ/mol and irrespective of the media conditions. The peak hydrogen generation is kinetically controlled on the surface of the Al particle with the apparent activation energy of 75 kJ/mol, which is independent of the particle size for 500 nm, 1, 5 and 10 μm diameters of the Al particles. The NaOH solution and Al-hydroxide byproducts are effective in reducing the energy barrier of the reaction. The reactivity of Al/water reactions creates significant pressure and temperatures overshoots inside the batch reactor. Catalysis is required for commercial applications and hydrogen generation on timescales of one minute.

6.2.2. Objectives

Hydrogen generation from Al/water reactions should occur on a seconds to minutes timescale for any commercial applications such as power generation or fuel cells. This requires higher reaction temperatures under high pressures to prevent water from boiling. Furthermore, the addition of catalysts enhances the reaction rate. This study investigates the reaction kinetics and timescales of hydrogen generation for self-sustained Al/water reactions in a batch reactor under argon at high pressure (1000 psi gauge). The catalytic effects of Al-hydroxide byproducts and NaOH solution on the apparent activation energy of the reaction are investigated.

6.2.3. Experimental

The batch reactor experiments were performed using a non-stirred high pressure/temperature batch reactor, following the procedure in section 3.1.7. Two types of experiments were performed:

a) study the effect of Al particle size, by mixing 10g of 500 nm, 1, 5 and 10 μm Al powder with 20 mL of distilled water (equivalence ratio of 2);

b) study the catalytic effects, by mixing 3.5g of 5 μm Al powder with Al-hydroxide byproduct (mass ratio of 1 to 0.6) and distilled water (equivalence ratios of 3, 6 and 10), and mixing 3.5 g of 5 μm Al powder with 0.275 M NaOH solution (equivalence ratios of 3, 6 and 10)

The temperature of the mixture was increased to 90˚C using an external electric heater, and then turned off after this set temperature. The reactions initiate prior to reaching the set temperature. The hydrogen pressures during the reaction were used to study the kinetics of the hydrogen generation.

6.2.4. Results and discussion

The Al/water reactions are thermally activated processes. This means that the kinetic parameters such as the apparent activation energy and frequency factor can be quantified by varying the heating rate before the reaction initiates. Figure 6.9 shows the total pressure (argon and hydrogen) and reaction temperature of 5 μm Al/water reactions for 3 different equivalence ratios. The aluminum mass is 3.5g and the water mass is varied accordingly. The slopes of the temperature and pressure curves indicate that heating and pressurization rates are significantly different. The heating rate prior to initiation can be assumed to be approximately linear and controlled by the high specific heat capacity of water. This assumption was validated by

determining that the heat capacity of the mixture (Eq. 3.33) between 25 ˚C and the initiation temperature varies by less than 5%.

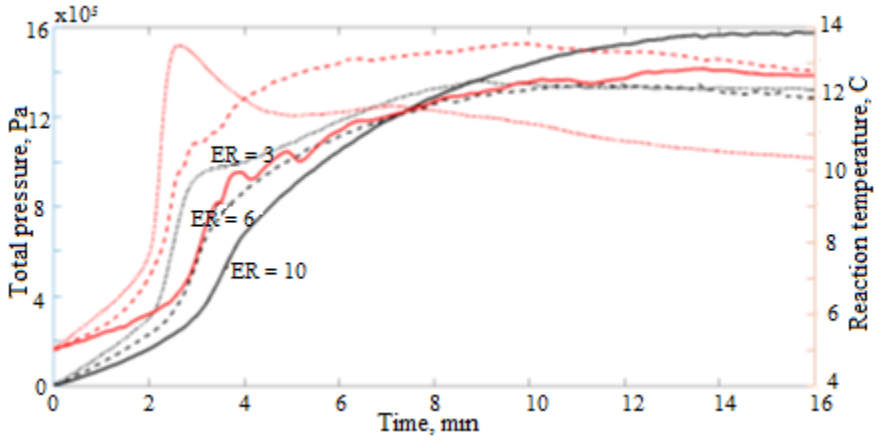

Figure 6.9: Total pressure and reaction temperature of 5 micron Al/water reaction for 3 different equivalence ratios

The ignition of self-sustained exothermic reactions occurs at the temperature T_i, such that $d^2T_i/dt^2 = 0$. This is the classical method, which equates the magnitudes and rates of the heat release and the heat losses. Using the isoconversion method based on Eq. 3.8, the apparent activation energy for initiation is estimated to be 35 kJ/mol for the Al/water and catalyzed Al/water reactions. This result indicates that initiation is controlled by the diffusive transport of water or OH^- species across the native alumina shell (i.e. hydration).

Figure 6.10 shows the total pressure and reaction temperature of 5 μm Al/water reactions in NaOH solution and with Al-hydroxide catalysis (ER = 10). It can be seen that the hydrogen rates are improved when the reaction occurs in NaOH solution or catalyzed using Al-hydroxide byproduct. The reaction kinetics are enhanced since water dissociates faster on the surface of the Al-hydroxide [107], and the OH^- ions in NaOH dissolves the alumina layer [97] [170]. The key to maintaining higher reaction rates in Al/water is to continuously disrupt the alumina layer that forms a barrier for diffusion of water to the aluminum core.

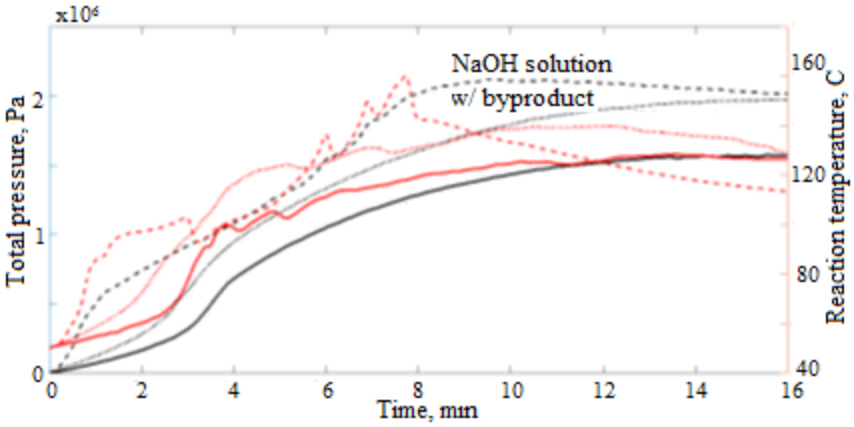

Figure 6.10: Total pressure and reaction temperature of 5 micron Al/water reaction with catalysis (ER = 10)

It is assumed that the reactions are controlled kinetically on the surface of the aluminum core around the temperature that generates the highest pressure rates. At this temperature, the surface of aluminum is saturated by the oxidizing species (i.e. 0 order). The apparent activation energy is estimated using the rate constant given by the Arrhenius equation in Eq. 3.4. The E_a values under this condition are ~ 22 kJ/mol for Al/water and ~ 16 kJ/mol for Al reaction in NaOH solution or Al/water catalyzed by Al-hydroxide. The reduced E_a indicates that NaOH and Al-hydroxide are effective in reducing the energy barrier of the reaction. The timescale of the reactions for the equivalence ratios of 3, 6 and 10 is approximately 10 min, as shown in Figures 6.9 and 6.10.

The procedure described above was used to determine the apparent activation energy of the Al/water reactions for different Al particle diameters (500 nm, 1, 5 and 10 μm). However, the maximum pressure rates were normalized by the surface area of the particle. Figure 6.11 illustrates that the effective apparent activation energy of the reactions is approximately 75 kJ/mol and independent of the particle size. This indicates that the reactivity of the smaller sizes Al particles scales with the specific surface area.

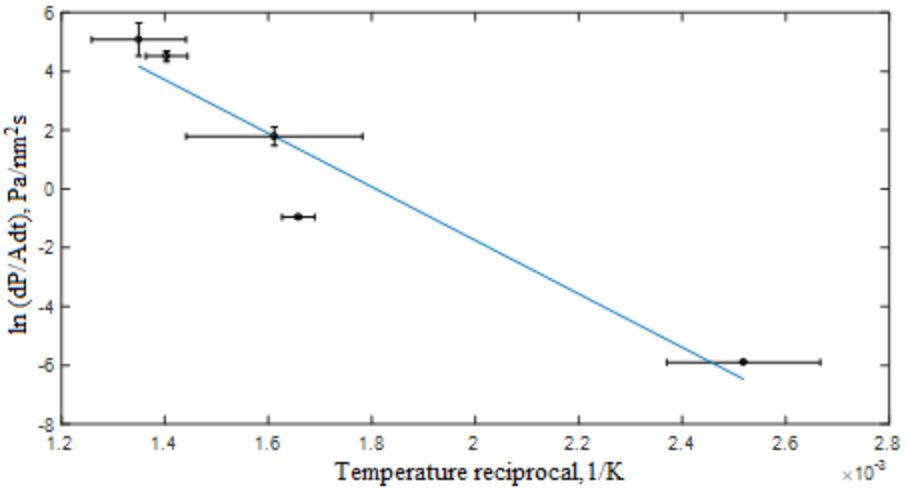

Figure 6.11: Effective activation energy of Al/water reactions at maximum rate of hydrogen production using the isoconversion method

Hydrogen can be generated faster from Al/water reactions at lower equivalence ratios. Figure 6.12 shows an example of the total gauge pressure and reaction temperature profiles of the commercial spherical Al/water and catalyzed 5 μm (grainy) Al/water reactions for an equivalence ratio of 1.5 and argon pressure of 800 psig. The catalyst was provided by Cleanwave Energy Corp. (a Waterloo based company) without any details due to its patent status. The premixed Al/catalyst powder included 10% catalyst by mass. As noted in Figure 6.12, the commercial Al powders initiate faster due to the spherical morphology that optimizes the contact area between the fuel and the oxidizer. However, the catalyzed Al powder is significantly more reactive and exothermic once initiated, as noted by the higher pressure and temperature rates. It should be noted that under the conditions above, there were significant pressure or temperature overshoots, owing to the fast exothermic reaction and hydrogen release.

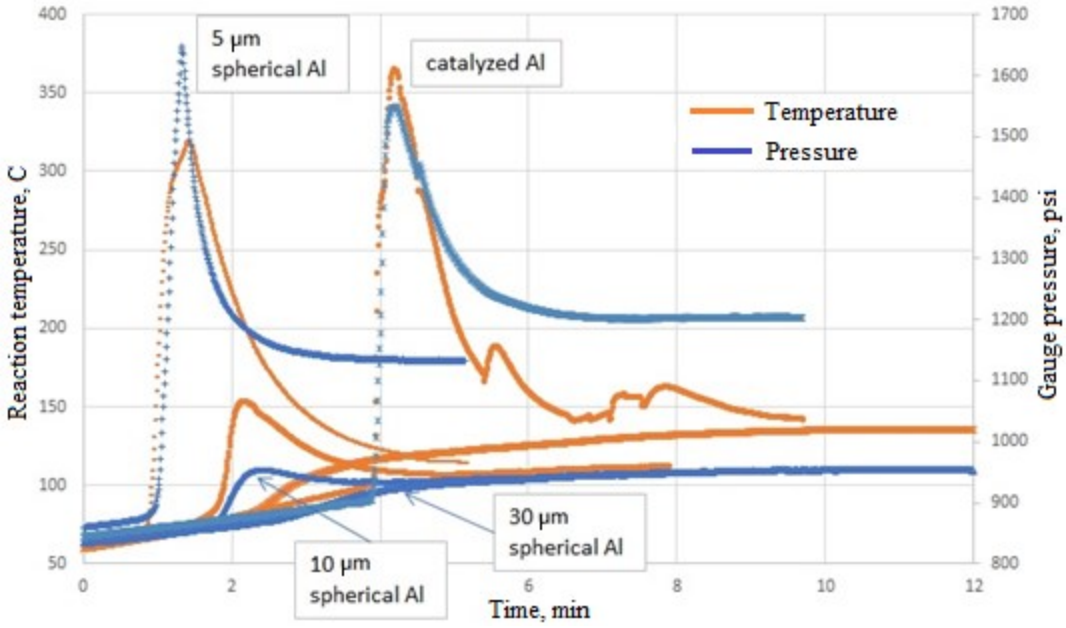

Figure 6.12: Gauge pressure and reaction temperature of the commercial and catalyzed Al/water reactions (ER = 1.5 and P_{argon} = 800 psig)

Table 6.2 compares the rate of pressurization and the hydrogen gas pressure at the final equilibrium temperature. It can be seen that the catalyzed Al powder has significantly higher rates of hydrogen release and improved yields. Theoretically, this can be attributed to the catalyst around the Al particles, whose role is to lower the energy barrier for the reaction and hence enhance the reaction rates.

Table 6.2: Pressure rate and hydrogen gas pressure of the commercial Al/water and catalyzed Al/water reactions

	P_{argon} = 800 psi		P_{argon} = 1200 psi	
Al powder type	**dP/dt (psi/min·g)**	**P_{H2} (psi/g)**	**dP/dt (psi/min·g)**	**P_{H2} (psi/g)**
30 µm spherical	2.9	16	4.4	9.4
10 µm spherical	32	17.5	10	16
5 µm spherical	333	39	377	28
5 µm grainy (catalyzed)	566	57	522	54

6.2.5. Summary

The Al/water reactions are highly reactive inside a batch reactor at low equivalence ratios (i.e. ER = 1.5). These reactions should be catalyzed in order to decrease the timescale of hydrogen generation. It was found that the apparent activation energy for initiating the reaction is 35 kJ/mol, and irrespective of the media conditions. Furthermore, the chemical reactions are driven kinetically on the surface of the Al particle at the peak rate of hydrogen generation. The apparent activation energy at this condition is 75 kJ/mol and independent of the particle size of aluminum.

7. Conclusions and Future work

7.1 Conclusions

The major conclusions from this research are listed below. These conclusions are based on the results in sections 4, 5 and 6.

Aluminum-oxygen reactions (solid-gas):

- Simultaneous oxidation and phase transformations in Al particles are driven by the crystallization of the Al_2O_3 shell
- The apparent activation energy, E_a, of O_2 and Al diffusion through the Al_2O_3 shell is much higher than the E_a of the chemical reaction
- Nano Al particles oxidize at a faster rate and at lower temperatures compared to micro Al particles
- The effective Knudsen diffusion of O_2 through a consolidated Al nanoparticle pellet drives the reaction front

Aluminum-copper oxide reactions (solid-solid):

- Fast laser heating creates material ablation on the surface of consolidated Al/CuO nanoparticle pellets, followed by edge ignition
- The combustion mechanism in consolidated Al/CuO nanoparticle pellets changes from mass convection to heat conduction with increasing the pellet density, while the speed of the reaction front decreases from the order of 100 m/s to 1 m/s
- The ignition mechanism of consolidated Al/CuO nanoparticle pellets is driven by heat transfer on the surface; on the other hand, the ignition mechanism of sputtered Al/Cu_2O nanolaminates is driven by the laser absorption into the Cu_2O layer

Aluminum-water reactions (solid-liquid):

- The kinetics of the Al/water reaction are driven by the nucleation and growth of the aluminum hydroxide by-products
- The mechanism of reaction follows two sequential stages: kinetically controlled chemical reactions on the Al surface, and mass diffusion controlled through the by-product
- The apparent activation energy of this reaction is lower in nano Al powders compared to micro Al powders
- The apparent activation energy for initiation and maximum rate of hydrogen release under high pressure is independent of the Al particle size

Table 7.1 below summarizes the major procedure and findings of the research in this thesis, from the microstructure of the aluminum materials, to the experimental setups that initiate and monitor the reactions, and the major contributions on the reaction mechanisms based on the experimental and theoretical results.

Table 7.1: Summary of the research in this thesis

Heterogeneous reactions	Al – O_2 (solid-gas)	Al – CuO (solid-solid)	Al – H_2O (solid-liquid)
Microstructure	a) Spherical particles (40 nm,1 μm) b) Consolidated pellets	a) Consolidated pellets (40–40 nm) b) Sputtered nanolaminates	Spherical particles (40, 500 nm, 1, 5, 10 μm)
Initiation	a) Oxidation under low heating rate in TGA/DSC b) Ignition under fast heating rate using laser	Ignition under fast heating rate using laser	a) Oxidation using isothermal micro-calorimetry b) Ignition under low heating rate in batch reactor
Reaction mechanism	a) Simultaneous phase transformations and gas-solid kinetics b) Oxygen diffusion in porous pellet	a) Transition from mass convection to heat diffusion b) Laser absorption and oxygen diffusion	Nucleation and growth of the by-product

7.2 Future work and recommendations

Potential applications of the reactions between Al powders and metal or liquid oxidizers should be investigated. In particular, the suitability of Al/CuO thermites in propulsion and Al/water

mixtures for hydrogen production can be studied using the apparatus setups in sections 3.1.5 and 3.1.7. The short ignition delay and fast gas generation of the Al/CuO reaction may find suitable for small scale thrusters. The tunable kinetics and portability of the Al/water mixtures are suitable for on-demand hydrogen generation. The following subsections summarize recommendations for the future work on Al/CuO and Al/water reactions.

7.2.1 Al/CuO thermites for small scale propulsion

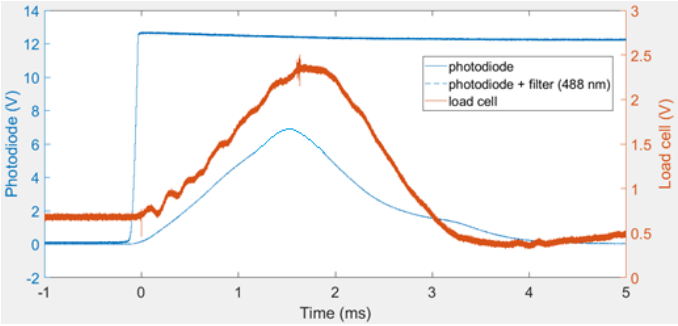

Figure 7.1: Photodiode and load cell data during the combustion of a 50% TMD Al/CuO nanothermite (the work was performed in collaboration with Alex Baranovsky)

The consolidated Al/CuO nanothermite pellets can be integrated in acrylic tubes using the laser ignition with high speed imaging setup in section 3.1.5, in order to study the thrust and specific impulse. Related research can be found in rerefences [171] [172]. Figure 7.1 illustrates the load cell and photodiode data during the combustion of an Al/CuO nanothermite (40 nm Al and CuO powders, ER = 1.5, mass = 130 mg, 50% TMD) under atmospheric conditions. The filtered photodiode indicates that the duration of burn correlates well with the duration of thrust; however, the unfiltered photodiode shows much longer burn duration due to reactions of Al nanoparticles/clusters with oxygen in air. This result shows the importance of studying the combustion of Al/CuO thermites under inert conditions, or under vacuum for space applications of this reaction.

Figure 7.2 illustrates the force profiles and snapshots during the combustion of Al/CuO nano and micro thermites under various configurations: no nozzle and converging-diverging (CD) nozzle (mass = 100 mg, ER = 1.5). The engine and nozzle were developed by the undergraduate

students for the 4th year project. The force profiles in Figure 7.2 indicate that the 40 nm Al/CuO thermite generated higher thrust forces over a shorter duration compared to the 1 μm Al/CuO thermites. On the other hand, the CD nozzle produced less thrust over a longer duration compared to the no-nozzle case. This can be explained by the large Cu and Al_2O_3 product agglomerates that impede the gas flow, which is magnified by the converting part of the nozzle.

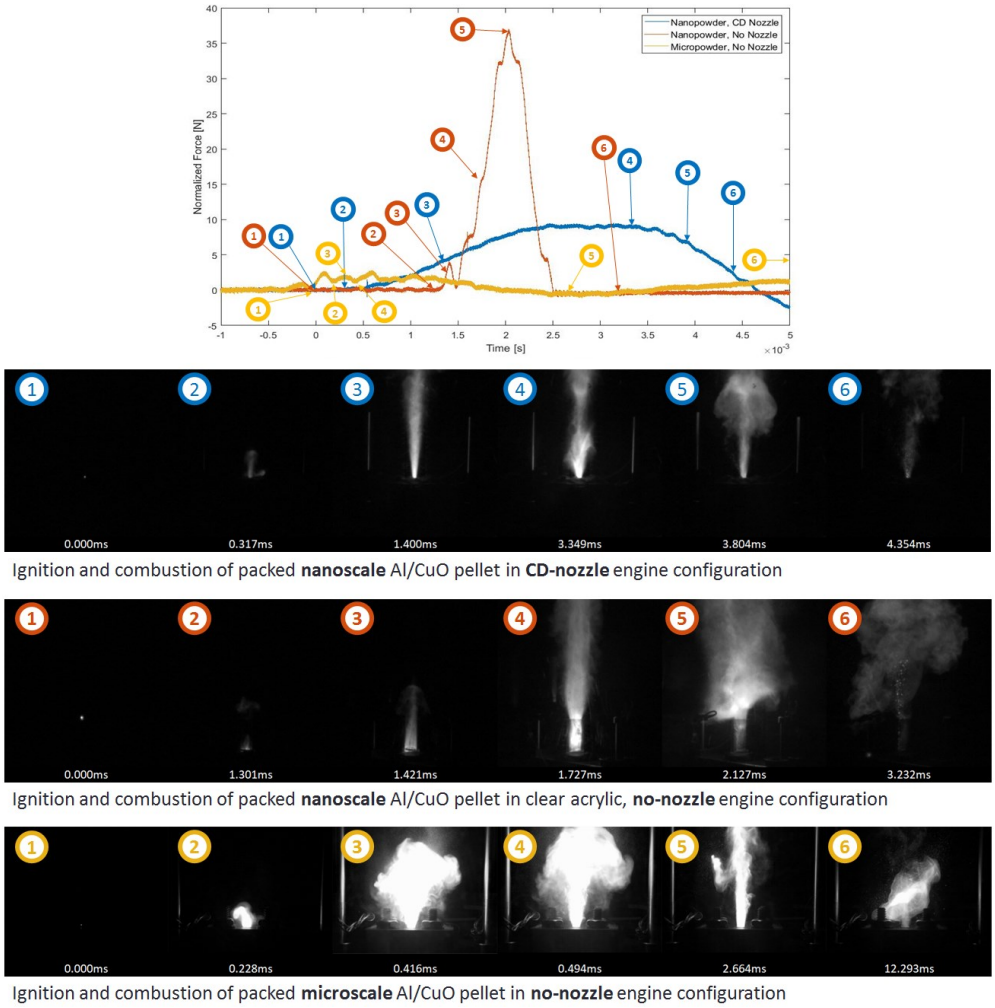

Figure 7.2: Force profiles and snapshots of the Al/CuO nano and micro thermites under various configurations (the work was performed in collaboration with Alex Baranovsky)

Additional experiments should be performed to obtain the force profiles and measure the specific impulse of these reactions, and relate the packing density (%TMD) to the peak thrust, burning

speeds and durations. These measurements can be incorporated in the theoretical framework in section 3.2.4 to estimate the burning speed through the porous Al/CuO pellet. In addition, ignitions under high vacuum should be investigated since these are representative of the atmosphere in space.

7.2.2 Al/water mixtures for on-demand hydrogen generation

The kinetics of Al/water mixtures under high pressure can be studied further using the experimental setup in section 3.1.7 along with the batch reactor model described in section 3.2.6. The reaction mechanism of these self-sustained Al/water reactions can be studied from two different points of view: a) kinetics of the heat release; and b) kinetics of the hydrogen gas release.

Figure 7.3 shows an example of the reaction and gas temperatures, and the total gas pressure of 3.5g of 5 μm Al powder mixed with 0.275 M NaOH solution at an equivalence ratio of 3 (initial argon pressure was 1000 psi). It can be seen the reaction and gas temperatures are in thermal non-equilibrium during the reaction. It should be noted that in this specific case, the large temperature difference are caused by the enhanced kinetics of the reaction in NaOH solution. Temperature differences are up to 80˚C for the reactions of Al powders in distilled water. It is interesting to note that the reaction temperature and pressure rates have different profiles, owing to the kinetics of heat release and hydrogen gas release, respectively.

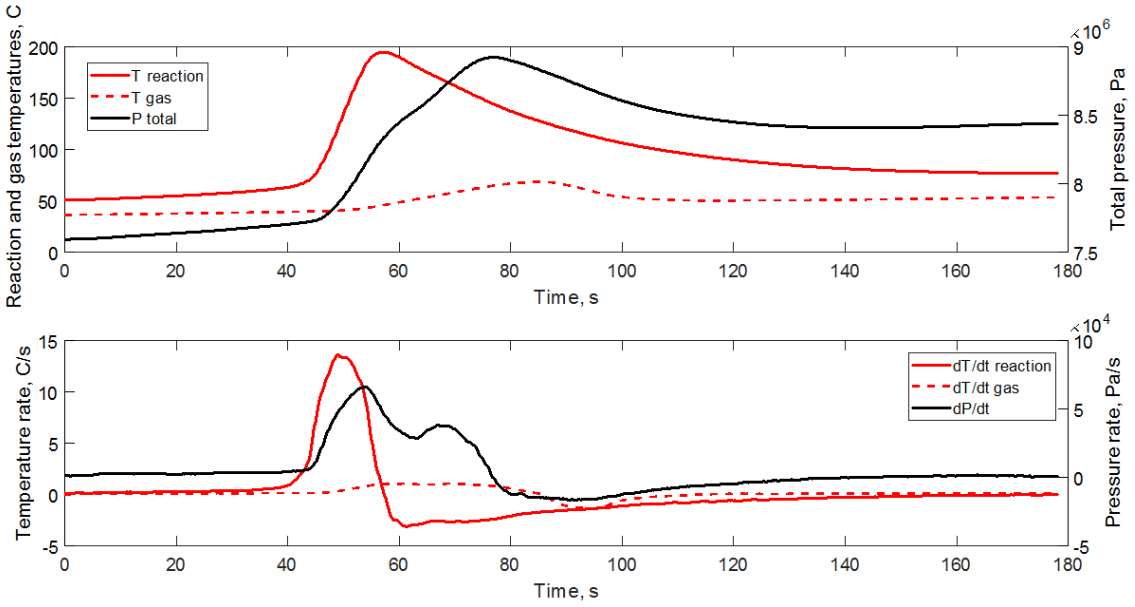

Figure 7.3: Reaction and gas temperatures, and total gas pressure of the Al/water reaction (3.5g of 5 micron Al, ER = 3)

Figure 7.4 shows the reaction rates based on the kinetics of heat release and the kinetics of hydrogen gas release, calculated from the theoretical model in section 3.2.6. The general profiles of the reaction rate with the extent of the reaction are similar. However, the kinetics of hydrogen generation indicates higher complexity given the more complex profile. Furthermore, it was found that the 2-stage sequential mechanism found at moderate isothermal temperatures in section 6.1.4.3 is not applicable to the high pressure/temperature batch reactions. Instead, the mechanism can be estimated based on the model fitting the reaction rate with extent of reaction based on parallel and/or sequential reaction steps, using the general reaction model in section 3.2.1. The rate-determining steps in the mechanism should follow the shape of the curves in Figure 7.4.

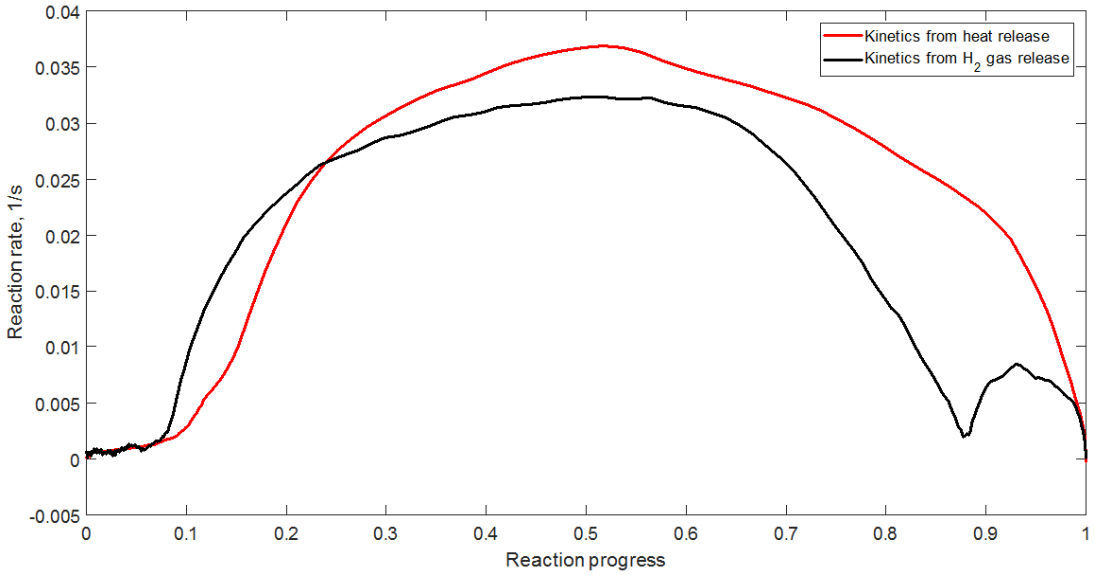

Figure 7.4: Reaction kinetics of Al/water based on heat release and hydrogen gas release (3.5g of 5 micron Al, ER = 3)

The example shown in Figures 7.3 and 7.4 illustrates the importance of understanding the heat release from the reaction on generating hydrogen. The kinetics should be understood well in order to improve the hydrogen generation rates and yield for commercial applications of on-demand hydrogen production.

7.2.3 Comments on studies on oxidation/ignition of single Al nano or micro-particle

The nano and micro Al powders used in the experiments of this research are polydisperse as shown in the SEM images and the particle size distributions. The particle size is particularly important at the nano scale since the active Al content reduces significantly and the specific surface energy increases significantly for particle diameters below 50 nm. Experimentally, the reactivity of single Al particles can be studied using apparatus such as transmission electron microscopy (TEM) with specially designed sample holders that allow for fast electric heating [28] or environmental transmission electron microscopy (ETEM) [173]. Such real-time observations of a single particle can be used to estimate the reaction kinetics of a single particle.

However, the kinetics of a reaction involving polydisperse Al powders can separate into distinct stages, as shown in the TGA/DSC graphs of the 40-60 nm Al powders. The intrinsic reactions can be different for powder mixtures due to the additional heat and mass transfer within the particle bed. Yet the application of metal aluminum for heat generation, propulsion and hydrogen generation involve powder mixtures with wide particle size distributions. Hence the experimental results on the reactivity of polydisperse powders are important for the potential application.

Bibliography

[1] D. Sundaram, V. Yang and R. A. Yetter, "Metal-based nanoenergetic materials: Synthesis, properties, and applications," *Progress Energ. Comb. Science,* vol. 61, pp. 293-365, 2017.

[2] S. W. Chung, E. A. Guliants, C. E. Bunker, P. A. Jelliss and S. W. Buckner, "Size-dependent nanoparticle reaction enthalpy: oxidation of aluminum nanoparticles," *J. Phys. Chem. Solids,* pp. 719-724, 2011.

[3] I. Glassman, Combustion, 3rd ed., San Diego: Academic Press, 1996.

[4] S. Chowdhury, *Probing the Ignition Mechanism of Aluminum Nanothermites (Doctoral Dissertation),* Faculty of the Graduate School of the University of Maryland, 2012.

[5] J. G. Granier, *Combustion Characteristics of Al Nanoparticles and Nanocomposite Al+MoO3 Thermites (Doctoral Dissertation),* Graduate Faculty of Texas Tech University, 2005.

[6] A. A. Gromov and U. Teipel, Metal Nanopowders: Production, Characterization, and Energetic Applications, John Wiley & Sons, 2014.

[7] D. S. Sundaram, V. Yang and V. E. Zarko, "Combustion of Nano Aluminum Particles (Review)," *Combust. Explo. Shock+,* vol. 51, pp. 173-196, 2015.

[8] O. B. Nazarenko, Y. A. Amelkovich and A. I. Sechin, "Characterization of aluminum nanopowders after long-term storage," *Appl. Surf. Sci.,* vol. 321, pp. 475-480, 2014.

[9] S. H. Fischer and M. C. Grubelich, "Theoretical Energy Release of Thermite, Intermetallics, and Combustible Metals," Sandia National Labs, Albuquerque, NM, US, 1998.

[10] R. A. Yetter, A. R. Grant and F. S. Steven, "Metal particle combustion and nanotechnology," *Proceedings of the Combustion Institute,* vol. 32, pp. 1819-1838, 2009.

[11] G. Jian, S. Chowdhury, K. Sullivan and M. R. Zachariah, "Nanothermite reactions: Is gas phase oxygen generation from the oxygen carrier an essential prerequisite to ignition?," *Comb. Flame,* vol. 160, pp. 432-437, 2013.

[12] M. R. Weismiller, J. Y. Malchi, J. G. Lee, R. A. Yetter and T. J. Foley, "Effects of fuel and oxidizer particle dimensions on the propagation of aluminum containing thermites," *Proceedings of the Combust. Inst.,* vol. 33, pp. 1989-1996, 2011.

[13] M. Pantoya and J. J. Granier, "Combustion Behavior of Highly Energetic Thermites: Nano versus Micron Composites," *Prop. Expl. Pyrotech.,* vol. 30, pp. 53-62, 2005.

[14] J. M. Bergthorson, Y. Yavor, J. Palecka, W. Georges, M. Soo, J. Vickery, S. Goroshin, D. L. Frost and A. J. Higgins, "Metal-water combustion for clean propulsion and power generation," *Appl. Energ.,* vol. 186, pp. 13-27, 2017.

[15] H. Z. Wang, D. Y. C. Leung, M. K. H. Leung, M. Ni and K. Y. Chan, "Modeling and analysis of an aluminum-water electrochemical generator for simultaneous production of electricity and hydrogen," *Int. J. Energ. Res.,* vol. 35, pp. 44-51, 2011.

[16] J. Petorvic and G. Thomas, "Reaction of aluminum with water to produce hydrogen," U.S. Department of Energy, 2008.

[17] Z. Y. Deng, J. M. F. Ferreira and Y. Sakka, "Hydrogen-generation materials for portable applications," *J. Am. Ceram. Soc.,* vol. 91, pp. 3825-3834, 2008.

[18] G. A. Risha, S. F. Son, R. A. Yetter, V. Yang and B. C. Tappan, "Combustion of nano-aluminum and liquid water," *Proceedings Comb. Inst.,* vol. 31, pp. 2029-2036, 2007.

[19] M. A. Trunov, M. Schoenitz, X. Zhu and E. L. Dreizin, "Effect of Polymorphic Phase Transformations in Al2O3 Film on Oxidation Kinetics of Aluminum Powders," *Combust. Flame,* vol. 140, pp. 310-318, 2005.

[20] M. V. Coulet, B. Rufino, P. H. Esposito, T. Neisius, O. Isnard and R. Denoyel, "Oxidation Mechanism of Aluminum Nanopowders," *J. Phys. Chem. C.,* vol. 119, pp. 25063-25070, 2015.

[21] M. W. Beckstead, "A Summary of Aluminum Combustion," RTO-EN-023, Rhode-Saint-Genese, 2004.

[22] Y. Yavor, S. Goroshin, J. M. Bergthorson, D. L. Frost, R. Stowe and S. Ringuette, "Enhanced hydrogen generation from aluminum-water reactions," *Int. J. Hydr. Energ.,* vol. 38, pp. 14992-15002, 2013.

[23] H. Nie, S. Zhang, M. Schoenitz and E. L. Dreizin, "Reaction interface between aluminum and water," *Int. J. Hydr. Energ.,* vol. 38, pp. 11222-11232, 2013.

[24] S. S. Razavi-Tousi and J. A. Szpunar, "Effect of structural evolution of aluminum powder during ball milling on hydrogen generation in aluminum-water reaction," *Int J Hydr Energ,* pp. 1-12, 2013.

[25] Q. S. Fu, Y. Q. Que, Z. X. Cui and M. F. Wang, "Study on the Size-Dependent Oxidation Reaction Kinetics of Nanosized Zinc Sulfide," *J. Nanomater.,* vol. 2014, p. 856489, 2014.

[26] M. A. Trunov, S. M. Umbrajkar, M. Schoenitz, J. T. Mang and E. L. Dreizin, "Oxidation and Melting of Aluminum Nanopowders," *J. Phys. Chem. B,* pp. 13094-13099, 2006.

[27] B. C. Yang, Y. J. Chai, F. L. Yang, Q. Zhang, H. Liu and N. Wang, "Hydrogen generation by aluminum-water reaction in acidic and alkaline media and its reaction dynamics," *Int. J. Energ. Res.,* vol. 42, pp. 1594-1602, 2018.

[28] K. T. Sullivan, N. W. Piekiel, C. Wu, S. Chowdhury, S. T. Kelly, T. C. Hufnagel, K. Fezzaa and M. R. Zachariah, "Reaction sintering: An important component in the combustion of nanocomposite thermites," *Comb. Flame,* vol. 159, pp. 2-15, 2012.

[29] V. Sanders, B. Asay, T. Foley, B. Tappan, A. Pacheco and S. Son, "Reaction Propagation of Four Nanoscale Energetic Composites (Al/MoO3, Al/WO3, Al/CuO, and Bi2O3)," *J. Propul. Power,* vol. 23, pp. 707-714, 2007.

[30] G. O. Piloyan, N. S. Bortnikov and N. M. Boeva, "The determination of surface thermodynamic properties of nanoparticles by thermal analysis," *J. Modern Phys.,* vol. 4, pp. 16-21, 2013.

[31] S. C. Stacy, X. Zhang, M. Pantoya and B. Weeks, "The Effects of Density on Thermal Conductivity and Absorption Coefficient for Consolidated Aluminium Nanoparticles," *Int. J. Heat Mass Transf.,* vol. 73, pp. 595-599, 2014.

[32] J. J. Granier and M. L. Pantoya, "Laser Ignition of Nanocomposite Thermites," *Comb. Flame,* vol. 138, pp. 373-383, 2004.

[33] M. L. Pantoya, V. I. Levitas, J. J. Granier and J. B. Henderson, "Effect of Bulk Density on Reaction Propagation In Nanothermites and Micron Thermites," *J. Prop. Power,* vol. 25, pp. 465-470, 2009.

[34] D. Stamatis and E. L. Dreizin, "Thermal initiation of consolidated nanocomposite thermites," *Combustion and Flame,* vol. 158, pp. 1631-1637, 2011.

[35] F. Saceleanu, J. Z. Wen, M. Idir and N. Chaumeix, "Laser Assisted Ignition and Combustion Characteristics of Consolidated Aluminum Nanoparticles," *J. Nanopart. Res.,* vol. 18, p. 328, 2016.

[36] M. Andisheh-Talbir, M. El Hannach, E. Kjeang and M. Bahrami, "An analytical relationship for calculating the effective diffusivity of micro-porous layers," *Int. J. Hydr. Energy,* vol. 40, pp. 10242-10250, 2015.

[37] L. S. Fan and C. Zhu, "Size and Properties of Particles," in *Principles of Gas-Solid Flows*, Cambridge University Press, 2005.

[38] F. Emmerling, *Precision Measurement of the Specific Surface Area of Solids by Gas Adsorption,* BAM Reference procedure, 2014.

[39] J. M. Zielinski and L. Kettle, *Physical Characterization: Surface Area and Porosity,* Intertek, 2013.

[40] B. Akbari, M. P. Tavandashti and M. Zandrahimi, "Particle Size Characterization of Nanoparticles - A Practical Approach," *Iran. J. Mat. Sci. Eng.,* vol. 8, pp. 48-56, 2011.

[41] F. Noor, H. Zhang, T. Korakianitis and D. Wen, "Oxidation and ignition of aluminum nanomaterials," *Phys. Chem. Chem. Phys.,* vol. 15, pp. 20176-20188, 2013.

[42] F. Ahmadi, "A New Approach to Undestanding the Mechanism and Effect of Phase Change of Aluminum in Aluminum Nanoparticles Oxidation: An Experimental Study," *Int. J. Sci. Eng. Res.,* vol. 5, pp. 48-56, 2014.

[43] C. Kong, D. Yu, S. Li and Q. Yao, "Mechanism and modelling of aluminum nanoparticle oxidation coupled with crystallisation of amorphous Al2O3 shell," *Combust. Theor. Model.,* vol. 20, pp. 296-312, 2016.

[44] T. Bazyn, H. Krier and N. Glumac, "Combustion of Nanoaluminum at Elevated Pressure and Temperature Behind Reflected Shock Waves," *Comb. Flame,* vol. 145, pp. 703-713, 2006.

[45] W. Zhou, J. B. DeLisio, X. Wang, G. C. Egan and M. R. Zachariah, "Evaluating free vs bound oxygen on ignition of nano-aluminum based energetics leads to a critical reaction rate criterion," *J. Appl. Phys.,* vol. 18, p. 114303, 2015.

[46] K. Park, D. Lee, A. Rai, D. Mukherjee and M. R. Zachariah, "Size-Resolved Kinetic Measurements of Aluminium Nanoparticle Oxidation with Single Particle Mass Spectrometry," *J. Phys. Chem. B.,* vol. 109, pp. 7290-7299, 2005.

[47] M. M. Sandstrom, D. Oschwald and S. F. Son, "Laser Ignition of Aluminum Nanoparticles in Air," in *31st International Pyrotechnics Seminar*, 2004.

[48] W. I. Lee, A. C. Loos and G. S. Springer, "Heat of Reaction, Degree of Cure, and Viscosity of Hercules 3501-6 Resin," *J. Compos. Mater.,* vol. 16, pp. 510-520, 1982.

[49] M. A. Trunov, M. Schoenitz, X. Zhu and E. L. Dreizin, "Effect of polymorphic phase transformations in alumina layer on ignition of aluminum particles," *Combust. Theor. Model.,* vol. 10, pp. 603-623, 2006.

[50] S. Hasani, M. Panjepour and M. Shamanian, "Oxidation and Kinetic Analysis of Pure Aluminum Powder under Nonisothermal Condition," *Open Access Sci. Rep.,* vol. 1, pp. 1-7, 2012.

[51] A. B. Vorozhtsov, M. Lerner, N. Rodkevich, H. Nie, A. Abraham, M. Schoenitz and E. L. Dreizin, "Oxidation of nano-sized aluminum powders," *Thermochimica Acta,* pp. 48-56, 2016.

[52] N. Eisenreich, H. Fietzek, M. D. Juez-Lorenzo, V. Kolarik, A. Koleczko and V. Weiser, "On the Mechanism of Low Temperature Oxidation of Aluminum Particles down to the Nano-Scale," *Prop.*

Expl. Pyrotech., vol. 29, pp. 137-145, 2004.

[53] A. Rai, K. Park, L. Zhou and M. R. Zachariah, "Understanding the Mechanism of Aluminum Nanoparticle Oxidation," *Comb. Theo. Mod.,* vol. 10, pp. 843-859, 2006.

[54] F. Saceleanu, S. Atashin and J. Z. Wen, "Roles of diffusion mechanisms during oxidation of aluminum micro/nanoparticles," in *P. Can. Sect. Comb. Ins.*, Waterloo, 2016.

[55] V. I. Levitas, M. L. Pantoya, G. Chauhan and I. Rivero, "Effect of the Alumina Shell on the Melting Temperature Depression for Aluminum Nanoparticles," *J. Phys. Chem. C.,* vol. 113, pp. 14088-14096, 2009.

[56] E. L. Dreizin and M. Schoenitz, "Correlating ignition mechanism of aluminum-based reactive materials with thermoanalytical measurements," *Prog. Energ. Comb. Sci.,* vol. 50, pp. 81-105, 2015.

[57] J. Z. Wen, N. Chaumeix, S. Ory and G. Matzen, "Thermal Stability and Controlled Oxidation of Aluminum Nanoparticles," in *P. Can. Sect. Comb.*, Waterloo, 2015.

[58] V. E. Zarko, "Effect of Heat Transfer Peculiarities on Ignition and Combustion Behavior of Al Nanoparticles," *Eurasian Chemico-Technological Journal,* vol. 18, pp. 171-179, 2016.

[59] D. Sundaram, P. Puri and V. Yang, "A general theory of ignition and combustion of nano- and micron-sized aluminum particles," *Combust. Flame,* vol. 169, pp. 94-109, 2016.

[60] S. Hong and A. C. T. van Duin, "Molecular Dynamics Simulations of the Oxidation of Aluminum Nanoparticles using the ReaxFF Reactive Force Field," *J. Phys. Chem. C.,* vol. 119, pp. 17876-17886, 2015.

[61] Y. Ohkura, P. M. Rao and X. Zheng, "Flash ignition of Al nanoparticles: mechanism and applications," *Comb Flame,* vol. 158, pp. 2544-2548, 2011.

[62] T. Bazyn, H. Krier and N. Glumac, "Evidence for the transition from the diffusion-limit in aluminum particle combustion," *Proceedings of the Combustion Institute,* vol. 31, pp. 2021-2028, 2007.

[63] Y. Huang, G. A. Risha, V. Yang and R. A. Yetter, "Combustion of bimodal nano/micron-sized aluminum particle dust in air," *Proceedings of the Combustion Institute,* vol. 31, pp. 2001-2009, 2007.

[64] C. Rossi, Al-based Energetic Nanomaterials, vol. 2, London: ISTE Ltd., 2015.

[65] E. Lafontaine and M. Comet, Nanothermites, London: ISTE Editions Ltd, 2016.

[66] V. I. Levitas, "Burn time of aluminum nanoparticles: Strong effect of the heating rate and melt-dispersion mechanism," *Combustion and Flame,* vol. 156, pp. 543-546, 2009.

[67] V. I. Levitas, "Mechanochemical mechanism for reaction of aluminum nano- and micrometre-scale particles," *Philosophical Transactions of the Royal Society,* 2013.

[68] M. Bidabadi and J. Fereidooni, "Modelling Ignition Temperature and Burning Time of a Single Aluminium Nanoparticle," *Micro Nano Lett.,* vol. 8, pp. 783-787, 2013.

[69] R. Williams, *Ignition Mechanism in Nanocomposite Thermites (Doctoral Dissertation),* New Jersey Institute of Technology, 2014.

[70] S. Chowdhury, K. Sullivan, N. Piekiel, L. Zhou and M. R. Zachariah, "Diffusive vs Explosive Reaction at the Nanoscale," *J. Phys. Chem. C.,* vol. 114, pp. 9191-9195, 2010.

[71] K. Sullivan and M. R. Zachariah, "Simultaneous Pressure and Optical Measurements of Nanoaluminum Thermites: Investigating the Reaction Mechanism," *J. Propul. Power,* vol. 26, pp. 467-472, 2010.

[72] R. A. Williams, J. V. Patel, A. Ermoline, M. Schoenitz and E. L. Dreizin, "Correlation of optical emission and pressure generated upon ignition of fully-dense nanocomposite thermite powders," *Combust. Flame,* vol. 160, pp. 734-741, 2013.

[73] M. R. Weismiller, J. Y. Malchi, R. A. Yetter and T. J. Foley, "Dependence of flame propagation on pressure and pressurizing gas for an Al/CuO nanoscale thermite," *Proceedings of the Combustion Institute,* vol. 32, pp. 1895-1903, 2009.

[74] V. Y. Egorshev, V. P. Sinditskii and K. K. Yartsev, "Combustion of high-density CuO/Al nanothermites at elevated pressures," in *Proceedings of 2013 International Autumn Seminar on Propellants, Explosive and Pyrotechnics*, Chengdu, 2013.

[75] R. J. Jacob, G. Jian, P. M. Guerieri and M. R. Zachariah, "Energy release pathways in nanothermites follow through the condensed state," *Combustion and Flame,* vol. 162, pp. 258-264, 2015.

[76] E. M. Hunt and M. L. Pantoya, "Ignition Dynamics and Activation Energies of Metallic Thermites: From Nano- to Micron-scale Particulate Composites," *J. Appl. Phys.,* vol. 98, p. 034909, 2005.

[77] K. Kim, "Computational Modeling of Combustion Wave in Nanoscale Thermite Reaction," *Int. J. Chem. Molecular Nuc. Mat. Mettal. Eng.,* vol. 8, pp. 679-682, 2014.

[78] B. W. Asay, S. F. Son, J. R. Busse and D. M. Oschwald, "Ignition Characteristics of Metastable Intermolecular Composites," *Propellants Explos. Pyrotech.,* vol. 29, pp. 216-219, 2004.

[79] D. Prentice, M. L. Pantoya and A. E. Gash, "Combustion Wave Speeds of Sol-Gel-Synthesized Tungsten Trioxide and Nano-Aluminum: The Effect of Impurities on Flame Propagation," *Energ. Fuels,* vol. 20, pp. 2370-2376, 2006.

[80] G. M. Dutro, R. A. Yetter, G. A. Risha and S. F. Son, "The effect of stoichiometry on the combustion behavior of a nanoscale Al/MoO3 thermite," *Proceedings of the Combust. Inst.,* vol. 32, pp. 1921-1928, 2009.

[81] K. T. Sullivan, W. A. Chiou, R. Fiore and M. R. Zachariah, "In situ microscopy of rapidly heated nano-Al and nano- Al/WO 3 thermites," *Appl. Phys. Lett.,* vol. 97, p. 133104, 2010.

[82] G. Jian, L. Zhou, N. W. Piekiel and M. R. Zachariah, "Low Effective Activation Energies for Oxygen Release from Metal Oxides: Evidence for Mass-Transfer Limits at High Heating Rates," *Chem. Phys. Chem.,* vol. 15, pp. 1666-1672, 2014.

[83] X. Zhou, Y. Wang, Z. Cheng, X. Ke and W. Jiang, "Facile preparation and energetic characteristics of core-shell Al/CuO metastable intermolecular composite thin films on a silicon substrate," *Chem. Eng. J.,* pp. 585-590, 2017.

[84] C. Yu, W. Zhang, B. Hu, D. Ni, Z. Zheng, J. Liu, K. Ma and W. Ren, "Core/shell CuO/Al nanorod thermite film based on electrochemical anodization," *Nanotech.,* vol. 29, 2018.

[85] S. M. Umbrajkar, M. Schoenitz and E. L. Dreizin, "Exothermic reactions in Al-CuO nanocomposites," *Thermochim. Acta,* vol. 451, pp. 34-43, 2006.

[86] Z.-Y. Deng, L.-L. Zhu and Y.-B. Tang, "Role of Particle Sizes in Hydrogen Generation by the Reaction of Al with Water," *J. Am. Ceram. Soc.,* vol. 93, pp. 2998-3001, 2010.

[87] W. Z. Gai, W. H. Liu, Z. Y. Deng and J. G. Zhou, "Reaction of Al powder with water for hydrogen generation under ambient condition," *Int. J. Hydr. Energ.,* vol. 37, pp. 13132-13140, 2012.

[88] S. F. Tikhov, V. A. Sadykov, A. I. Ratko, T. F. Kouznetsova, V. E. Romanenkov and S. I. Eremenko, "Kinetics of aluminum powder oxidation by water at 100 C," *React. Kinet. Catal. Lett.,* vol. 92, pp. 83-88, 2007.

[89] H. Nie, M. Schoenitz and E. L. Dreizin, "Calorimetric investigation of the aluminum-water reaction," *Int. J. Hydr. Energ.,* vol. 37, pp. 11035-11045, 2012.

[90] A. Lozhkomoev, E. Glazkova, S. Kazantsev, I. Gorbikov, O. Bakina, N. Svarovskaya, A. Miller, M. Lerner and S. Psakhie, "Formation of micro/nanostructured AlOOH hollow spheres from aluminum nanoparticles," *Nanotech. Russia,* vol. 10, pp. 858-864, 2015.

[91] H.-W. Wang, H.-W. Chung, H.-T. Teng and G. Cao, "Generation of hydrogen from aluminum and

water - effect of metal oxide nanocrystals and water quality," *Int. J. Hydr. Energ.,* vol. 36, pp. 15136-15144, 2011.

[92] A. P. Astankova, A. Y. Godymchuk, A. A. Gromov and I. AP, "The Kinetics of Self-Heating in the Reaction between Aluminum Nanopowder and Liquid Water," *Rus J Phys Chem A,* vol. 82, pp. 1913-1920, 2008.

[93] S. S. Razavi-Tousi and J. A. Szpunar, "Role of ball milling of aluminum powders in promotion of aluminum-water reaction to generate hydrogen," *Metalllurg. Mat. Transact.,* vol. 1E, pp. 247-256, 2014.

[94] A. V. Ilyukhina, O. V. Kravchenko, B. M. Bulychev and E. I. Shkolnikov, "Mechanochemical activation of aluminum with gallams for hydrogen evolution from water," *Int. J. Hydr. Energ.,* vol. 35, pp. 1905-1910, 2010.

[95] K. Mahmoodi and B. Alinejad, "Enhancement of hydrogen generation rate in reaction of aluminum with water," *Int. J. Hydr. Energ.,* vol. 35, pp. 5227-5232, 2010.

[96] Q. Lei, B. Wang, P. Wang and S. Liu, "Hydrogen generation with acid/alkaline amphoteric water electrolysis," *J. Energy. Chem.,* vol. 38, pp. 162-169, 2019.

[97] C. B. Porciuncula, N. R. Marcilio, I. C. Tessaro and M. Gerchmann, "Production of Hydrogen in the Reaction between Aluminum and Water in the Presence of NaOH and KOH," *Braz. J. Chem. Eng.,* vol. 29, pp. 337-348, 2012.

[98] M.-Q. Fan, F. Xu, L.-X. Sun, J.-N. Zhao, T. Jiang and W.-X. Li, "Hydrolysis of ball milling Al-Bi-hydride and Al-Bi-salt mixture for hydrogen generation," *J. Alloys Comp.,* vol. 460, pp. 125-129, 2008.

[99] Y. Sun, R. Sun, B. Zhu and Y. Wu, "Effects of additives on the hydrogen generation of Al-H2O reaction at low temperature," *Int. J. Energy Res.,* vol. 41, pp. 2020-2033, 2017.

[100] Y. K. Chen, H. T. Teng and T. Y. Lee, "Rapid hydrogen generation from aluminum-water system by adjusting water ratio to various aluminum/aluminum hydroxide," *Int. J. Energ. Environ. Eng.,* vol. 87, pp. 1-6, 2014.

[101] W. Z. Gai, C. S. Fang and Z. Y. Deng, "Hydrogen generation by the reaction of Al with water using oxides as catalysts," *Int. J. Energy Res.,* vol. 38, pp. 918-925, 2014.

[102] L. Zhang, Y. Tang, Y. Duan, L. Hou, L. Cui, F. Yang, Y. Zheng, Y. Li and J. Huang, "Green production of hydrogen by hydrolysis of graphene-modified aluminum through infrared light irradiation," *Chem. Eng. J.,* vol. 320, pp. 160-167, 2017.

[103] Y. C. Wen, W. M. Huang and H. W. Wang, "Kinetics study on the generation of hydrogen from an

aluminum/water system using synthesized aluminum hydroxides," *Int. J. Energy Res.,* vol. 42, pp. 1615-1624, 2017.

[104] H. Liu, F. Yang, B. Yang, Q. Zhang, Y. Chai and N. Wang, "Rapid hydrogen generation through aluminum-water reaction in alkali solution," *Cat. Today,* vol. 318, pp. 52-58, 2018.

[105] B. C. Bunker, G. C. Nelson, K. R. Zavadil, J. C. Barbour, F. D. Wall, J. P. Sullivan, C. F. Windisch, M. H. Engelhardt and D. R. Baer, "Hydration of passive oxide films on aluminum," *J. Phys. Chem. B,* vol. 106, pp. 4705-4713, 2002.

[106] M. Curioni and F. Scenini, "The mechanism of hydrogen evolution during anodic polarization of aluminum," *Electrochim. Acta,* vol. 180, pp. 712-721, 2015.

[107] Z.-Y. Deng, J. M. F. Ferreira, Y. Tanaka and J. Ye, "Physicochemical mechanism for the continuous reaction of gamma-Al2O3-modified aluminum powder with water," *J. Am. Ceram. Soc.,* vol. 90, pp. 1521-1526, 2007.

[108] W. Vedder and D. A. Vermilyea, "Aluminum + Water Reaction," *Trans. Faraday Soc.,* vol. 65, pp. 561-584, 1969.

[109] Y. Lin, A. A. Nepapushev, P. J. McGinn, A. S. Rogachev and A. S. Mukasyan, "Combustion joining of carbon/carbon composites by a reactive mixture of titanium and mechanically activated nickel/aluminum powders," *Ceram. Int.,* vol. 39, pp. 7499-7505, 2013.

[110] K. T. Higa, "Energetic Nanocomposite lead-free electric primers," *J. Propul. Power,* vol. 23, pp. 722-727, 2007.

[111] T. Troianello, "Precision foil resistors used as electro-pyrotechnic initiator," in *Electronic Components and Technology Conference*, 2001.

[112] H. H. DiBiaso, B. A. English and M. G. Allen, "Solid-phase conductive fuels for chemical microactuators," *Sensors and Actuators A: Physical,* vol. 111, pp. 260-266, 2004.

[113] S. J. Apperson, "Characterization and MEMS Applications of Nanothermite Materials (Doctoral Dissertation)," Faculty of the Graduate School, University of Missouri, 2010.

[114] D. H. L. Jr, S. W. Janson, R. B. Cohen and E. K. Antonsson, "Digital MicroPropulsipon," *Sensors and Actuators A: Physical,* vol. 80, pp. 143-154, 2000.

[115] C. Rossi, D. Briand, M. Dumonteuil, T. Camps, P. Q. Pham and N. F. Rooij, "Matrix of 10x10 addressed solid propellant microthrusters: review of the technologies," *Sensors and Actuators A: Physical,* vol. 126, pp. 241-252, 2006.

[116] C. Acar and I. Dincer, "Review and evaluation of hydrogen production options for better environment," *J. Cleaner Prod.,* vol. 218, pp. 835-849, 2019.

[117] K. Wando, V. Shmelev, S. Finiakov, Y. Cho and W. Yoon, "Combustion of micro aluminum-water mixtures," *Combust. Flame,* vol. 160, pp. 2990-2995, 2013.

[118] V. M. Shmelev and S. V. Finyakov, "Specifics of the combustion of aluminum-water mixtures," *Russian J. Phys. Chem. B,* vol. 7, pp. 437-447, 2013.

[119] T. F. Miller and J. D. Herr, "Green rocket propulsion by reaction of Al and Mg powders and water," in *40th AIAA/ASME/SAW/ASEE Joint Propulsion Conference and Exhibit*, Fort Lauderdale, 2004.

[120] G. N. Eby, in *Principles of environmental geochemistry*, Pacific Grove, Thomson-Brooks/Cole, 2004, pp. 212-214.

[121] A. Khawam and D. R. Flanagan, "Solid-state kinetic models: basics and mathematical fundamentals," *J. Phys. Chem. B,* vol. 110, pp. 17315-17328, 2006.

[122] H. E. Kissinger, "Variation of peak temperature with heating rate in differential thermal analysis," *J. Res. Nat. Bur. Stand.,* vol. 57, pp. 217-221, 1956.

[123] F. J. Gotor, J. M. Criado, J. Malek and N. Koga, "Kinetic analysis of solid-state reactions: the universality of master plots for analyzing isothermal and nonisothermal experiments," *J. Phys. Chem. A.,* vol. 104, pp. 10777-10782, 2000.

[124] P. Simon, "Isoconversional Methods: Fundamentals, meaning and application," *J. Therm. Anal. Calorim.,* vol. 76, pp. 123-132, 2004.

[125] A. W. Coats and J. P. Redfern, "Kinetic Parameters from Thermogravimetric Data," *Nature,* vol. 201, pp. 68-69, 1964.

[126] C. D. Doyle, "Integral methods of kinetic analysis of thermogravimetric data," *Macromolec. Chem. Phys.,* pp. 220-224, 1964.

[127] S. V. Vyazovkin and A. I. Lesnikovich, "Practical application of isoconversional methods," *Thermochim. Acta,* vol. 203, pp. 177-185, 1992.

[128] S. Vyazovkin and C. A. Wight, "Isothermal and non-isothermal kinetics of thermally stimulated reactions of solids," *Int. Rev. Phys.Chem.,* vol. 17, pp. 407-433, 1998.

[129] E. F. Caldin, The Mechanisms of Fast Reactions in Solution, Amsterdam: IOS Press, 2001.

[130] R. E. Carter, "Kinetic Model for Solid-State Reactions," *J. Chem. Phys.,* pp. 2010-2015, 1961.

[131] L. A. Perez-Maqueda, J. M. Criado and J. Malek, "Combined kinetic analysis for crystallization kinetics of non-crystalline solids," *J. Non-Crystal Solids,* vol. 320, pp. 84-91, 2003.

[132] S. A. T. Redfern, "The Kinetics of Dehydroxylation of Kaolinite," *Clay Miner.,* vol. 22, pp. 447-456, 1987.

[133] L. S. Kagan, S. B. Margolis and G. I. Sivashinsky, "Modelling the transition from conductive to convective burning in porous energetic materials," *Combust. Theory Model. ,* vol. 16, pp. 737-746, 2012.

[134] M. Wang and N. Pan, "Predictions of effective physical properties of complex multiphase materials," *Mat. Science Eng. R,* vol. 63, pp. 1-30, 2008.

[135] N. I. o. S. a. Technology, "NIST Chemistry WebBook SRD 69," U.S. Department of Commerce, 2018. [Online]. Available: https://webbook.nist.gov/chemistry/. [Accessed February 2019].

[136] S. C. Stacy, R. A. Massad and M. L. Pantoya, "Pre-ignition laser ablation of nanocomposite energetic materials," *Journal of Applied Physics,* vol. 113, p. 213107, 2013.

[137] L. Macku, "Arrhenius equation parameters identification from temperature profiles," in *Annals for DAAAM for 2011 & Proceedings of the 22nd International DAAM Symposium*, Vienna, 2011.

[138] M. Mazzotti, "Introduction to chemical engineering: chemical reaction engineering," ETH Swiss Federal Institute of Technology Zurich Separation Processes Laboratory, Zurich, 2015.

[139] F. Saceleanu, S. Atashin and J. Z. Wen, "Role of phase transformations in micro and nano aluminum powders on kinetics of oxidation using thermogravimetric analysis," *Phys. Chem. Chem. Phys. C,* vol. 19, pp. 18996-19009, 2017.

[140] P. S. Santos, H. S. Santos and S. P. Toledo, "Standard Transition Aluminas, Electron Microscopy Studies," *Mat. Res.,* vol. 3, pp. 104-114, 2000.

[141] Y. Rozita, R. Brydson and A. J. Scott, "An investigation of commercial gamma-Al2O3 nanoparticles," *J. Phys. Conf. Series,* 2010.

[142] J. S. Raut, R. B. Bhagat and K. A. Fichthorn, "Sintering of Aluminum Nanoparticles: A Molecular Dynamics Study," *NanoStruct. Mater.,* vol. 10, pp. 837-851, 1998.

[143] X. Luo, U. Sundararaj and J. L. Luo, "Oxidation kinetics of copper nanowires synthesized by AC electrodeposition of copper into porous aluminum oxide templates," *J. Mater. Res.,* vol. 27, pp. 1755-1762, 2012.

[144] S. Hasani, M. Panjepour and M. Shamanian, "Non-Isothermal Kinetic Analysis of Oxidation of Pure

Aluminum Powder Particles," *Oxid. Met.,* vol. 81, pp. 299-313, 2014.

[145] W. He, W. Lv and J. H. Dickerson, Gas Transport in Solid Oxide Fuel Cells, New York: Springer Science, 2014.

[146] F. Saceleanu, M. Idir, N. Chaumeix and J. Z. Wen, "Combustion characteristics of physically mixed 40 nm aluminum/copper oxide nanothermites using laser ignition," *Font. Chem.,* vol. 6, p. 465, 2018.

[147] Kaye&Laby, "Tables of Physical & Chemical Constants, Thermal conducvities," National Physical Laboratory, 2018. [Online]. Available: http://www.kayelaby.npl.co.uk/general_physics/2_3/2_3_7.html. [Accessed July 2018].

[148] S. Apperson, R. V. Shende, S. Subramanian, D. Tappmeyer, S. Gangopadhyay, Z. Chen, K. Gangopadhyay, P. Redner, S. Nicholich and D. Kapoor, "Generation of fast propagating combustion and shock waves with copper oxide/ aluminum nanothermite composites," *Appl. Phys. Lett.,* vol. 91, 2007.

[149] V. V. Skorokhod, O. I. Get'man, A. E. Zuev and S. P. Rakitin, "Correlation between the particle size, pore size, and porous structure of sintered tungsten," *Soviet Powder Metallurgy and Metal Ceramics,* vol. 27, pp. 941-947, 1988.

[150] NIST, "NIST Chemistry WebBook, SRD 69," U.S. Department of Commerce, 2017. [Online]. Available: https://webbook.nist.gov/chemistry/. [Accessed July 2018].

[151] A. B. Murphy and C. J. Arundell, "Transport Coefficients of Argon, Nitrogen, Oxygen Argon-Nitrogen, and Argon-Oxygen Plasmas," *Plasma Chemistry and Plasma Processing,* vol. 14, pp. 451-490, 1994.

[152] V. Baijot, L. Glavier, J. M. Ducere, M. D. Rouhani, C. Rossi and A. Esteve, "Modeling the pressure generation in aluminum based thermites," *Propellants Explos. Pyrotech.,* vol. 40, pp. 402-412, 2015.

[153] R. J. Jacob, D. L. Ortiz-Montalvo, K. R. Overdeep, T. P. Weihs and M. R. Zachariah, "Incomplete reactions in nanothermite composites," *J. Appl. Phys.,* vol. 121, 2017.

[154] S. F. Son, B. W. Asay and T. J. Foley, "Combustion of Nanoscale Al/MoO3 Thermite in Microchannels," *J. Prop. Pow.,* vol. 23, pp. 715-721, 2007.

[155] G. C. Egan, T. LaGrange and M. R. Zachariah, "Time-Resolved Nanosecond Imaging of Nanoscale Condensed Phase Reaction," *J. Phys. Chem. C,* vol. 119, pp. 2792-2797, 2014.

[156] L. Glavier, G. Taton, J.-M. Ducere, V. Baijot, S. Pinon, T. Calais, A. Esteve, M. D. Rouhani and C.

Rossi, "Nanoenergetics as pressure generator for nontoxic impact primers: Comparison of Al/Bi2O3, Al/CuO, Al/MoO3 nanothermites and Al/PTFE," *Comb. Flame,* vol. 162, pp. 1813-1820, 2015.

[157] F. Saceleanu, L. LeSergent, H. Sui, J. Z. Wen, C. F. Petre, D. Chamberland, P. Beland and T. Ringuette, "Low-power laser ignition of Al/CuO nano powders and Al/Cu2O nanolaminates," in *Proceedings of Combustion Institute - Canadian Section*, Toronto, 2018.

[158] G. Lahnier, A. Nicollet, J. Zapata, L. Marin, N. Richard, M. Rouhani, C. Rossi and A. Esteve, "A diffusion-reaction scheme for modeling ignition and self-propagation reactions in Al/CuO multilayered thin films," *J Appl Phys,* vol. 122, p. 155105, 2017.

[159] L. LeSergent, Tailoring the Ignition and Reaction Properties of Cu2O Thermite Nanolaminates, Waterloo: University of Waterloo, 2018.

[160] M. Salloum and O. M. Knio, "Simulation of reactive nanolaminates using reduced models: I. basic formulation," *Combust. Flame,* vol. 157, pp. 288-295, 2010.

[161] A. F. Fedorov and A. V. Shul'gin, "Point Model of Combustion of Aluminum Nanoparticles in the Reflected Shock Wave," *Combust. Explos. Shock Waves,* vol. 47, pp. 289-293, 2011.

[162] G. C. Egan and M. R. Zachariah, "Commentary on the heat transfer mechanisms controlling propagation in nanothermites," *Combustion and Flame,* vol. 162, pp. 2959-2961, 2015.

[163] G. C. Egan, "Understanding the Reaction Mechanism of Aluminum Nanocomposite Thermites," Faculty of the Graduate School of the University of Maryland, PhD dissertation , 2015.

[164] A. Nicollet, G. Lahiner, A. Belisario, S. Assie-Souleille, M. Djafari-Rouhani, A. Esteve and C. Rossi, "Investiation of Al/CuO multilayered thermite ignition," *J Appl Phys,* vol. 121, pp. 34503-34503, 2017.

[165] F. Saceleanu, T. V. Vuong, E. R. Master and J. Z. Wen, "Tunable kinetics of nanoaluminum and microaluminum powders reacting with water to produce hydrogen," *Int. J. Energy Res.,* pp. 1-13, 2019.

[166] A. S. E112-13, "Standard Test Methods for Determining Average Grain Size," ASTM International, West Conshohocken, PA, 2014.

[167] E. Moukhina, "Determination of kinetic mechanisms for reactions measured with thermoanalytical instruments," *J. Therm. Anal. Calorim.,* vol. 109, pp. 1203-1214, 2012.

[168] S. Vyazovkin, "Conversion dependence of activation energy for model DSC curves of consecutive reactions," *Thermochim. Acta,* vol. 236, pp. 1-13, 1994.

[169] S. Vyazovkin, "An approach to the solution of the inverse kinetic problem in the case of complex processes: part 4. chemical reaction complicated by diffusion," *Thermochim. Acta,* vol. 223, pp. 201-206, 1993.

[170] M. Miadokova and M. Molnarova-Plchova, "Kinetics and mechanism of the reaction of aluminum in aqueous solution of sodium hydroxide," *Chem. Papers,* vol. 2, pp. 229-235, 1985.

[171] S. J. Apperson, A. V. Bezmelnitsyn, R. Thiruvengadathan, K. Gangopadhyay and S. Gangopadhyay, "Characterization of nanothermite material for solid-fuel microthruster applications," *J. Prop. Power,* vol. 25, pp. 1086-1091, 2009.

[172] C. S. Slaley, K. E. Raymond, R. Thiruvengadathan, S. J. Apperson, K. Gangopadhyay, S. M. Swaszek, R. J. Taylor and S. Gangopadhyay, "Fast-impulse nanothermite solid-propellant miniaturized thrusters," *J. Prop. Power,* vol. 29, pp. 1400-1409, 2013.

[173] B. Li, A. D. Sediako, P. Zhao, J. Li, E. Croiset, M. J. Thomson and J. Z. Wen, "Real-Time Observation of Carbon Oxidation by Driven Motion of Catalytic Ceria Nanoparticles within Low Pressure Oxygen," *Sci. Rep.,* vol. 9, p. 8082, 2019.